Negative Ions in Outer Solar System Plasmas: Titan, Europa & Rhea

Ravindra Tobias Desai

A dissertation submitted in partial fulfillment

of the requirements for the degree of

Doctor of Philosophy

of

University College London.

Mullard Space Science Laboratory

University College London

June 8, 2018

I, Ravindra Tobias Desai, confirm that the work presented in this thesis is my own. Where information has been derived from other sources, I confirm that this has been indicated in the work.

Abstract

Negative ions exist in many astrophysical environments. They are the major source of opacity in stars such as our sun and played a role in forming the first stars in the early-universe. In recent years, significant populations of negatively charged ions have been discovered in plasma environments within the outer solar system, discoveries which in many cases were serendipitously made by instruments not designed for this purpose. This thesis uses a combination of spacecraft data analysis and numerical simulations to study negatively charged ions observed by Cassini at the Saturnian moons, Titan and Rhea, and by Galileo at the Jovian moon Europa.

The first study focuses on detections by Cassini's Electron Spectrometer of negatively charged ions and aerosols in Titan's ionosphere. An advanced model of the instrument response function is developed and used to statistically identify the presence of carbon chain anions, the first such detections within a planetary atmosphere. Observations of slightly larger anions are interpreted as a hitherto unknown chemical regime involving chemical structures incompatible with previously observed, or even known, anion species. Moreover, a multi-flyby analysis shows the smaller species to deplete with decreasing altitude at a rate proportional to the growth of the larger aerosols, a correlation which suggest these anions are coupled to this growth process. These results demonstrate the importance of tracing a route from small to large species to understand how complex organics can be produced within a planetary atmosphere.

The second study derives from Galileo magnetometer observations near Europa which, surprisingly, showed both left-hand and right-hand wave power at the Chlorine ion gyrofrequency. These waves are generated by the outflow of newly ionised material and, in this case, the mix of polarisations was inferred to result from the presence of both positive and negative Chlorine ions. To test this hypothesis, a hybrid particle-in-cell simulation technique is used to carry out the first study focussing on negative ions generating the Alfvén-cyclotron instability in order to constrain the non-linear relation between sources densities, wave amplitudes and polarisation, for

Chlorine pickup ions in conditions representative of the Europa plasma environment. Through relating simulated and observed wave properties, Chlorine pickup ion densities are constrained to within 0.1-1.5 cm^{-3} in localised regions in Europa's plasma wake, with not less than 5% resulting from a negatively charged component. These results suggest the moon is a net source of these species with implications for the salinity of the global sub-surface ocean.

The third study focuses on both positive and negative pickup ions detected by Cassini's Plasma Spectrometer at Rhea. Using velocity space analysis and expressions derived for partially filled velocity-ring distributions, the positive pickup ions observed during two Rhea flybys are identified as compatible with CO_2^+. The negative pickup ions, observed during the first targeted Rhea flyby, are identified as incompatible with the previous identification of O^- and instead are shown as compatible with heavier species in the range of 26 ± 3 u. These are consequently attributed to carbon-based compounds, such as CN^-, C_2H^-, C_2^-, or HCO^-, and are suggested to derive from carbonaceous material on the moon's, likely negatively charged, surface. Unidentified, dark, possibly carbon-bearing material, is apparent in near-infrared observations of the surfaces of Rhea, Dione, Pheobe, Iapetus, Hyperion, Epimetheus and throughout Saturn's F-ring. These identifications thus provide context for understanding what minority species could be present within the surfaces of the icy moons of the giant planets.

Acknowledgements

The research carried out over the last three years was carried out with the assistance of a great many people whom I would all like to thank wholeheartedly.

I first of all thank Andrew Coates for his advice and guidance and more than extensive knowledge of plasma and planetary physics which allowed me to pursue multiple different research avenues. I thank Dhiren Kataria for his expertise in instrument science which allowed me the in-depth understanding of plasma spectrometers upon which many results are based upon, as well as his continued support. I thank Misa Cowee, who acted as an unofficial third advisor starting during my stay at the Los Alamos National Laboratory, by instructing me in the arts of computational plasma physics simulations. I would also like to thank Martin Cordiner for his assistance in analysing ALMA datasets during my visit to NASA Goddard Space Flight Centre

I thank Gethyn Lewis for his assistance in understanding Cassini data, Peter Gary for his contribution regarding fundamental plasma wave theory, Denis Caniulef for his input regarding statistic methods, and Daisuke Kawata for his sage advice. I thank Sam Taylor, Leonardo Regoli, William Dunn, Kim Birkett, Jamie Jasinski, Lin Gilbert, Oliver Price, Roger Stabbins, Eleni Bohacek, Geraint Jones, Annie Wellbrock and Raquel Caro-Carretero, for their feedback and advice during office and group discussions and Graziella Branduardi-Raymont and the wider space plasma physics group for their thorough questioning and feedback at group meetings and seminars. My thanks also go out to the Cassini Plasma Spectrometer team as well as many further collaborators.

On a personal level I would like to thank my fiancée Stephanie for her everlasting support, my friends who helped in keeping me sane during this period of my life, and, last but not least, my parents and all family members who helped in bringing me to this stage.

Contents

List of Figures

List of Tables

Chapter 1

Introduction

Plasma is considered the fourth state of matter beyond solid, liquid and gas, and accounts for more than 99% of the observable universe. Plasma is present from around 60 km upwards within the Earth's atmosphere, within the Sun and interplanetary space, and throughout the cosmos, indeed leaving us living within a small and unique corner. The study of astrophysical environments is therefore greatly facilitated by the understanding of plasmas, which constitute such a significant part.

Numerous sources of plasma exist within the Universe. The Sun, itself a giant ball of plasma, provides a significant source within our Solar System. At its surface the thermal pressure exceeds the gravitational pressure and results in the expulsion of supersonic plasma known as the solar wind. This flows through interplanetary space and dominates a giant region termed the heliosphere. At the edge of the heliosphere a pressure balance is achieved with the interplanetary plasma, the properties of which are presumably dominated by the galactic environment and nearby active astrophysical objects.

Solar wind plasma impacts planetary bodies with various consequences. It can act to strip material away from non-magnetised bodies, as visualised by the extensive comas surrounding comets. This interaction is also thought to be the mechanism that stripped away Mars' once dense atmosphere, and the hydrogen from Venus' atmosphere, leaving it arid. Planetary bodies with internally generated magnetic fields can be protected from the direct onslaught of the solar wind by the generation of a magnetosphere, which diverts the incoming plasma around the body. The solar wind, however, still significantly influences magnetosphere dynamics by pressing upon the outside surfaces and entering via processes such as magnetic reconnection. This allows the solar wind plasma to flow inward along planetary magnetic field lines and drive visible phenomenon

such as aurora, known at the Earth as the Aurora Borealis and Aurora Australis.

The ionisation of neutral material at planetary bodies can also be a significant source of plasma. The ionisation of the Earth's atmosphere results in a sphere of plasma surrounding the planet and solar wind plasma can become trapped in the 'Van Allen' radiation belts, which can pose dangers to operational spacecraft and astronauts. Neutral material erupting from the volcanic plumes on Jupiter's moon Io and Saturn's moon Enceladus, also result in abundances of plasma that dominate the dynamics of these giant magnetospheres and drive aurora.

The majority of plasmas consist of positively charged ions and electrons, formed from the separation of these basic constituents of a neutral atom. It is, however, possible for a molecule to possess an excess electron, which results in a negatively charged ion. This is often termed a negative ion or, in more chemistry-focussed applications, an anion. These particles have been found to play a significant role in a number of space environments. They were instrumental in the formation of molecular hydrogen in the early Universe. This facilitated gravitational collapse and the formation of the first stars. They are a significant contributor to the opaqueness within the Sun's outer layers and causes the Sun to appear as a uniform yellowish colour. They also exist in abundance in the Earth's ionosphere, the closest space plasma to ourselves. In recent years a variety of space missions, namely Giotto, Galileo, Cassini, and Rosetta, have surprisingly found evidence of negative ions existing in abundance within Planetary and Cometary plasmas.

This thesis investigates the role of negatively charged ions within outer solar system plasmas, a topic represents a new frontier in their understanding. To this end, three broad aims are outlined below.

- **Aim I** The negatively charged ions in Titan's ionosphere, detected by the Cassini spacecraft, completely reshaped our understanding of the moon's thick upper atmosphere [*Coates et al.*, 2007a]. These detections were, however, made with an electron spectrometer and, as such, significant uncertainties exist with regards to their composition and abundance. The first research aim is to provide an improved understanding of these surprising observations by performing an in-depth analysis of the instrument response function to negative ions. This will then be used to further examine this remarkable dataset.

- **Aim II** Negatively charged ions were inferred to be outflowing from the Galilean moon Europa by the Galileo spacecraft, which observed the possible magnetic signatures of a

negative ion plasma instability [*Volwerk et al.*, 2001]. The second research aim is to perform the first numerical simulation study of the instability characteristics associated with negatively charged pickup ions, so as to assess whether this initial hypothesis could be correct. A combination of linear dispersion theory and hybrid simulations will be used to this end and the results used to further interpret this dataset.

- **Aim III** Negatively charged pickup ions were observed at the moon Rhea and provided evidence for this moon's tenuous exosphere [*Teolis et al.*, 2010]. The final research aim is to further constrain these detections using the methods already developed within the previous research efforts, that is an advanced understanding of how an electron instrument detects negatively charged ions and an increased understanding of the behaviour of negatively charged pickup ion populations.

Within this thesis the fundamental electrodynamic and plasma physics are first addressed, which underpin the physical concepts discussed. This is followed by a review of the various detections of negative ions in astrophysical plasmas and provides the bridge between the fundamental physics and the research carried out. This is then followed by a description of the research methods and techniques employed. The three aforementioned aims then culminate in three distinct research chapters, which describe the salient results obtained. The conclusions drawn from these endeavours are presented within a further chapter, which describes the overarching implications and further suggested research avenues.

1.1 Plasma Physics

The fundamental physics concepts described hereafter form the foundation of the field of plasma physics and are described in many textbooks such as those written by *Chen* [1974], *Baumjohann and Treumann* [1996], and *Bittencourt* [2004].

1.1.1 Single particle motion

A charged particle will experience forces and motion according to the Lorentz force law,

$$\frac{d\mathbf{p}}{dt} = q(\mathbf{E} + \mathbf{v} \times \mathbf{B}), \tag{1.1}$$

where $\mathbf{p}$ is the momentum, q is the charge, $\mathbf{E}$ is the electric field, $\mathbf{v}$ is the velocity, $\mathbf{B}$ is the magnetic field, and t is time. This force results in a charged particle gyrating around the magnetic field with the direction of rotation dependent on the charge state of the particle. The motion of such a charged particle results in a diamagnetic current that produces its own magnetic field acting in opposition to the background field.

In the presence of magnetic and electric fields a charged particle will be accelerated by the electric field and gyrate around the magnetic field. This overall direction of this motion is necessarily the centre around which the particle gyrates and is independent of the particles charge state as follows,

$$\mathbf{v_E} = \frac{\mathbf{E} \times \mathbf{B}}{B^2}. \tag{1.2}$$

This is called the $E \times B$ drift. This expression can also be derived via a Lorentz transformation of the electric field into the frame of the particle.

In the presence of a time-varying electric field, a polarisation drift occurs in the direction parallel and anti-parallel to the electric field. This is dependent on the mass and charge of the particle and is described as,

$$\mathbf{v_P} = \frac{1}{\omega_g B} \frac{d\mathbf{E}_\perp}{dt}, \tag{1.3}$$

where the particles gyrofrequency $\omega_g = qB/M$, and in a system where $\perp$ and $\parallel$ are defined with respect to the magnetic field. A weakly non-homogeneous magnetic field will result in gradient and curvature drifts. The gradient drift can be expressed as

$$\mathbf{v}_\nabla = \frac{mv_\perp^2}{2qB^3}(\mathbf{B} \times \nabla B), \tag{1.4}$$

which depends upon the charge state of the ion. Positively and negatively charged particles will therefore drift in opposite directions. The circular gyratory motion of a charged particle also results in a centrifugal force, which acts perpendicularly to the curvature radius, r_c, of the magnetic field and causes the curvature drift,

$$v_R = \frac{mv_\perp^2}{q} \frac{\mathbf{r}_c \times \mathbf{B}}{r_c^2 B^2}. \tag{1.5}$$

1.1.2 Maxwell's equations

The Lorentz force law in Equation 1.1, intrinsically couples the motion of each particle and the electric and magnetic fields. To describe a set of charged particles requires a self-consistent methodology. The relationship to the electromagnetic fields can be accurately described by Maxwell's equations.

Faraday's Law of induction states that a time-varying magnetic field induces the electric field,

$$\nabla \times \mathbf{E} = -\frac{\partial \mathbf{B}}{\partial t}. \tag{1.6}$$

Amperes Law states that a time-varying electric field induces the magnetic field,

$$\nabla \times \mathbf{B} = \mu_0(\mathbf{J} + \varepsilon_0 \frac{\partial \mathbf{E}}{\partial t}), \tag{1.7}$$

where $\mathbf{J}$ is the current density, and μ_0 and ε_0 are the magnetic permeability and electric permittivity of a vacuum, respectively.

Gauss' Law states that an electric charge induces an electric field as,

$$\nabla \cdot \mathbf{E} = \frac{\rho_c}{\varepsilon_0}, \tag{1.8}$$

where ρ_c is the charge density.

Gauss' Law for magnetism states that the divergence of a magnetic field must be zero,

$$\nabla \cdot \mathbf{B} = 0. \tag{1.9}$$

1.1.3 Definition of a plasma

A plasma is defined as consisting of an equal number of positive and negative charge carriers that is virtually quasineutral over large distances with sufficient energy to overcome the forces exerted by the nearest neighbour. As a result, these charged particles can be considered as free-moving and experience collective effects. Any temperature or density perturbations will be cancelled out and the plasma will have a net potential of zero in the absence of any externally applied forces. Each individual charge within a plasma will generate an electric Coulomb field, Φ_c, defined as,

$$\Phi_c = \frac{q}{4\pi\varepsilon_0 r}. \tag{1.10}$$

where r is the distance from the charge. This electric field is neutralised by free charge carriers and a Debye potential is defined as,

$$\Phi_d = \frac{q}{4\pi\varepsilon_0 r} exp^{-\frac{r}{\lambda_D}}, \tag{1.11}$$

which acts over the characteristic Debye length scale,

$$\lambda_D = (\frac{\varepsilon_0 k_b T}{n_e e^2})^{\frac{1}{2}}, \tag{1.12}$$

where T is the temperature, n_e is the electron density, and k_b is the Boltzmann constant. Within a plasma, the individual electric fields generated by each charged particle cancel each other out over distances of this Debye length.

The first criterion for the existence of a plasma is defined according to this parameter. This criterion states that the length scales of the plasma, L, must be large compared with the Debye length such that

$$L >> \lambda_D. \tag{1.13}$$

This Debye shielding effect is instigated by electrons present inside the Debye sphere. This effect can therefore only take place if there exists a sufficiently number of electrons within the plasma. A second plasma criterion is thus defined as,

$$n_e \lambda_D^3 >> 1. \tag{1.14}$$

A further plasma state, an ion-ion plasma, can be found when the negative ions charge density exceeds that of the electrons. In this instance the effective Debye length is required, which utilises the shielding of electrons and negative ions by positive ions and the shielding of the positive ions by the negative ions. The effective Debye length is expressed as,

$$\lambda_{D,eff}^{-2} = \lambda_{De,eff}^{-2} + \lambda_{Di,eff}^{-2}, \tag{1.15}$$

where $\lambda_{di,eff}^{-2}$ is the shielding due to an ion component. In the case of multiple ion components, either positively or negatively charged, further like-terms can be added to this expression. When such additional plasma components are very large the plasma can be described as dusty plasma where significantly different collective effects result [*Baumjohann and Treumann*, 1996; *Shukla and Mamun*, 2002].

The first criterion in Equation 1.15 already infers charge neutrality but a third criterion can also specify this directly where, in conjunction with the first two criteria, the number of negative charge carriers must equal the number of positive charge carriers,

$$n_{pos} = n_{neg}. \tag{1.16}$$

The plasma frequency is the rate at which the faster moving electron oscillate about the slower moving ions as a result of the internal restoring force of a plasma acting to oppose a disturbance. This frequency is defined as

$$\omega_{pl} = (\frac{n_e e^2}{m_e \varepsilon_0}), \tag{1.17}$$

where m_e is the electron mass. A fourth criterion for the definition of a plasma derives from this plasma frequency. The presence of neutral particles results in collisions with the fast moving electrons and if the collision frequency, ω_{en}, is higher than ω_{pl}, the electrons cannot be considered free moving and will not be able to act to fulfil the Debye shielding condition. This fourth criterion is defined as

$$\omega_{en} > \omega_{pl}. \tag{1.18}$$

1.1.4 Plasma descriptions

1.1.4.1 Statistical plasma descriptions

There exists several different methods by which a plasma can be mathematically described. The most accurate approach is to solve the equation of motion for each individual particle and the self-consistent interaction with the fields. This can, however, be quite calculation intensive.

A statistical approach can greatly reduce the amount of calculations required. This method

solves for the distribution function of a set of particles in phase space. Phase space or space consists of a six-dimensional space where a particles position and velocity is represented along the x, y and z spatial dimensions at a single point in time as,

$$d^3rd^3v = dxdydzdv_xdv_ydv_z. \tag{1.19}$$

The phase space distribution function takes the form

$$f_\alpha(\mathbf{r},\mathbf{v},t) = \frac{d^6\mathscr{N}_\alpha(\mathbf{r},\mathbf{v},t)}{d^3rd^3v}, \tag{1.20}$$

where $d^6\mathscr{N}_\alpha$ is the number density of species α within volume d^3rd^3v. An example of a statistical formulation used to evolve this distribution function under a given set of conditions is the Vlasov equation,

$$\frac{\partial f_\alpha}{\partial t} + \mathscr{N}\cdot\nabla f_\alpha + \frac{1}{m_\alpha}(\mathbf{F}_{ext} + q_\alpha(\mathbf{E}_i + \mathbf{v}\times\mathbf{B}))\cdot\nabla_V f_\alpha = 0, \tag{1.21}$$

where $\mathbf{F}_{ext}$ corresponds to external forces. The Vlasov equation is derived from the Boltzmann equation and can be solved using Maxwell's equations.

1.1.4.2 Magnetohydrodynamics and Frozen-in Flux

A common approach to describing plasmas is that of magnetohydrodynamics (MHD), which treats plasma as a fluid. This can significantly reduce the calculations required as single particle physics are neglected. The fundamental MHD equations for an incompressible conducting fluid include the continuity equation written as,

$$\frac{\partial\rho_m}{\partial t} + \nabla\cdot(\rho_m\mathbf{v}) = 0, \tag{1.22}$$

where ρ_m is the mass density. This implies the absence of any sources or sinks. The equation of motion specifies that moment is conserved as,

$$\rho_m(\partial\mathbf{v}\partial t + \mathbf{v}\cdot\Delta v) = \mathbf{J}\times\mathbf{B} - \nabla p, \tag{1.23}$$

where p is the total scalar pressure. The conservation of energy is treated adiabatically such that,

$$\Delta p = V_s^2 \nabla \rho_m, \tag{1.24}$$

where $\mathbf{v}$ is the average fluid velocity, ρ is expressed as a scalar quantity and V_s is the adiabatic Mach number.

The generalised Ohm's law can be expressed as,

$$\mathbf{E} + \mathbf{v} \times \mathbf{B} = \frac{\mathbf{J}}{\sigma_o} - \nabla \cdot \mathbf{P_e} + \frac{\mathbf{j} \times \mathbf{B}}{n_e} + \frac{m_e \partial \mathbf{j}}{n_e e^2 \partial t}, \tag{1.25}$$

where $\mathbf{P}_e$ is the electron pressure, e is the charge on an electron, and the electrical conductivity is represented by σ_0. In Ohm's law the four terms on the right-hand side correspond to the resistivity, electron pressure, Hall current term, and time-varying current, respectively.

In the solar wind and within planetary magnetospheres, infinite conductivity is often assumed, which results in the right hand terms being dropped. This results in the idealised Ohm's law,

$$\mathbf{J} = \sigma_0 (\mathbf{E} + \mathbf{v} \times \mathbf{B}), \tag{1.26}$$

also known as Alfvén's frozen-in theorem. The frozen-in condition specifies that the magnetic field will remain fixed to a parcel of plasma. This concept can be quantified by combining the idealised Ohm's law with Faraday's and Ampere's law to provides the MHD induction equation,

$$\frac{\partial \mathbf{B}}{\partial t} = \nabla \times (\mathbf{v} \times \mathbf{B}) + \frac{1}{\mu_0 \sigma} \nabla^2 B. \tag{1.27}$$

Here, the two right-hand terms describe the magnetic field evolution with respect to convection and diffusion, the ratio of which provides the magnetic Reynold's number,

$$R_m = \frac{\nabla \times (\mathbf{v} \times \mathbf{B})}{\frac{1}{\mu_0 \sigma} \nabla^2 \mathbf{B}}. \tag{1.28}$$

This term is often reduced to a characteristic length scale multiplied by a characteristic velocity scale as a quick and easy method for analysing how frozen in the magnetic field is. When the magnetic Reynolds number greatly exceeds unity, the magnetic field can be viewed as fixed to the plasma. Despite the frozen-in approximation dominating in many space environments, many scenarios exist where it does not. These include at the boundaries and interactions of different

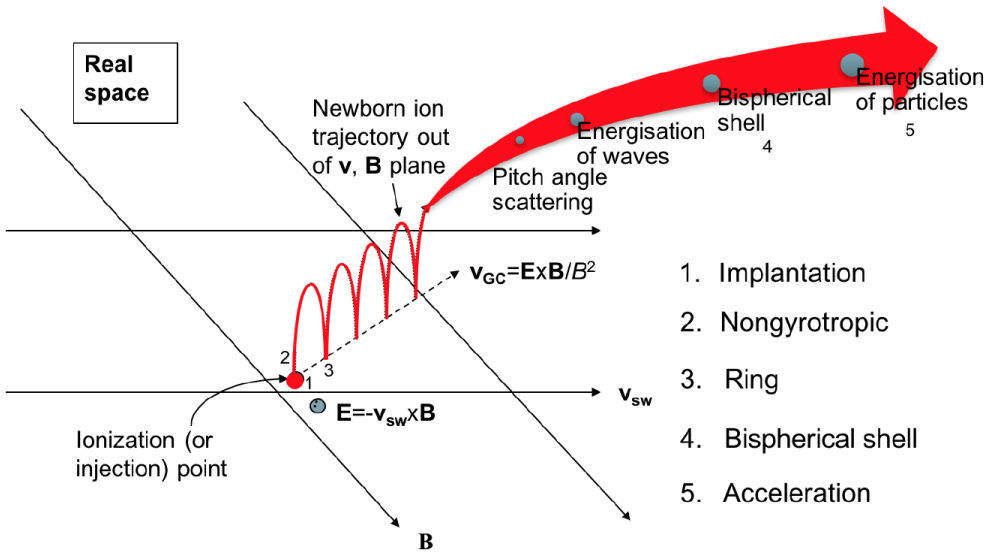

Figure 1.1: Summary of stages in the ion pickup process *[Coates 2017]*.

plasma regimes and where forces drive a plasma unstable. This can result in kinetic processes such as magnetic reconnection and plasma instabilities dominating.

1.1.5 Ion pickup & wave generation

When a neutral molecule is ionised it can be accelerated or 'picked up' by ambient electric fields and follow paths subscribed by single particle motion. In a homogeneous magnetic field, pickup ions move through a ring in velocity space and, when the pickup ions are produced across a spatial domain greater than the ion gyroradius, the pickup ions will form ring distributions in velocity space. This ring distribution results in a $T_\perp > T_\parallel$ anisotropy in velocity space, where $\perp$ and $\parallel$ are defined with respect to the magnetic field, and the generation of near circularly polarised field-aligned electromagnetic waves [*Wu and Davidson*, 1972]. These waves have been observed in the solar wind at comets, Mars and Venus [*Thorne and Tsurutani*, 1987; *Barabash et al.*, 1991; *Delva et al.*, 2008], in the Earth's polar wind [*Le et al.*, 2001], and within the Jovian and Kronian magnetospheres [*Kivelson et al.*, 1996; *Leisner et al.*, 2006]

Figure 1.1 shows the various stages of this process for ion pickup within the solar wind. The electric field can be seen to result from the motional plasma via the $-\mathbf{v} \times \mathbf{B}$ product, which accelerates the pickup ions. Waves consequently grow along the Alfvén branch and are damped by an ion cyclotron resonance. This interaction leads to the pickup ions being scattered along paths marked by two distinct rings in velocity space, each ring centred on the parallel and antiparallel wave velocity. The ions scatter along surfaces where the sum of the plasma and wave velocities

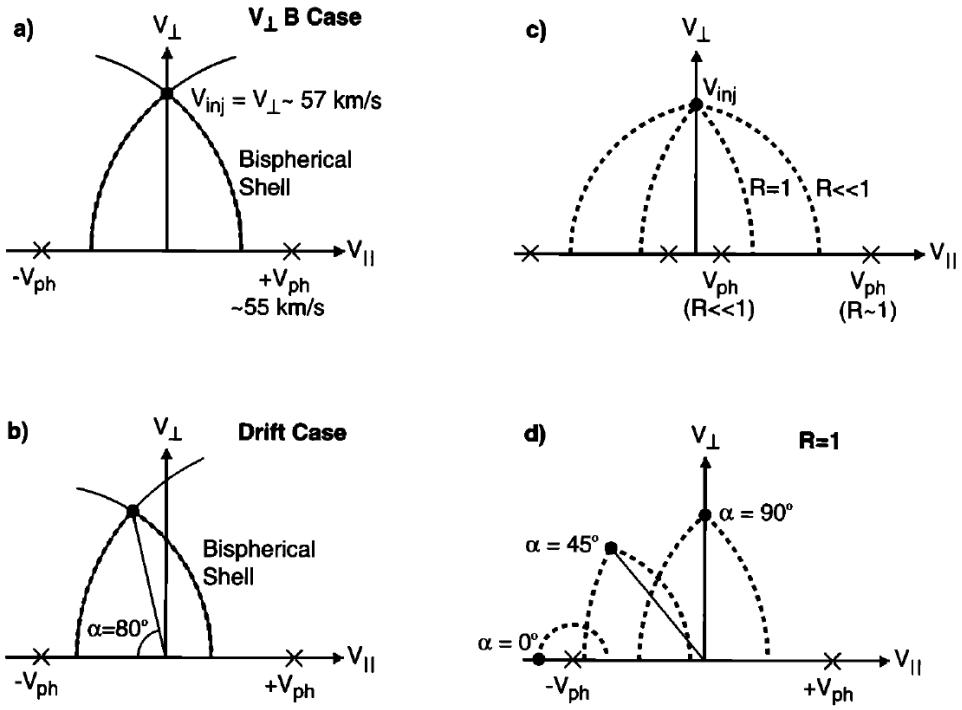

Figure 1.2: Velocity-space scattering paths of the pickup ion distribution for varying pickup geometries [*Huddleston et al.*, 1998]. (a) illustrates the paths along which the particles scatter into a bispherical shell distribution, (c) illustrates the effect on this distribution of the varying ratio $R = v_{ph}/v_{inj}$ where v_{ph} is the wave phase velocity and v_{inj} is the pickup velocity, and (c) and (d) illustrate the effect of a varying pickup angle. $\perp$ and $\parallel$ are still defined with respect to the background magnetic field.

remain constant from their initial location, their 'injection point'. As the pickup ions scatter in velocity space and pitch angle, they therefore scatter into a 'bispherical' shell distribution in velocity space [*Johnstone*, 1988; *Huddleston and Johnstone*, 1992; *Coates et al.*, 1989, 1990, 1993]. The scattering paths for various orientations of the magnetic field with respect to the plasma velocity are shown in Figure 1.2. The waves primarily travel in the direction parallel and antiparallel to the magnetic field [*Wu and Davidson*, 1972; *Huddleston et al.*, 1997; *Cowee et al.*, 2006] although oblique propagation angles can also result [*Cowee et al.*, 2007]. The presence of background thermalised ion populations of a similar mass will undergo cyclotron resonant interactions with the waves, which are heated as this interaction acts to damp wave growth.

This pickup ion-generated instability is often called the ion cyclotron temperature anisotropy instability or the Alfvén-Cyclotron instability, The resultant waves are termed Ion Cyclotron Waves (ICWs) as they will be referred to hereafter. These modes are unstable if the resonant condition,

$$\omega - \mathbf{k} \cdot \mathbf{v_b} - m\Omega_i = 0, \tag{1.29}$$

is satisfied, where ω is the wave frequency, $\mathbf{k}$ is the wavenumber, $\mathbf{v_b}$ is the bulk velocity, Ω_i is the ion gyrofrequency, and m is specified as an integer representing the ion mass.

Plasma instabilities can be defined as either macro or micro in scale. A plasma instability is characterised by an exponential growth in the electric or magnetic fluctuating field energy density. A linear dispersion relation for this phenomenon can be derived from the Vlasov equation in accordance with Maxwell's equation by introducing a perturbation to a stable system and finding the roots, which correspond to the various oscillatory modes [*Stix*, 1992; *Gary*, 1993]. This theoretical method is valid in the limit of small amplitudes where the perturbations do not significantly alter the a priori state of the system.

A typical pickup ion ring distribution can be defined as,

$$f(\mathbf{v}_\parallel, \mathbf{v}_\perp) = \frac{n\, exp(-(\mathbf{v}_\parallel - \mathbf{v}_b)^2/\mathbf{v}_{th\parallel}^2 exp(-(\mathbf{v}_\parallel - \mathbf{v}_b)^2/\mathbf{v}_{th\parallel}^2))}{\pi^{3/2}\mathbf{v}_{th\parallel}\mathbf{v}_{th\perp}^2(\pi^{1/2}(r)erfc(r) + exp(r^2))}, \tag{1.30}$$

where n is the number density, $r = \mathbf{v}_r^2/\mathbf{v}_{th\perp}^2$, v_r and v_b are the ring and bulk plasma velocities, and *erfc* is the complementary error function, and the thermal velocity $v_{th}^2 = 2k_bT/m$ [*Huddleston et al.*, 1997]. The dispersion relation for parallel propagation is expressed as,

$$c^2k_\parallel^2 = \omega^2 \sum_i \omega_{pl}^2(-\zeta_0 Z(\zeta) + \frac{Z'(\zeta)}{2}\frac{\mathbf{v}_{th\perp}^2}{\mathbf{v}_{th\parallel}^2}(1 + r^2 - \frac{\mathbf{v}_{th\parallel}^2}{\mathbf{v}_{th\perp}^2} + \frac{1}{2}\frac{r\pi^{-1/2}erfc(-r)}{r\pi^{-1/2}erfc(-r) + exp(-r^2)})), \tag{1.31}$$

where ω is the wave frequency, ω_{pl} is the plasma frequency, c is the speed of light, $\zeta = (\omega - k_\parallel v_b)/k_\parallel v_\parallel$, $Z(\zeta)$ is the plasma dispersion function, $Z(\zeta) = \partial Z\ /\partial\zeta$ [*Fried and Conte*, 1961]. Solutions to the dispersion relation are inherently complex. The real part of the solution yields the wave frequency and the imaginary part yield the growth rate, both often expressed as a function of wave number.

In some plasma environments, such as in the Earth's magnetosheath [*Hasegawa*, 1969; *Remya et al.*, 2013] and in Saturn's middle magnetosphere [*Russell et al.*, 2006], an increased plasma beta results in a further plasma mode, the Mirror Mode, dominating over the Alfvén-Cyclotron

mode. The plasma beta is defined as the ratio of thermal plasma pressure to magnetic pressure,

$$\beta = \frac{nk_bT}{B^2/2\mu_0}. \tag{1.32}$$

The competition and cogeneration of the two modes is the subject of much interest and Mirror Mode structures in the solar wind have been highlighted as a possible messenger of Alfvén-Cyclotron heating within the solar corona [*Russell et al.*, 2008].

1.2 Plasma structures

1.2.1 Astrophysical dynamos

Within astrophysical bodies, convecting and conducting fluids are able to generate magnetic fields called astrophysical dynamos, which persist over astronomical timescales. There exist three criteria for the formation of a dynamo; an electrically conductive fluid, energy made available through angular momentum, and a further energy source, which is able to drive convective motions within the fluid. The generation of the magnetic field consequently results from the MHD induction equation provided in Equation 1.27. The generated magnetic field is often nominally dipolar at planetary bodies but at larger astrophysical bodies, such as stars and black holes, higher order and even toroidal terms can dominate. More complex dynamo theory descriptions also include kinetic variations where the Lorentz force becomes significant. This magnetic field generated by a dynamo can extend far beyond the surface of the body itself and dominate the dynamics of the local space environment [*Larmor*, 1919; *Parker*, 1955; *Roberts*, 1987].

1.2.2 The Heliosphere

The sun is a main sequence star of spectral type G2 and magnitude 4.8. It emits 3.9 $\times$ 10^{26} W of radiation every second and $\sim 10^9$ kg s^{-1} of ionised gas. This magnetised plasma expands supersonically at 300-900 km s^{-1} and consists of electrons, protons and 5% Helium ions as well as traces of heavier elements such as oxygen and iron. The frozen-in condition defined in Equation 1.26 nominally holds within the solar wind and the rotation of the sun results in the formation of an "Archimedes" or "Parker" spiral, as the solar wind moves radially outwards and magnetic field lines stay connected to fixed location on the sun's surface [*Parker*, 1958; *Schrijver and Siscoe*, 2012].

The solar wind is a chaotic turbulent environment with similarly large-amplitude fluctuations

in pressure, density and velocity at all scales larger than ion inertial scales. Near the ion and electron inertial scales a range of kinetic instabilities exist which represent fundamental differences to the otherwise analogous phenomenon of hydrodynamic turbulence [*Schwenn and Marsch*, 1991].

The region dominated by the solar wind is termed the heliosphere and shelters the solar system from external forces such as Galactic Cosmic Rays (GCR). It is important to note however that this definition of the heliosphere is magnetically based and stars which don't possess significant internally generated magnetic fields, such as the majority of high luminosity stars, might require a different definition of a heliosphere.

1.2.3 Planetary magnetospheres

A planetary magnetosphere is generated by the interaction between a planetary dynamo and the solar wind. The solar wind, if supersonic and supra-Alfvénic, is first slowed down over a boundary termed the planetary bow shock. This plasma structure represents a solution to the warm plasma dispersion relation, which slows and heats the solar wind plasma, as described by the Rankine-Hugoniot jump conditions [*Macquorn Rankine*, 1870]. This phenomenon is present during the vast majority of instances at planets within our solar system. Inside the bow shock a region called the magnetosheath hosts turbulent plasma populations which, due to the force of the impinging solar wind, presses upon the characteristic surface of the magnetosphere, the magnetopause. This boundary represents a dynamic pressure balance between the shocked solar wind and planetary magnetic field and is located at the Chapman-Ferraro distance. Behind the planet a magnetotail stretches out to much greater distances than the magnetosphere occupies in front of the planet and which consists of a northern and southern lobe. These are separated by a plasma sheet where the plasma number density is notably higher and the magnetic field direction reverses orientation [*Kivelson and Russell*, 1995].

1.2.4 Magnetosphere driving

Planetary magnetospheres can host fundamental rhythms which can be driven by external or internal influences. The magnetosphere of the Earth, Mercury, and Saturn to a lesser extent, are driven by the solar wind whereas Jupiter's and Saturn's magnetospheres are internally driven. The magnetospheres of Uranus, Neptune and Ganymede have yet to be characterised in terms of a fundamental driving mechanism.

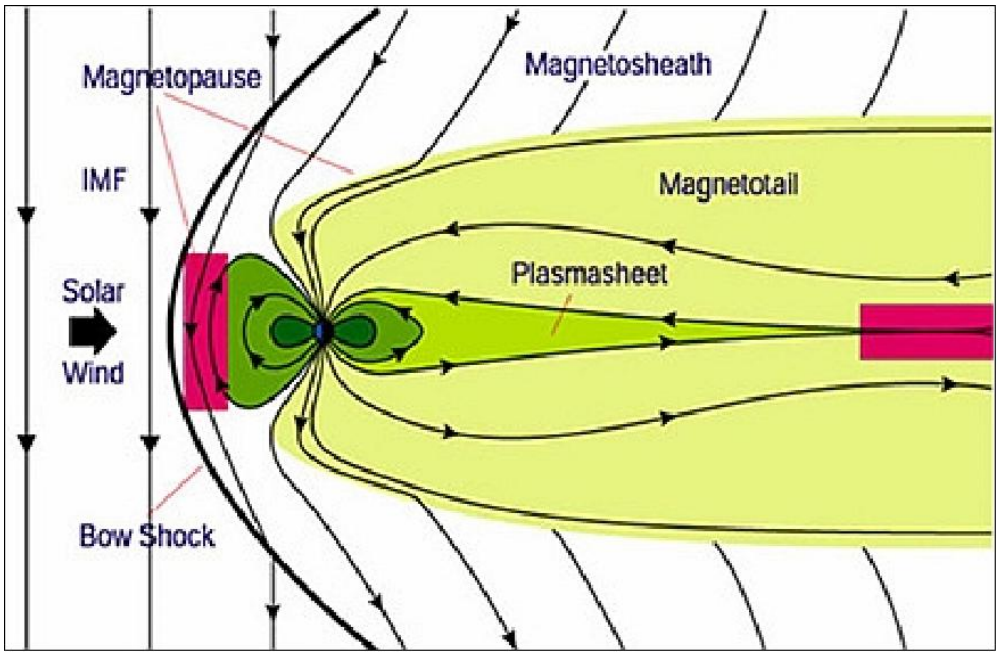

Figure 1.3: Two-dimensional schematic of the Earth's magnetosphere demonstrating its interaction with the Interplanetary Magnetic Field (IMF) carried by the Solar Wind [*SWRI*, 2018]. The red regions indicate where reconnection results in reconfigurations of the magnetic field topology and the transfer of flux across the poles. The cycle of these events constitutes the Dungey cycle.

1.2.4.1 Dungey Cycle

The solar wind driving of a magnetosphere is characterised by the Dungey Cycle [*Dungey*, 1961]. Here, southward Interplanetary Magnetic Field (IMF) lines magnetically reconfigure themselves to reconnect with the planetary magnetic field lines at the magnetopause, which allows the solar wind plasma to enter the magnetosphere. The motion of the solar wind drags these field lines past the planet and the solar wind plasma is able to travel into the magnetosphere. Further reconnection events are subsequently triggered in the magnetotail, which results in precipitation of plasma onto the planetary atmosphere causing the phenomenon of aurora. A plasmoid can also be released from the tail reconnection site in the anti-sun direction. The presented in Figure 1.3, shows the Earth's magnetosphere in the midst of such a Dungey cycle.

1.2.4.2 Vasyliunas Cycle

Planetary magnetospheres can also be driven by internal plasma sources. In Jupiter's magnetosphere the volcanic moon Io emits an estimated 1 tonne of neutral material [*Broadfoot et al.*, 1979], which becomes ionised and picked up according to the process described in Section 1.1.5. This hot plasma bloats the magnetosphere and provides an internal pressure source, which

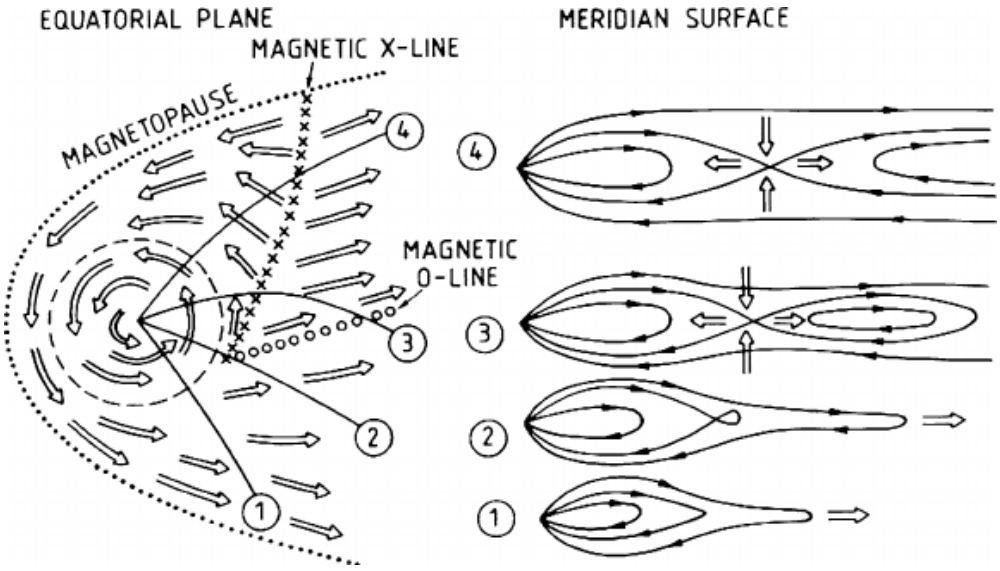

Figure 1.4: Schematic of the Vasyliunas cycle [*Vasyliunas*, 1983].

greatly increases the size of the magnetosphere and distance to the magnetopause. At Saturn, Enceladus provides an internal plasma source, which emits approximately an order of magnitude less material than Io does [*Dougherty et al.*, 2006].

The presence of an internal plasma source results in the the solar wind having a reduced impact on magnetospheric dynamics. Internal plasma can still be accelerated along magnetic field lines to generate aurora and control magnetosphere dynamics by triggering tail reconnection and plasmoid ejection. Such an internally driven rhythm is known as the Vasyliunas cycle. This is schematically shown in Figure 1.4.

The presence of an internal plasma source results in the formation of a magnetodisk. This is an equatorial sheet of plasma, which rotates rapidly, pulled along by planetary magnetic field lines, which are embedded into the planet's ionosphere. This disk stretches the field outwards such that at greater radial distances the magnetic field is no longer dipolar and the radial component dominates. The rapidly rotating plasma also induces a strong corotational electric field, which in turn accelerates the newly ionised material, the ultimate energy source deriving from the planet's angular momentum. Although the Earth does not possess a mass loading moon, ionospheric material forms a plasmasphere in the inner magnetosphere, which results in a ring current and a corotational electric field.

1.2.5 Induced magnetospheres

Unmagnetised planetary bodies that posses a substantial atmosphere can host an induced magnetosphere. This has been observed at comets [*Alfvén*, 1957] and at Venus, Mars and Titan [*Russell and Vaisberg*, 1983; *Ness et al.*, 1982; *Schwingenschuh et al.*, 1992]. Here, the frozen-in magnetic field is unable to pass through the body's conducting ionosphere and consequently drapes around the obstacle. This forms a magnetic structure with many similarities to an internally generated magnetic field, including an extended magnetotail and an often well defined magnetopause. Magnetic reconnection can occur within these magnetotails, which results in the ejection of plasmoids [*Eastwood et al.*, 2008; *Zhang et al.*, 2012]. This is also the mechanisms by which comets lose their tails during periods of strong solar activity.

1.2.6 Ionospheres

An ionosphere is a region of a planetary atmosphere that contains a significant amount of both ionised and neutral material. The electric conductivity is therefore characterised by both Coulomb and neutral collisions. The dominant ionisation source at the Earth, and in the majority of known ionospheres, are solar ultraviolet photons, which exist in energy states high enough to ionise neutral atoms to produce photoeletrons and ions. Impinging electrons and ions form a secondary ionisation source and become the primary source during the night. Electrons are also able to attach to neutral species to form negative ions. These can in some instances exceed the electron density and produce an ion-ion plasma. The chemical recombination of positive ions and electrons, and photodetachment of negative ions, are the mechanisms by which the ionosphere maintains a partially ionised state.

Ionospheric current systems are driven by precipitating plasma along the field lines. These can become intense during solar storms where increased fluxes of solar wind plasma precipitate along magnetic field lines entering the atmosphere at the poles. At the Earth, these current systems can be measured by ground magnetometers and used as a measure of geomagnetic activity. The motion of the neutral atmosphere is also able to generate current systems due to coupling between the ionosphere and thermosphere.

Within the uppermost atmospheric layer, atmospheric losses will primarily consist of ionospheric material. At magnetised planets, field-aligned potentials are able to pull plasma out in a

phenomenon called the polar wind. This is also observed along draped field lines at unmagnetised planets [*Coates et al.*, 2015]. The collisionless nature of the outer ionosphere and exosphere, also facilitates Jeans escape where random ballistic particle motion will result in particles escaping the bodies gravitational sphere of influence known as the Hill sphere. Pickup ionisation can also play a dominant role at unmagnetisted objects such as comets, Mars and Venus, and the moons of the outer planets.

The outer layer of the atmosphere is termed the exosphere and merges with the local space environment. Airless bodies such as Mercury, the moon and icy moons of the outer planets can also host tenuous exospheres although these have so far been observed as not being able to sustain appreciable current systems. The primary source of this ionised material is surface-sputtering and sublimation and the loss mechanisms are Jeans escape and pickup ionisation [*Kivelson and Russell*, 1995; *Baumjohann and Treumann*, 1996].

Ionospheric plasma can be the source of increased chemical complexity compared with space plasmas due to a greater variety of species deriving from the neutral atmosphere or planetary surface. Chemical processes can therefore act as the primary sources and sinks of many plasma populations.

1.3 Negative ion molecular physics

The presence of negative ions in space plasmas can result from a variety of different production mechanisms and as such requires an understanding of negative ion atomic physics relevant to gas phase chemistry. The material described hereafter is derived from the fundamental works of *Massey* [1976], which has been used extensively for examining negative ion chemistry in planetary and cometary environments [e.g. *Vuitton et al.*, 2009a; *Cordiner and Charnley*, 2014].

1.3.1 Electron Affinity

The electron affinity (EA) of a molecule describes its ability to attract and retain electrons. This quantity is measured as an energy and defined as the difference between a neutral atom and when an electron is captured to form a negative ion as,

$$X + e^- \rightarrow (X^-)^* \rightarrow X^- + energy. \tag{1.33}$$

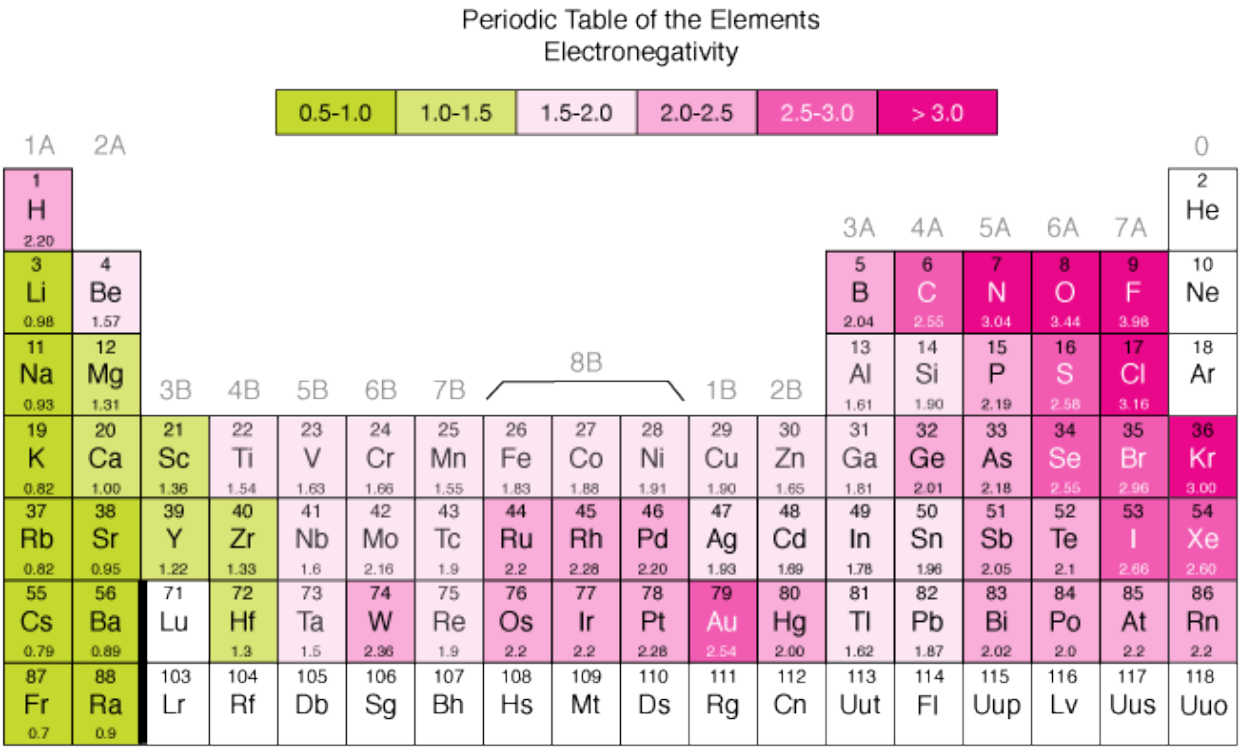

Figure 1.5: Periodic table displaying the Electron Affinities in eV [*Xaktly*, 2014].

The EA can be either a positive or negative quantity and only molecules with a positive EA are able to exist in a stable negatively charged state. The first gas phase negative ion was discovered by Thompson in 1907 since which ∼80% of elements in the periodic table have been discovered to possess a positive EA. A periodic table, which denotes the EA of each element is present in Figure 1.5.

1.3.2 Proton Affinity

A further useful property is the proton affinity of a given molecule, which describes the ability of a molecule to retain or lose a proton. The Gas Phase Acidity is the Gibbs free energy given by the reaction,

$$AH \rightarrow A^- + H^+. \tag{1.34}$$

The enthalpy change of this reaction provides the proton affinity.

1.3.3 Formation and loss mechanisms

1.3.3.1 Radiative electron attachment

Electrons can radiatively attach onto neutral molecules with a positive electron affinity via the reaction,

$$A + e^- \rightleftharpoons (A^-)^* \rightarrow A^- + h\nu, \tag{1.35}$$

where h is the planck constant and ν is the frequency of a photon, where the multiple of these two represents the photon energy. This occurs via a two-step process where the molecule initially gains an excited metastable negative charge state. This can relax into a stable state through emitting either an electron or photon, $h\nu$.

1.3.3.2 Dissociative electron attachment

Electrons with higher suprathermal energies are able to dissociate neutral species and form negative ions via,

$$AB + e^- \rightarrow A^- + B. \tag{1.36}$$

The energy of the electron necessarily has to be greater than the bond between the dissociative products in their initial paired state.

1.3.3.3 Polar photodissociation

Solar photons primarily act to photoionise neutral molecules but, in a minority of instances, they dissociate a given molecule to form a negative ions via,

$$AB + h\nu \rightarrow A^- + B^+. \tag{1.37}$$

1.3.3.4 Photodetachment

Solar photons, which have energies higher than the electron affinity of a negative ion, can be absorbed by an anion and cause the emission of an electron,

$$A^- + h\nu \rightarrow A + e. \tag{1.38}$$

1.3.3.5 Mutual neutralisation and Recombination

Negative ions can be lost through interactions with positively charged particles. In a process known as mutual neutralisation, a positive and negative ions will interact as,

$$A^- + B^+ \rightarrow A + B, \tag{1.39}$$

and both become neutralised. Positive and negative ions will also interact and recombine via,

$$A^- + B^+ \rightarrow AB \tag{1.40}$$

and cancel out their charge states.

1.3.3.6 Associative detachment

Negative ions can attach onto neutral molecules and produce a metastable negative ion. This occurs via,

$$A^- + B \rightarrow (AB^-)^* \rightarrow AB + e, \tag{1.41}$$

and results in the ejection of an electron.

1.3.3.7 Charge transfer

A neutral can become negatively charged from the loss of a proton as it is transferred onto another negative ion via,

$$AH + B^- \rightarrow A^- + BH. \tag{1.42}$$

It is also possible for the negative charge to transfer directly via

$$A^- + B \rightarrow A + B^-. \tag{1.43}$$

1.3.3.8 Polymerisation

A further class of reactions exist which involve the production of higher order negative ions. For example the C_nH^- anions, where $n = 2,4,6...$, can produced via

$$C_nH^- + C_2H_2 \rightarrow C_{n+2}H^- + H_2, \tag{1.44}$$

which shows how smaller charged particles can facilitate the production of larger charged molecules via polymerisation processes.

1.3.4 Further negative ion states

The aforementioned negative ion production and destruction mechanisms result purely from the physics of the valence shell of a molecule. These can result in singly charged negative ions as have been observed in a range of space environments. Observations of these are described within the following chapter.

It is however possible for an atom to capture two excess electrons although this has as yet only been observed within the laboratory. It is also possible for a molecule to capture an excess electron via long-range forces resulting from a strong dipole-moment. Such negative ions are termed dipole-bound anions. Exotic anionic states such as multiply charged and dipole-bound anions are the subject of much experimental and theoretical research within fundamental physics due to their relevance to quantum correlation properties. Techniques such as electrospray ionisation and Rydberg electron transfer have recently been able to produce exotic negative ions in the gas phase for the first time. [e.g. *Arn*, 2009].

Chapter 2

Negative Ions in Atmospheric and Space Environments

Negative ions have been found to inhabit a diverse range of environments from the Suns' photosphere to diffuse interstellar environments and within a range of Cometary and Planetary systems. In these environments they can have remarkable consequences, significantly altering the physical characteristics of the medium they populate

This chapter reviews the current observations of negative ions in atmospheric and space environments in a roughly chronological order with respect to when the various detections were made, and how the understanding of these species evolved.

2.1 The Sun and Stars

Prior to 1939, the opacity of the outer layers of the Sun's atmosphere provided a long standing mystery to astronomers.

Stellar opacity can be produced by three different physical processes: Photons can cause electrons to transition from one bound atomic state to another, 'absorption', from a bound state to a free state, 'photoionisation', and from one freely ionised state to another in the vicinity of an ion, 'bremsstrahlung'. As photoionisation dominates, the Sun's structure was thought to result in opacity described by Kramer's Law, which predicts the opacity to vary as function of the density and temperature as $\rho T^{-7/2}$. Observations however showed the Sun as uniformly opaque with an unexplained source of opacity in the outer layers

This presented a serious puzzle as this could only be explained by metallicity ratios (the ratio of hydrogen and helium to heavier elements) of the order of $\sim$50:1, which were over an order

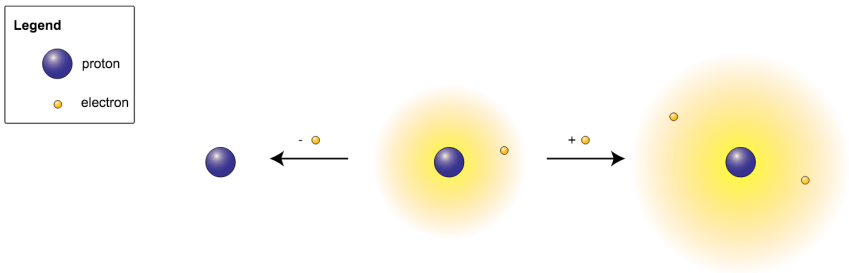

Figure 2.1: Schematic of a neutral hydrogen atom (middle), a hydrogen atom losing an electron (left), and a hydrogen atom gaining an electron (right). Image credit: Jkwchui.

of magnitude larger than the observed abundances of ∼1000:1 . While initial efforts focused on reformulating Kramer's law for these heavier elements [e.g. *Page*, 1938; *Unsöld*, 1939], it was *Wildt* [1939] who first showed that the observed opacity was consistent with the Hydrogen anion, H^-, through calculation of its absorption coefficient. Following this, *Chandrasekhar and Krogdahl* [1943] provided the fundamental quantum calculations justifying this hypothesis and showing this theory held true for cool stellar atmospheres with photospheric temperature of <7000 K.

The H^- anion is loosely bound with an electron affinity of 0.754 eV. This allows electrons produced by ionisation of the low-energy states of alkali metals, such as Sodium and Potassium, to add an electron to the valence shell via reaction,

$$H + e^- \rightarrow H^-. \tag{2.1}$$

The significance of this concept is that for H^-, as a two electron and one proton system, an infinity amount of ionised states are available for the additional electron which are sensitive to optical photons. The bound-free transitions of H^- therefore provides continuum opacity at visible and near-infra-red wavelengths via photon absorption via reaction,

$$H^- + h\nu \rightarrow H + e^-, \tag{2.2}$$

and results in stellar opacity deviating from that predicted by Kramer's law. The hydrogen anion is also able to interact with further electrons to provide a unique type of bremsstrahlung, which also contributes to the observed opacity. Abundances of H^- exist in a narrow radial range where the electrons have temperatures low enough to facilitate Reaction 2.1, yet with densities high enough

for sufficient electron densities.

This discovery showed how the hydrogen anion has an important effect on the large-scale characteristics of the Sun and other cool stars.

2.2 The Early Universe

The hydrogen anion has also been shown to be instrumental to the formation of molecular hydrogen during the re-ionisation epoch in the early Universe [*McDowell*, 1961]. At this time, just a few hundred thousand years after the Big Bang, temperatures reached a few thousand kelvin and electrons and protons were able to recombine to form neutral hydrogen atoms. These conditions allowed electrons to radiatively attach onto hydrogen atoms, see Reaction 2.1, which was closely followed by the associate detachment reaction,

$$H^- + H \rightarrow H_2 + e^-. \tag{2.3}$$

This was significant as molecular hydrogen was able to undergo rotational-vibrational and quadrupole transitions previously unseen in the universe. These mechanisms efficiently dissipated thermal energy and, even at extremely low fractional abundances of 1 ppm, allowed the gas cooling time to reach a critical level with respect to the expansion rate of the Universe. This facilitated the Jeans instability, which drove gravitational collapse and the formation of large stellar masers, as shown in Figure 2.2, which shows the rapid increase in molecular hydrogen density correlating with a decrease in electron density and subsequent growth of these large stellar masers.

2.3 The Interstellar Medium

After the first stars in the Universe entered their death throes and produced heavier elements, rich organic chemistry has taken place in vast molecular clouds.

The presence of molecular anions in dark interstellar clouds was first postulated by *Dalgarno and McCray* [1973]. Here, contrary to in the early universe, the formation of molecular hydrogen readily occurs via grain chemistry and *Dalgarno and McCray* [1973] theorised that the H^- and O^- anions could be produced and could facilitate the production of more complex species via associate detachment reactions. S^- and C^- were also considered in this vein and this study also first postulated the formation of the carbon chain anions, CH^-, C_2H^- and CN^-.

Following this, *Sarre* [1980] explained how linear anions with large dipole moments such

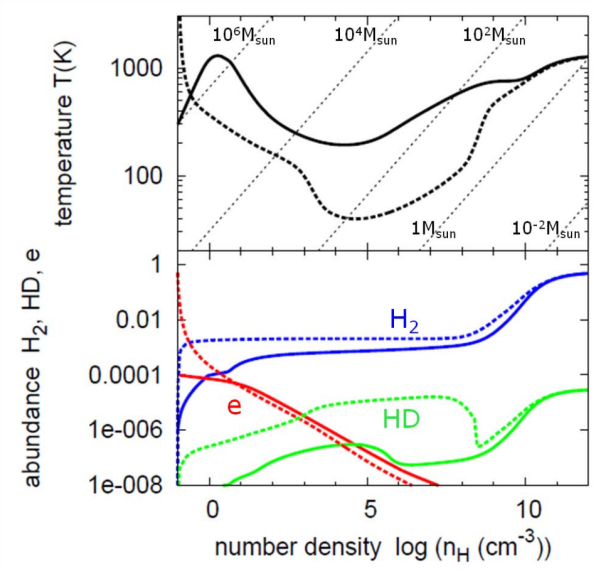

Figure 2.2: *Galli and Palla* [2013]'s calculations of the thermal evolution of a collapsing gas cloud in the early Universe presented in comparison with the abundance of molecular Hydrogen, key to causing this collapse. The scenarios of a pre-ionised gas cloud (dashed line) and that of a neutral cloud (solid line) are depicted.

as C_2^-, C_2H^- and CN^- could result in strong rotational transition line intensities, which might be observed in the laboratory and in space. He went on to outline the key reaction sequences of proton transfer, dissociative electron transfer, charge exchange, and radiative attachment, which could produce molecular anions. *Herbst* [1981] then provided the first quantitative estimates of abundances. This study predicted that the radiative attachment process was efficient enough to result in abundances of 0.01-0.1 of their neutral counterparts of the following linear molecular anions, C_4H^-, C_nN^- where n=3,5,7,9, $C_2H_3O_n^-$ where n=1,2, as well as the branched molecular anion CH_2CN^-.

The first definitive detection of anions in these environments was however only made in 2006 following the ability of *McCarthy et al.* [2006] to accurately measure anion emission spectra in the laboratory. Here, *McCarthy et al.* [2006] definitively attributed a number of millimetre and sub-millimetre emission lines detected towards the carbon star CW Leonis IRC+10216 and TMC-1, as deriving from C_6H^-, as shown in Figure 2.3. These anions were observed to exist with anion-to-neutral ratios of between 1% and 5%, thus confirming earlier predictions [*Herbst*, 1981; *Millar et al.*, 2000]. Following this, the number of detections increased rapidly with $C_{n-1}N^-$ and C_nH^- anions, where n=2-6, being shown to reside in dark molecular clouds, prestellar cores or protostellar envelopes, although the cyano species have not yet been observed in the dark clouds

[*McCarthy et al.*, 2006; *Brünken et al.*, 2007; *Cernicharo et al.*, 2007, 2008; *Thaddeus et al.*, 2008; *Agúndez et al.*, 2010] . Further information on the various detections and the calculated column densities can be found in Table 1 in *Millar et al.* [2017].

Larger anions have been considered in a number of studies. *Bettens and Herbst* [1996] included C_n^- and C_n^-H anions with up to 23 carbon atoms in studies of fullerene formation and *Terzieva and Herbst* [2000] consequently showed how in these cold environments, every collision between an electron and a molecule containing >6 carbon atoms would result in the formation of a molecular anion.

The study of even larger negatively charged molecules were conducted by *Lepp and Dalgarno* [1988] who showed how electron attachment to Polyaromatic Hydrocarons (PAH) could result in negatively charged PAH molecules carrying more of the negative charge density that free electrons. A comparable result was also obtained by *Harada and Herbst* [2008] when simulating the chemistry in the dark core L1527. Although this study did not focus on PAHs, it was found that the molecular anion number density could also exceed that of the electrons, thus significantly altering the characteristics of the medium.

The study of interstellar anion chemistry is surely the most mature due to an accumulation of research over nearly 35 years. The advent of a new generation of powerful telescopes, will provide further insight into further negative anions in a greater range of interstellar environments. Limitations also exist regarding the laboratory characterisation of anion spectra. Larger linear anions possess a greater dipole moment but models show abundances of these species are lower than the smaller anions. Even more massive molecules such as the C_{60} Buckminster fullerene have also been detected in the ISM [*Berné et al.*, 2013] and the quantification of anion chemistry at this scale is still in its infancy.

2.4 The Earth's Ionosphere

The Earth's ionosphere extends from 60 km to 1000 km above the surface of which 60-90km, and 90-150km, make up the D and E regions, respectively. Large quantities of negative ions have been observed in these regions which results in some of the most complex chemistry in the Earth's atmosphere. The ionospheric plasma in the D and lower E regions is collisional and the negative ion abundance influences electron densities.

The first published mention of negatively charged ions was by *Appleton et al.* [1933] who at-

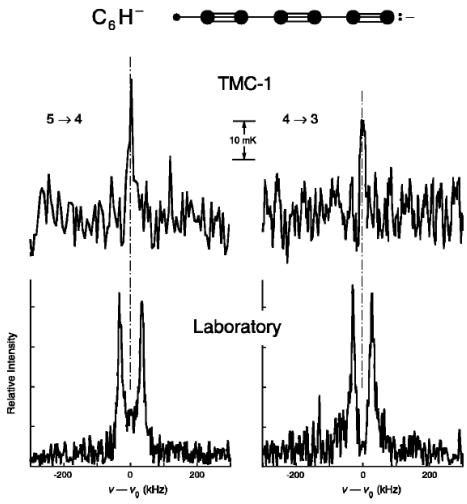

Figure 2.3: First astronomical identification of the carbon chain anions C_6H^-. The data show two rotational transitions in the laboratory (lower panels) and observed in TMC-1 (upper panels). A schematic of this linear molecule is also show above the four panels [*McCarthy et al.*, 2006].

tributed the depletion of electrons responsible for reflection of radio waves to be due to attachment to abundant atomic oxygen as well as recombination with positive ions. Following this, candidate atmospheric negative ions, such as O^- and O_2^-, received considerable theoretical interest [e.g. *Martyn and Pulley*, 1936; *Bradbury*, 1938; *Massey*, 1937], but it wasn't until the 1960s that understanding of these species really evolved. This was due to the increasing number of sounding rockets flown in this era which were able to obtain in-situ spectroscopic measurements. The first sounding rocket obtained mass spectroscopic measurements of negatively charged ions in 1956 [*Johnson et al.*, 1958] a result followed by a number of further flights in the following decades [e.g. *Narcisi et al.*, 1971].

Negative ion chemistry was determined to result from the initial formation of O^- and O_2^-, which generate a cascade of reactions resulting in larger 'cluster' ions of the form $X^-H_2O_n$ where X could for example be O, O_2, O_3, O_4, CO_3, CO_4, NO_2, NO_3, HCO_3, and where n is an integer. The extensive number of negative ions observed precludes the extensive discussion of each species but the interested reader is referred to *Pavlov* [2014, Table 8-9 therein].

These ionospheric regions near 90 km are notoriously difficult to study due its inaccessibility to satellites and mass spectroscopic measurements acquired by sounding rockets lacking large-scale coverage. Negative ion populations can however also be studied through analysis of the Thomson Scatter Power Spectrum obtained from radar measurements [*Tepley et al.*, 1981]. This method has proven useful and some of the more powerful radar facilities, such as Arecibo and

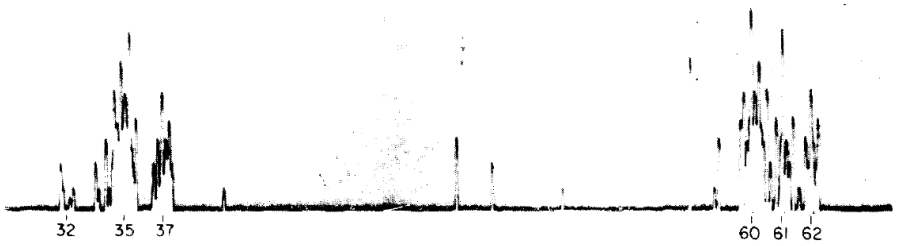

Figure 2.4: Mass spectrometric measurements of negative ions from an early sounding rocket showing strong detections near 32, 35 and 60 and 62 u [*Johnson et al.*, 1958].

Jicamarca, have proven capable of measuring the negative ion-to-electron ratio down to altitude as low 65 km [*Ganguly et al.*, 1979; *Gong et al.*, 2017]. Figure 2.5 shows such a measurement reported by *Gong et al.* [2017], which shows how the negative ion density can exceed those of the electron in this environment resulting in an ion-ion plasma. The modelled abundances of [*Fritzenwallner and Kopp*, 1998] are also shown for comparison.

Negative ions in the Earth's ionosphere have primarily been detected in the mass range of 16-152 u although *Schulte and Arnold* [1992] reported mass spectroscopic detections of negative ions with masses up to, and exceeding, 473 u. It has proposed that metallic dust particles resulting from micrometeorite ablation could become negatively charged *Arnold et al.* [1982], a process subsequently suggested by *Schulte and Arnold* [1992] to explain these detections. Massive negatively charged dust particles can be formed by the nucleation of water group clusters onto meteoric smoke particles, which consequently form small ice structures. The relatively faster motion of electrons relative to that of ions results in electrons attaching onto these particles. This has been identified as resulting in large electron depletions of over an order of magnitude [e.g. *Friedrich and Rapp*, 2009].

Negative ion species have also been shown to vary over diurnal cycles [*Fritzenwallner and Kopp*, 1998] and to increase abundances by several orders of magnitude during Solar Energetic Proton events [*Verronen et al.*, 2005]. Radar measurements have also revealed the sporadic formation of large negative ion zones at larger altitudes near 95 km [*Ganguly*, 1984], which illustrates the dynamic nature of the negative ion chemistry. The relevance to human activity is also apparent as negative ions have been shown to act to modulate production of the protective ozone layer [*Osepian et al.*, 2009] and ionospheric electron densities strongly influence the propagation of radio signals.

Negative ions in the Earth's atmosphere were known to exist before any other in atmospheric

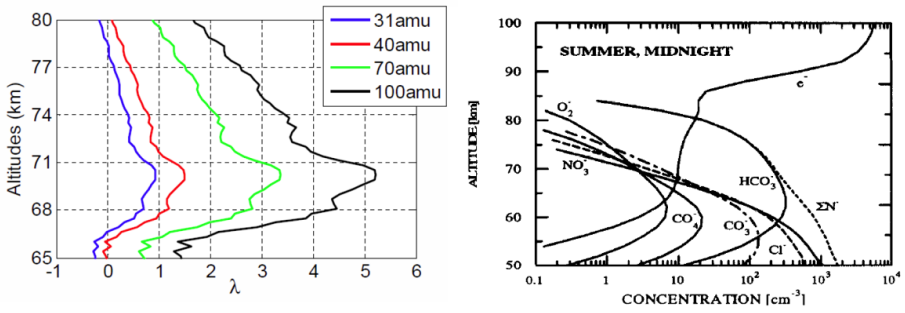

Figure 2.5: The left panel shows radar measurement of the negative ion abundances using various different assumed mean masses as a function of wavelength from *Gong et al.* [2017] and the right hand panel shows the modelled abundances according to *Fritzenwallner and Kopp* [1998]

and space environments [e.g. *Appleton et al.*, 1933], and, in tandem with negative ions in laboratory applications, galvanised much of the earlier theoretical work on the topic [*Massey*, 1976]. Many open questions remain, however, regarding the spatial and temporal distributions of these species and a global model of their evolution with respect to latitude and local time, has yet to be reported. The role of massive negatively charged particles of several hundred atomic mass units also remains to be constrained with regards to negatively charged cluster ions and meteoritic ablation.

2.5 Comets

2.5.0.1 1P/Halley

The Giotto spacecraft opened the inner coma of Comet Halley to detailed measurements and analysis. During the encounter, whilst just 600 km from the cometary nucleus, the electron instrument surprisingly detected negatively charged ions arriving from the spacecraft ram vector [*Chaizy et al.*, 1991]. The relatively fast motion of the spacecraft, with respect to the slow-moving negative ions, resulted in these species overcoming the electrostatic forces of the instrument, nominally set to accept only electrons. These detections are shown in Figure 2.6 from which these detections were constrained into three broad mass peaks of 7-19 u/q, 22-65 u/q and 85-110 u/q.

These detections were initially attributed to O^-, OH^-, C^-, CH^-, CN^- and more complex negatively charged molecular species deriving from CHO. Further chemical modelling of negative ion chemistry at 1P/Halley by *Cordiner and Charnley* [2014] built upon the advances made in understanding of interstellar anion chemistry and highlighted the likely presence of C_nH^- where n=4,6,8, and CN^-. An interesting outcome of this study was the result that the highest mass

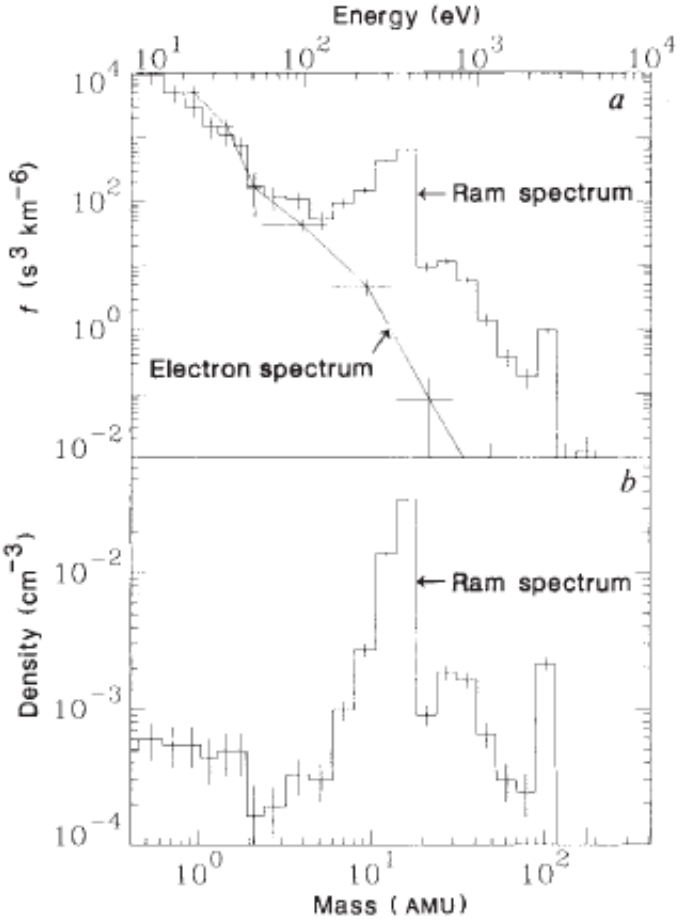

Figure 2.6: Negative ion mass spectra and densities measured by Giotto at Comet 1P/Halley [*Chaizy et al.*, 1991].

considered, C_8H^-, could only be produced in abundances high enough to match the observations if a source of large carbon chains bearing molecules from the nucleus was considered [*Cordiner and Charnley*, 2014]. Constraining the stoichiometric composition of comets, or indeed even families of different comets, is an active area of research [e.g. *Mumma and Charnley*, 2011], and results from this will surely guide studies of what negative ions might be produced.

The presence of molecular anions at 1P/Halley provided the first indication that negative ions might play a significant role in other solar system plasma with reduced photodetachment rates.

2.5.0.2 67P/Churymov-Gerasimenko

The recent Rosetta mission to Comet 67P/Churymov-Gerasimenko has provided valuable insight into the composition and evolution of cometary bodies close to the Sun. When close to the comet, Rosetta detected the presence of the hydrogen anion, H^-, within the solar wind [*Burch et al.*, 2015]. The low velocities of the spacecraft relative to the nucleus, did however, pre-

clude the detection of more complex molecular negative ions that via the method used at Comet 1P/Hally. These negative ions were, as at Comet Halley, made using an electron instrument and were observed as a distinct plasma population at $\sim$10% of the solar wind proton density, and with $\sim$90% of the energy. The production mechanisms were explained by a double charge exchange reaction sequence resulting from the interaction of solar wind protons and cometary neutrals and ions. In the first instance, a solar wind proton interacts with a cometary neutral such as H_2O or CO_2, which are represented as M in the following reactions. This process initiates as,

$$H^+ + M \rightarrow H_{fast} + M^+. \tag{2.4}$$

The resulting fast neutral can then interact with cometary ions to produce a negative ion via,

$$H^+ + M \rightarrow H_{fast} + M^+. \tag{2.5}$$

The discovery of these negative ions were the first observations of H^- in the solar wind. The detections were reported between 3.4 and 2.5 A.U. from the Sun and it therefore remains unknown how this phenomenon develops throughout the comets orbit.

The implications of H^- for cometary chemistry have also not been addressed although *Burch et al.* [2015] noted these could be relatively minor due to the energy of these species being sufficiently high to allow them to escape the inner coma relatively quickly.

2.6 Europa

The Galilean moon Europa is bombarded by the sub-Alfvénic plasma of the Jovian magnetodisc and radiation belts, which results in the generation of a sputter-induced oxygen-based exosphere. On two flybys through the moon's plasma wake, the Galileo spacecraft's magnetometer observed a mix of left and right-handed ion cyclotron wave power at the chlorine gyrofrequency [*Volwerk et al.*, 2001; *Kivelson et al.*, 2009], a phenomena absent at the gyrofrequencies of other trace species picked up from the moon, such as Sodium and Potassium. This phenomenon was consequently attributed to the pickup of both positively and negatively charged Chlorine ions. The inference is also compatible with the stable configuration of the Chlorine anion, the additional electron filling the halogen's outer electron shell.

This phenomenon is possible as positively charged pickup ions gyrate in a left-hand sense

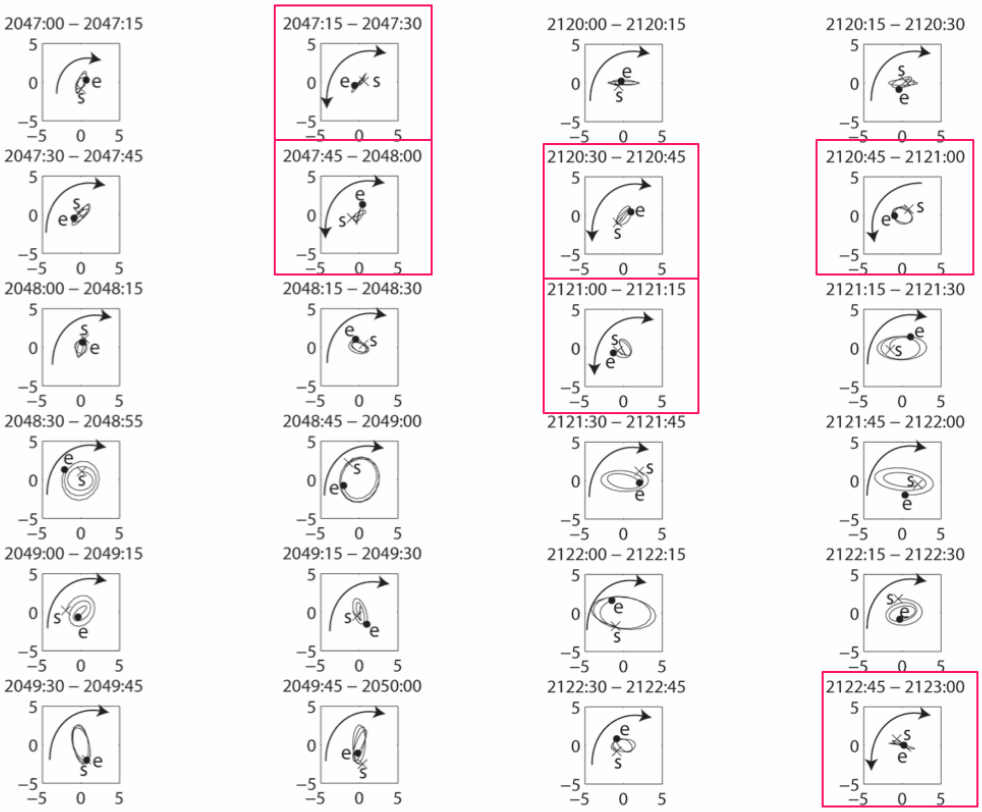

Figure 2.7: Magnetic field hodograms showing the wave polarisations at the Chlorine gyrogrequency during Galileo's E11 and E15 encounter through Europa's wake as shown in [*Kivelson et al.*, 2009].

around the magnetic field and, when the distributions are unstable to wave growth as anticipated for pickup ions, this causes the resultant waves to also possess a left-hand polarisation. Negatively charged pickup ions conversely gyrate in a right-hand sense around the magnetic field and resultant waves would therefore also possess a right-hand polarisation. ICWs are by definition gyroresonant and the occurrence of brief periods of right-hand polarisations, as shown in Figure 2.7, at the Chlorine ion gyrofrequency, suggests a non-negligible contribution from Cl^- to the Chlorine pickup process.

Source densities were not calculated in this study as it was unclear whether the the instability had saturated or was still growing [*Volwerk et al.*, 2001]. Io provides a local Chlorine source in the Jovian environment [*Küppers and Schneider*, 2000; *Feldman et al.*, 2001], and Chlorine has also been hypothesised to be present in Europa's sub-surface ocean in the form of NaCl, which arises through the extended contact with a rocky ocean bed, as occurred in the Earth's oceans. *Hand and Carlson* [2015] suggest that Chlorine could be abundant on the moon's surface due to upwelling

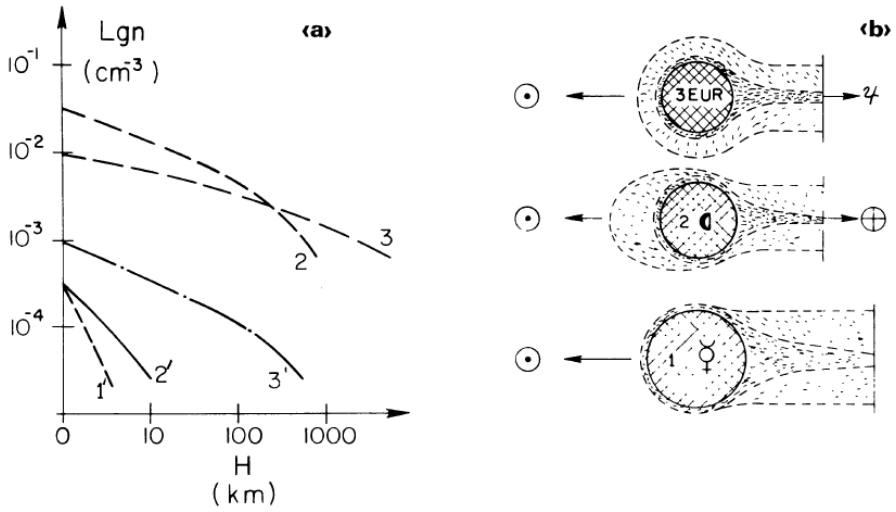

Figure 2.8: Calculated negative ion densities and qualitative diagram of the ionospheres of (1) the Moon, (2) Mercury and (3) Europa. The solid and dashed lines correspond the hydrogen and non-hydrogen components [*Wekhof*, 1981].

of ocean material through cracks in the surface ice.

Negative ion ionospheres have been predicted around the surface of solar system bodies with thin atmospheres such as the moon, Europa and also Mercury [*Wekhof*, 1981]. Figure 2.8 shows a depiction of this at these three environments where the negative ions reach densities of a few percent of the electron density as a result of sputtering processes. Chlorine was not considered in this analysis however which concentrated mainly on H^- and some heavier species.

This possible detections of negative ions at Europa shows negative ions might result in the generation of unique plasma instabilities, different to those previously observed in space plasmas. The densities of Chlorine ions at Europa might also elucidate whether Europa is a net source of Chlorine, or whether it is derived from Iogenic populations implanted in Europa's surface.

2.7 Titan's ionosphere

The detections of heavy negative ions in Titan's ionosphere by Cassini at altitudes 870-950 km, completely reshaped our understanding of the moon's upper atmosphere. Prior to this, negative ion species had only been considered to exist in the cosmic ray induced ionised layer below 200 km, during the night [*Hunten et al.*, 1984; *Borucki et al.*, 2006]. At these lower altitudes, the attachment of electrons onto molecules such as H, CH_3 and C_3H_2 as well as onto PAH's were considered due to the large concentrations of electrons that could exist compared with other substantial atmospheres, such as those of Venus and the Earth.

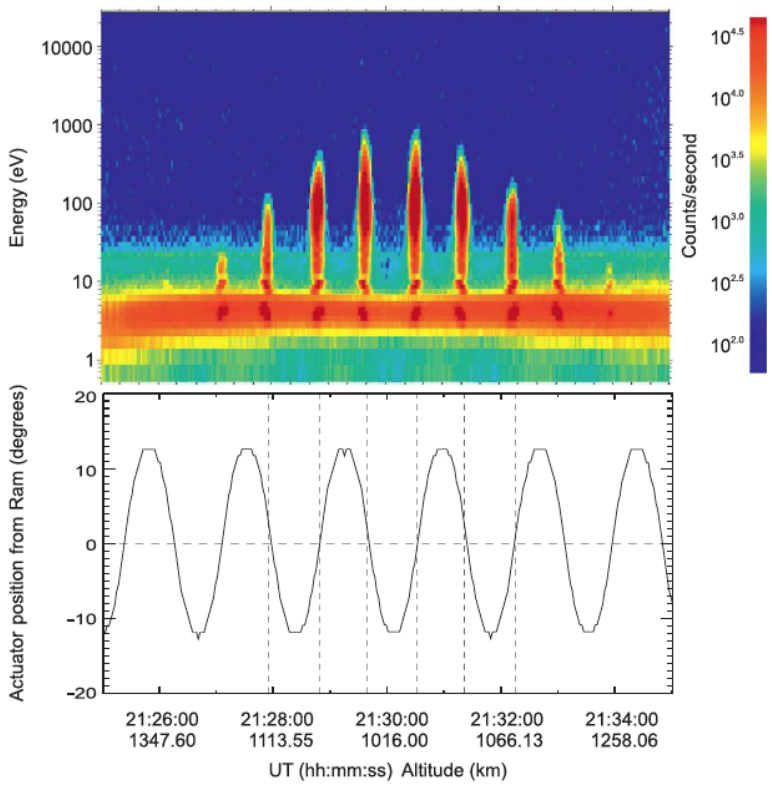

Figure 2.9: Negative ion mass spectra during the T40 encounter showing how the negative ion signatures only appear when CAPS is pointing in the Ram direction [*Vuitton et al.*, 2009a].

The negative ions observed in Titan's ionosphere were first detected by the Cassini's electron spectrometer [*Coates et al.*, 2007a] and were also observed by the langmuir probe [*Ågren et al.*, 2012], as Cassini sampled Titan's atmosphere in-situ. Here, the electron spectrometer was able to observe a mass spectrum through using the ram velocity of the spacecraft, as Giotto did at Comet Halley. The relative energy between the spacecraft and the cold plasma enabled the negative ions to overcome the electrostatic passband of the instrument so that the energy-per-charge spectrum can be converted into a mass-per-charge spectrum. The electron spectrometer was located on an actuator, which scanned through the spacecraft ram direction and the negative ions were consequently evident as distinct spikes in the velocity distributions as the instrument scanned back and forth across the ram direction, see Figure 2.9.

This spectrum was identified as containing negatively charged ions and aerosol precursors extending from 12 to 13,800 u/q [*Coates et al.*, 2007a, 2009]. The energy resolution of the instrument however did not allow unambiguous identifications and the species were grouped into mass ranges of 12-30, 30-55, 55-90, 90-130, 130-190, 190-625, and >625 u/q, with the highest masses

observed at the lowest altitudes [*Coates et al.*, 2009; *Wellbrock et al.*, 2013]. These large negatively charged molecules are thought to be the precursors to the haze observed at lower altitudes [*Waite et al.*, 2007], and to drift downwards, possibly even playing a role in surface processes. The Langmuir Probe is able to resolve the current balance onto its surfaces [*Gurnett et al.*, 2004; *Shebanits et al.*, 2016] and reported that the negative ions carried a greater amount of the negative charge than electrons at the lowest altitudes and resulted in an ion-ion dusty plasma [*Ågren et al.*, 2012; *Shebanits et al.*, 2013].

Cassini observed negative ion data on all encounters where pointing conditions were favourable. This resulted in a dataset spanning 35 flybys. The negative ions were found to display a latitude dependence with higher masses preferentially existing at lower latitudes and a weak dependence on Solar Zenith Angle was also reported [*Coates et al.*, 2009]. Density estimations showed the negative ions as existing with densities as high as 200 cm^{-3} and notably showed how the ratio of large to small negative ions appeared greater than one.

As with regarding interstellar environments, the lack of reaction rates at these low temperatures ($\sim$150 k), has severely hindered chemical modelling efforts. To date, only two studies have included negative ions and these only included species with mass $\leq$75 u [*Vuitton et al.*, 2009a; *Dobrijevic et al.*, 2016]. These studies highlighted the presence of the carbon chain anions, C_nN^- and $C_{n+1}H^-$, where n=1,3,5. There exists however a significant discrepancy between modelled and observed densities, see Figure 2.11, with the modelled abundances appearing up to two orders of magnitude lower than those reported by *Wellbrock et al.* [2013]. Aerosol charging models have provided theories that explain the high mass negative ions using aerosol charging microphysics [*Michael et al.*, 2011; *Lavvas et al.*, 2013; *Lindgren et al.*, 2017]. The results of *Lavvas et al.* [2013] are displayed in Figure 2.10, which shows how the positively and negatively charged species distributions can be reasonably explained by such calculations, despite not using specific chemistry.

While some explanation has been provided for the lower mass species, the route from small to large molecules in Titan's ionosphere is still unknown. Studies have highlighted the role of ion-molecule growth processes in producing molecules greater than 100 u [*Westlake et al.*, 2014], and building processes via Olah's carbonium chemistry has also been proposed. In the latter study the negative ions have been identified as possible carbanions formed from carbocations. $C_{13}H_9^-$ is illustrated by *Ali et al.* [2015] as such an example.

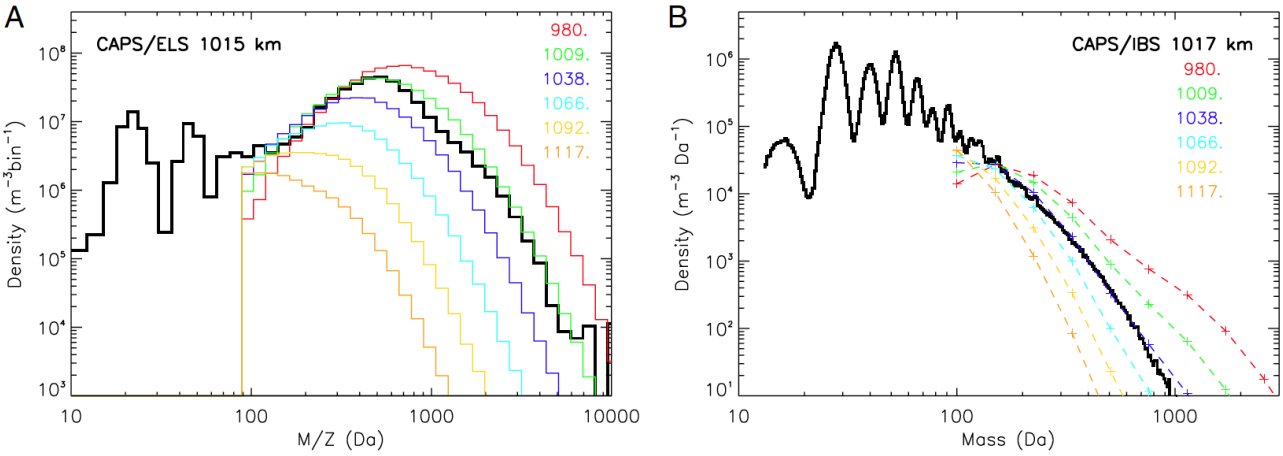

Figure 2.10: CAPS positive and negative ion mass spectra (black) and the aerosol mass distribution from the model of *Lavvas et al.* [2013] (orange-red), which shows that stochastic charging processes can explain the size distributions of the larger species.

The negative ions at Titan provided a paradigm shift regarding the presence of large organic molecules at significant altitudes within a dense atmosphere. An adequate explanation of the production routes for the low mass negative ions is now required as the models produce significantly less than those observed [*Wellbrock et al.*, 2013; *Vuitton et al.*, 2009a]. Significant uncertainties exist however regarding the chemical models and uncertainties as well as in the observed abundances, which hinders further quantitative comparisons. While the trend of increasing in mass with decreasing altitude points to building processes it is also quite plausible that the larger organics such as PAHs and cyannopolyynes could be breaking down at the top of the atmosphere and their constituents providing the source for negative ion production. The intermediary part of the ELS spectrum also remains unconstrained, that is the range above the maximum mass of 75 u considered by the anion chemistry modelling studies and below the several hundred amu where aerosol charging physics start to dominate [*Lavvas et al.*, 2013], see Figure 2.10. The composition of the larger molecules are unknown and it is also unknown whether the larger species are formed predominantly from chains, rings or even fullerenes [*Sittler et al.*, 2009].

2.8 Enceladus plumes

The plumes of Enceladus constitute the primary mass loading source within Saturn's inner magnetosphere emitting between 20-200 kg/s of water-based material, which forms Saturn's Extended Neutral Cloud (ENC) extending from 2-10 R_s [*Dougherty et al.*, 2006; *Jurac and Richardson*, 2005] . When passing through these plumes, Cassini's electron instrument observed

negatively charged ions and ice-grains, in an analogous manner to at Titan or 1P/Halley [*Coates et al.*, 2010; *Jones et al.*, 2009]. These charged ions and molecules were associated with the plume and thus forming a part of the moon's plume-derived atmosphere. The detections are displayed in Figure 2.12.

The negative ions were observed to peak at multiples of the mass of water-group ions, 16-18 u, indicating the presence of O^-, OH^-, H_2O^- and higher order negatively charged water cluster ions and possibly also more complex organics [*Coates et al.*, 2010]. The negative ions were identified as being formed through dissociative electron attachment and to possess short lifetimes of $\sim$6s due to high photodetachment rates [*Coates et al.*, 2010]. They were observed in regions of stagnated flow and, given these short lifetimes, it does not appear likely that they would reach beyond the vicinity of the plumes.

The negatively charged nanograins were observed at masses from 1000 u up to the top of the ELS range of 17,600 u/q, the trend of increasing density with increasing mass implying even larger species were also present above this. It was initially suggested that these became charged via tribo-electric interaction with the wall of the plume vents [*Jones et al.*, 2009]. Further analysis however revealed that incoming fluxes of magnetospheric electrons were also able to explain their charge state *Hill et al.* [2012]. Charging studies have also highlighted how these nano-sized ice grains represented a previously unseen mass distribution spanning the range between the gas phase material and the larger grains observed by Cassini's Cosmic Dust Analyser [*Spahn et al.*, 2006; *Dong et al.*, 2015].

The detections of negative ions and negatively charged ice grains at Enceladus revealed a new component of the Enceladus plume and showed negatively charged ions and ice grains to play a significant role in this environment.

2.9 Rhea

Saturn's icy moon Rhea hosts a sputter induced atmosphere composed of O_2 and CO_2. During a targeted encounter with the moon, Cassini's electron instrument detected negatively charged pickup ions behind the moon, in agreement with the anticipated cycloidal trajectory of ion deriving from the moons atmosphere, see Figure 2.13 [*Teolis et al.*, 2010]. The discovery of these negatively charged pickup ion populations contributed to the discovery of the moons tenuous exosphere and highlighted the pickup of negative ions as a possibly significant atmospheric loss

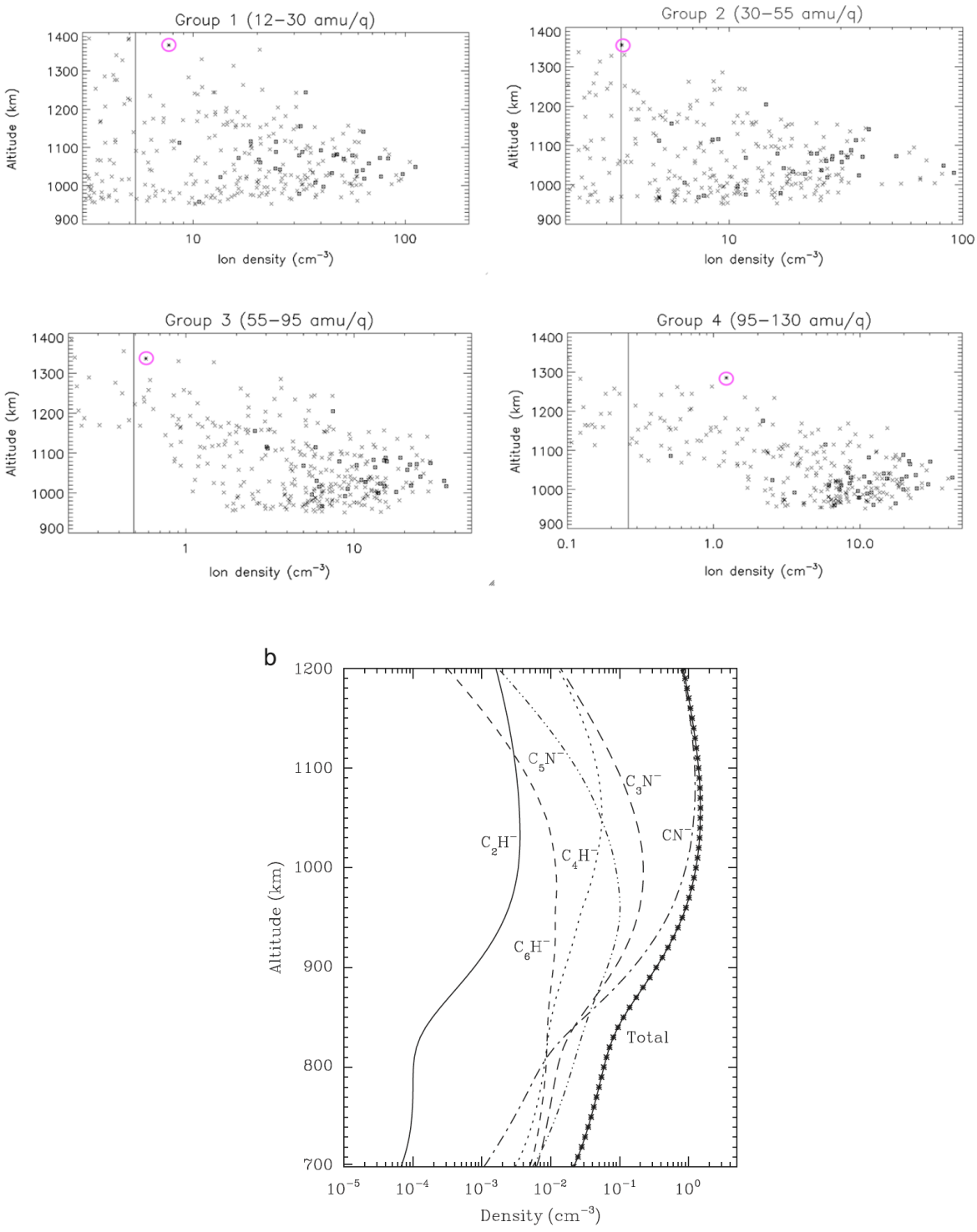

Figure 2.11: Altitude dependence of the negative ions in Titan's ionosphere from *Wellbrock et al.* [2013] and the modelled results of *Vuitton et al.* [2009a], which are significantly different to one another.

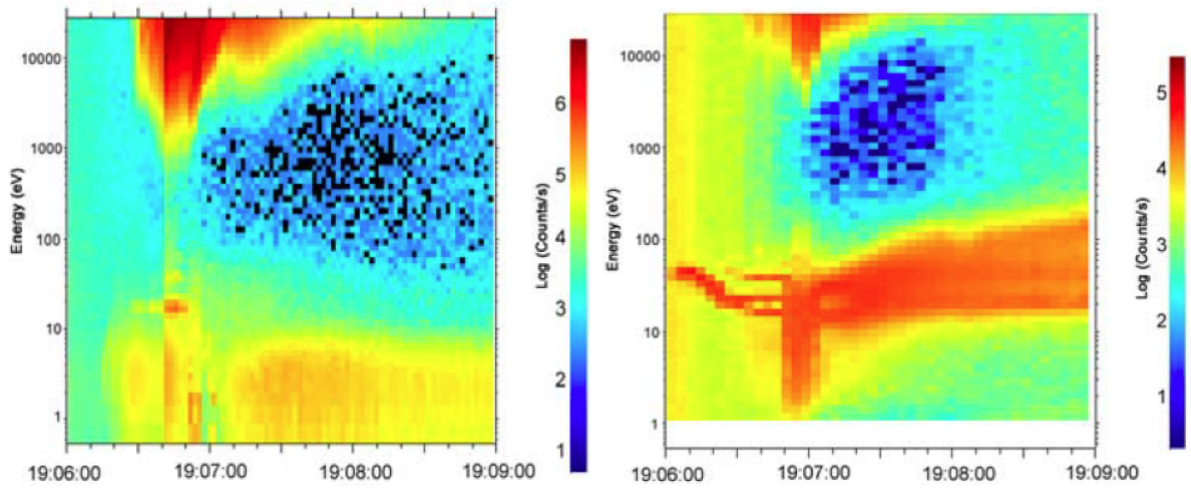

Figure 2.12: Cassini observations of negatively charged ions and nanograins (left) and positively charged ions and nanograins (right) in the Enceladus plumes [*Jones et al.*, 2009].

mechanism.

These detections were initially identified as O^- produced through dissociative reactions between the incident plasma and atmospheric neutrals. Further more distant encounters with the moon failed to detect these species, possibly indicating high loss rates in Saturn's magnetosphere.

Further analysis by *Teolis and Waite* [2016] however highlighted the inefficiency of gas-phase electron attachment reactions [*Itikawa*, 2009] and suggested surface reactions involving O_2 adsorbed on the night side was a more likely explanation.

2.10 Key Themes

This chapter demonstrates how the recent spate of discoveries of negatively charged ions in the outer solar system has heralded a new frontier for their study. The decreased loss mechanisms at greater heliocentric distances also points to an even greater role played by these species beyond Saturn where the outer-most discoveries have been made. Several key themes emerge when analysing the detections of negative ions in atmospheric and space environments.

The first theme is that of the role played by negatively charged hydrogen. As the most abundant element in the Universe, this is perhaps not surprising and the hydrogen anion has been found to play a role in hydrogen rich environments from the cold interstellar medium to the Sun's photosphere to at comets immersed within the solar wind.

The second theme to emerge is that of organic chemistry. Complex organic chemistry in the dense interstellar medium involves anions playing an important role and the discovery of negative

ions in Titan's atmosphere also showed organic chemistry here to be sensitive to abundance of negative ions. The negative ions observed at Comet 1P/Halley are also likely organic in nature although have not been definitively identified. The abundance of organic molecules, termed tholins by *Sagan and Khare* [1979], in the outer solar system, such as at Pluto and throughout the Kuiper Belt, also provide further environments ripe for detecting negative ions.

The third theme involves the role of negatively charged oxygen. These play a significant role in initiating negative ion chemistry in the Earth's ionosphere and negatively charged water group ions have been identified within the Enceladus plumes. Tentative detections of negatively charged water group ions have has also been made near Saturn's main rings [*Jones and Coates*, 2014] and could form significant magnetospheric populations in Saturn's shadow.

Beyond these, the final theme is that of the halogens, which possess the highest electron affinity of all elements in the periodic table. Chlorine and Bromine compounds have been discovered to exist within the Earth's atmosphere and Chlorine inferred as possibly present at Europa.

It is interesting to note that all of the detections in the Outer Solar System were made by instruments not specifically designed and calibrated for this purpose. In most instances the detections were made using an electron spectrometer with the data reformulated to yield mass spectroscopic measurements. The presence of negative ions at Europa was inferred using a magnetometer.

2.11 Conclusions

The various detections of negative ions in space and atmospheric plasmas demonstrate how negative ions often form a fundamental part of the medium which they populate. Not considering them could therefore lead to significant misunderstandings of the physical processes at hand.

Reviewing the literature pertaining to negative ion detections thus provides context for future exploratory endeavours. Here, the implementation of instruments designed to detect negative ions can be considered, or existing instruments operated in manner facilitating their detection. This literature is also important for modelling efforts, which aim to describe space and atmospheric environments and in these the inclusion of all plasma components may be necessary to accurate understand the physics and to formulate fundamental theory.

The previous work has been unique and provided excellent targeted studies of individual cases of negative ions. These studies have however been isolated and staggered over time and

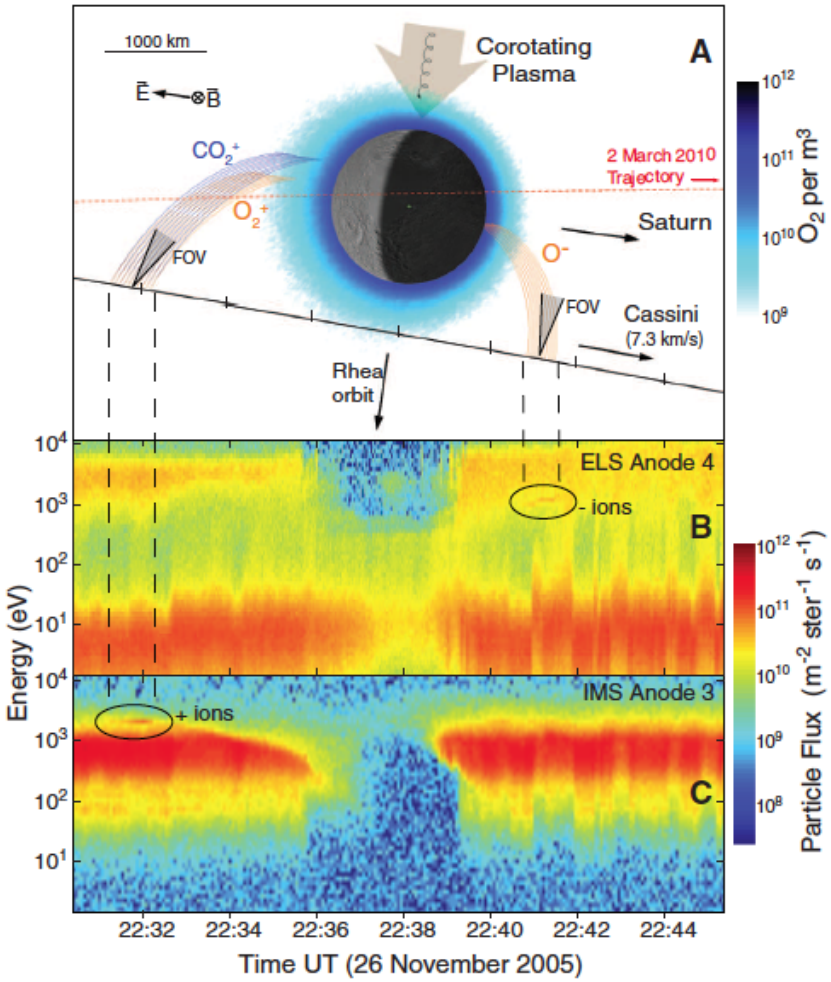

Figure 2.13: The detection of positive and negative pickup ions during Cassini's passage behind Rhea. The top panel shows the trajectories of pickup ions picked up from the moon as *Teolis et al.* [2010].

indeed are spread across several different subject areas. What is therefore missing is a comprehensive review, which ties these pieces of knowledge together into a coherent tapestry. This chapter aims to provide this by highlighting the key themes common across vastly different environment and which are relevant when considering negative ions in further environments such as many within the outer solar system.

Chapter 3

Methods & Techniques

The research described in this thesis exploits Cassini spacecraft data and employs numerical plasma simulations. This chapter describes the specific instruments from which data is derived and the simulation technique.

3.1 The Cassini-Huygens mission

The Cassini-Huygens mission was a collaborative endeavour of the NASA, ESA and ASI space agencies. The spacecraft was launched on a Titan IVB/Centaur rocket on 15 October 1997 and used gravitational assists from Venus (26 April 1998 and 24 June 1999), Earth (18 August 1999) and Jupiter (30 December 2000) to slingshot itself towards Saturn where orbit insertion occurred on 1 July 2004.

The Cassini orbiter was initially scheduled for a 4 year Prime Mission, which was supplemented by the two year Cassini Equinox Mission, the seven year Cassini Solstice Mission, and the 4 month Grand Finale Mission, which ended up with Cassini burning up in Saturn's atmosphere on 15 September 2017.

Cassini carried an extensive range of instruments, which included twelve scientific payloads and the Huygens probe, which landed on Titan on 14 January 2005. The science instruments are shown in Figure 3.1, designed to explore and characterise Saturn's surface and interior, the magnetosphere and its interaction with the Solar Wind, the many icy satellites, which form Saturn's rings and moons, and the large Earth-like moon Titan. As an exploratory endeavour the mission also had significant scope for change, a capability exemplified by the discovery of the Enceladus plumes and sub-surface ocean, and the subsequent targeted encounters to directly sample the plume material

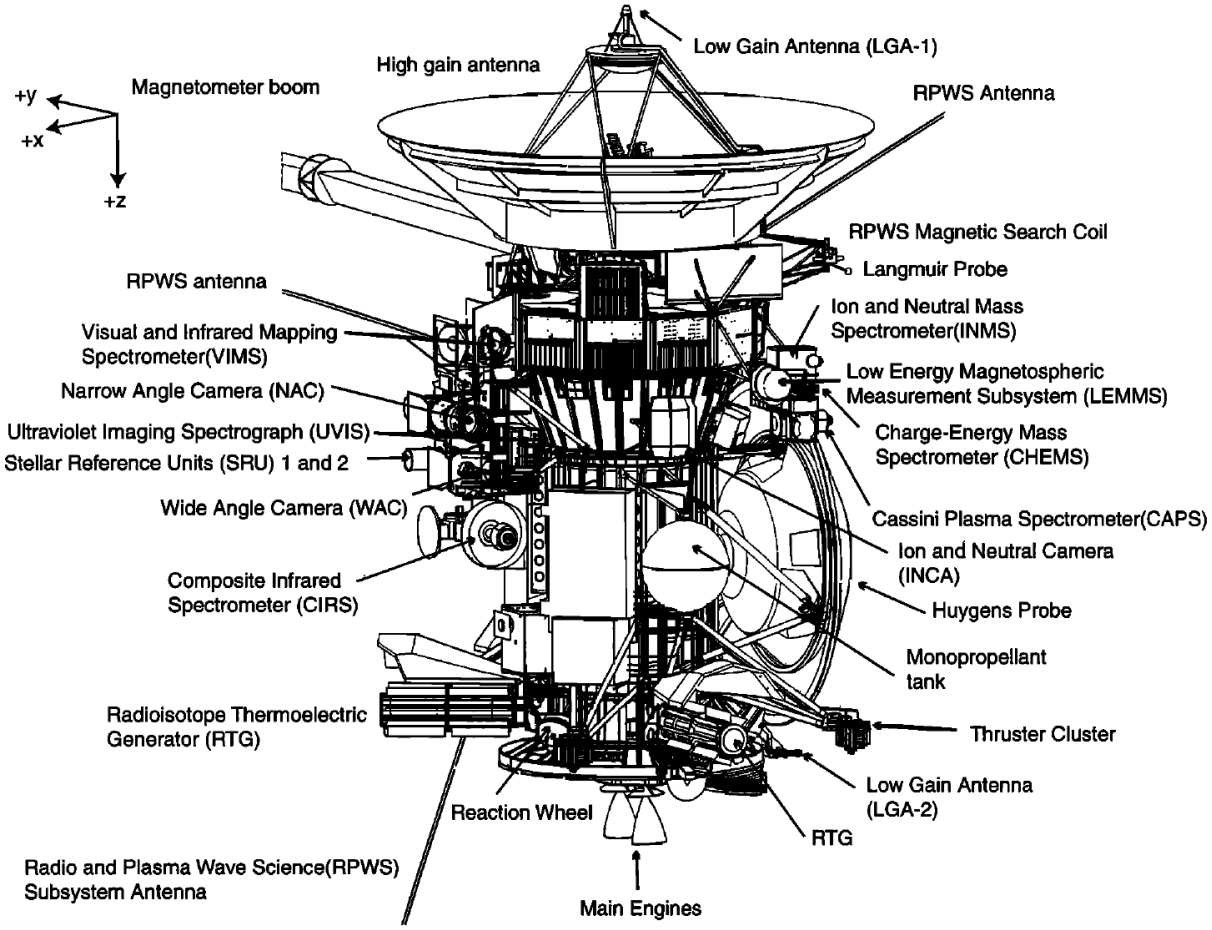

Figure 3.1: Cassini spacecraft schematic displaying science payloads showing and engineering subsystems [*Burton et al.*, 2001].

3.2 Cassini Plasma Spectrometer

The Cassini Plasma Spectrometer (CAPS) consisted of a suite of three instruments [*Young et al.*, 2004]. These included the Electron Spectrometer (ELS) to measure low energy electrons, the Ion Beam Spectrometer (IBS) to measure ion beams at high energy and angular resolution, and the Ion Mass Spectrometer (IMS) to measure ions at a lower angular resolution but with mass resolving capabilities. These all utilised electrostatic analysers (ESA's) to energy select incident charged particles and the IMS contained an additional Time-Of-Flight (TOF) system.

Cassini was a three axis stabilised spacecraft and CAPS was located on the fields and particles pallet and had its own actuator, which moved through 208° to increase its FOV.

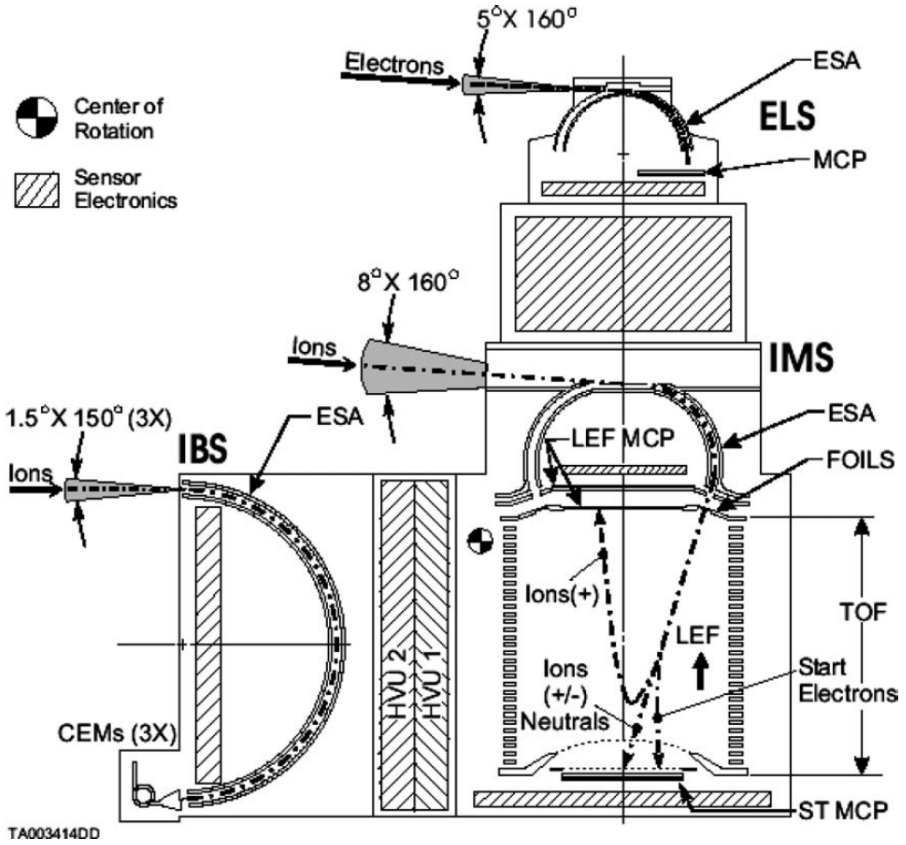

Figure 3.2: CAPS cross section in the XY azimuthal plane of the spacecraft (see Figure 4). Cross-hatched areas denote electronic also shown [*Young et al.*, 2004].

3.2.1 CAPS-Electron Spectrometer

The CAPS-ELS is a hemispherical top-hat analyser based on the design initially described by *Carlson et al.* [1982], similar to the Cluster Plasma Electron and Current Experiment(PEACE) [*Johnstone et al.*, 1997] but with a more compact mechanical arrangement. It was designed to measure low energy electrons in the energy range of 0.55-26,600 eV with a 160° field of view (FOV) in elevation over 8 anodes and a 5° FOV in azimuth.

Th actuator upon which CAPS is located, swept through its 208° at a rate of $1^\circ/s$, although the orientation could be held at specific angular settings for targeting specific plasma populations. The energy range is divided into 63 quasi-logarithmically spaced energy bins, which, by default, the instrument steps down through in 2 seconds. 25% of the time spent in each bin and the 63rd bin is dead time to allow the sweep high voltage to settle. The instrument is also capable of scanning through a selected energy range twice in 2 seconds for a higher time resolution, and can also be held at a continuous energy level for in-flight calibration purposes. From optical and physical

calibration tests the instrument has been determined to have an energy resolution of $\sim$16.7% at Full-Width-Half-Maximum (FWHM). Incident particles pass through a grounded baffle structure and are then bent by an electrostatic analyser to energy select particles of interest.

The particles then pass through a biased grid, which acts to reject secondary electrons, such as from incident particles impacting the walls inside the ELS, and strike onto the first Microchannel Plate (MCP). The incident particle is amplified by 10^6, according to the MCP gain function, and a secondary MCP amplifies this signal once more before the signal is collected by 8 anodes. The MCPs are arranged in a chevron configuration to reduce ion feedback and with a spacer to increase lifetime. Beyond the grounded baffles and the biased grid, as with PEACE, a number of additional improvements have been made, in order to reduce the susceptibility to spacecraft photoelectrons, to increase relative accuracies and to account for non-concentricity of the hemispheres.

3.2.2 Deriving plasma parameters for the CAPS-ELS

The ELS has demonstrated that it is capable of detecting negatively charged ions as well as electrons [*Coates et al.*, 2007a; *Teolis et al.*, 2010; *Coates et al.*, 2010] and, due to the varioius detections of negative ions made by this instrument, which this thesis focuses on, the various methods of deriving plasma parameters from are now described in some depth.

The ELS measures incident particles as counts, which must be converted into relevant physical parameters describing the bulk plasma properties. As Cassini is a three axis stabilised spacecraft, the plasma instruments have limited FOVs, which complicates the integration of the results over the full 4π space. When retrieving bulk plasma properties parameters, such as Phase Space Density (PSD) and Differential Energy Flux (DEF), are commonly used. Phase Space Density (PSD) describes the bulk properties of a plasma within a six dimensional space consisting for three dimensions in configuration space and three in velocity space. The PSD can be obtained from instrument counts via,

$$PSD = \frac{2R_c}{t_a \mathbf{v}_c^4 G}, \tag{3.1}$$

where R_c is the instrument count rate, t_a is the accumulation time, v_c the incident velocity, and Geometric Factor is of the form,

$$G = \int\int\int T(\mathbf{v}, \theta, \phi, \varepsilon), \tag{3.2}$$

where T is the transmission, θ and ϕ are the polar and azimuthal angles respectively, and ε the MCP detection efficiency [*Rymer*, 2004; *Lewis et al.*, 2008]. The PSD representation of bulk space plasma properties, in accordance with Louiville's theorem, shows that the phase space distribution function is constant through time within the system. Corrections to the data can thus be applied such as altering the energy or removing effects associated with spacecraft charging or contamination by spacecraft photoelectrons [*Lewis et al.*, 2008]. The Differential Energy Flux (DEF) defines the number of particles at the measured energy E, within ΔE, passing through area A, and solid angle subtended by Ω. This can be related to the PSD via,

$$N = \frac{R_c}{A\Omega\Delta E} = PSD\frac{2E}{m^2}, \tag{3.3}$$

where m, is the measured particles mass derived from the energy E. Two distinct methods of extracting plasma parameters from the CAPS-ELS count rate have been used. The first was developed by *Rymer* [2004] and is referred to as a one dimensional method, useful as a fast and simple method for extracting parameters. The second method is more accurate and is described as the three dimensional approach where plasma parameters are obtained by taking moments of the plasma momentum equation, as is described in many textbooks [e.g. *Baumjohann and Treumann*, 1996].

3.2.2.1 1-D method

In this method, the density and temperature of the plasma is calculated by approximating the distribution function as a Maxwellian of the form,

$$f = n(\frac{m}{2\pi kT})^{\frac{3}{2}} exp(-\frac{E}{kT}), \tag{3.4}$$

where T is the plasma temperature and n the number density. Combining this with Equation 3.3 and then differentiating with respect to the count rate leaves,

$$\frac{dR_c}{dE} = exp\frac{-E}{kT}(2CE - \frac{CE^2}{kT}), \tag{3.5}$$

where,

$$C = \frac{2nG}{\sqrt{m}}(\frac{1}{2\pi kT}). \tag{3.6}$$

For the maximum count rate, Equation 3.5 can be set to zero and expressions for the plasma temperature can be calculated as,

$$T = \frac{E_{peak}}{k(2+\frac{dln(G)}{dln(E)})} \simeq \frac{E_{peak}}{2kT}, \tag{3.7}$$

and the density as,

$$T = \frac{\pi^{\frac{3}{2}}}{2^{\frac{3}{2}}G} R_c \sqrt{\frac{m}{kT}} exp(2). \tag{3.8}$$

3.2.2.2 3-D Method

In this method the plasma number density, the bulk flow velocity v_b, and the stress tensor, which in the plasma rest frame is equal to the pressure tensor P, can be obtained from the first three moments of the particle distribution function,

$$M_r(x,t) = \int \mathbf{v}^r f(\mathbf{v},x,t) d^3\mathbf{v}. \tag{3.9}$$

The zeroth moment of this distribution function is density,

$$n = \int f(\mathbf{v}) d^3\mathbf{v}, \tag{3.10}$$

the first moment is bulk velocity,

$$v_b = \int \mathbf{v} f(\mathbf{v}) d^3\mathbf{v}, \tag{3.11}$$

and the second moment pressure,

$$P = m \int (\mathbf{v}-\mathbf{v}_b) \cdot (\mathbf{v}-\mathbf{v}_b) f(\mathbf{v}) d^3\mathbf{v}. \tag{3.12}$$

As no analytical solution exists due to the initial distribution function, the off-trace elements of the pressure tensor can be assumed as negligible and as introducing inaccuracies due to the limited CAPS FOV. The above equations are summed over the finite energy measurements of the instrument and expressed using spherical polar coordinates as scalar quantities. The number density can be expressed as

$$n = \frac{4\pi}{3} \sum_{i=1}^{i=63} f(\mathbf{v}_{i,m})(\mathbf{v}_i^3 - \mathbf{v}_{i-1}^3), \tag{3.13}$$

and the temperature as,

$$T = \frac{4\pi m}{15kn} \sum_{i=1}^{i=63} f(\mathbf{v}_{i,m})(\mathbf{v}_i^5 - v_{i-1}^5). \tag{3.14}$$

3.2.2.3 Current approximation

In the ionosphere of Titan, negative ions were detected in the spacecraft ram direction where the spacecraft velocity provided the energy for these relatively slow moving species to overcome the instruments ELS [*Coates et al.*, 2007a]. They could be distinguished from electrons due to electrons being highly supersonic and therefore registering across anodes not aligned with the spacecraft velocity vector whereas the negative ions consistently measured as arriving from only this direction. In order to derive their properties, the negative ions can be approximated by a current arriving from the ram vector, as carried out in previous analyses when the flow speed is significantly greater than the thermal speed [*Waite et al.*, 2005]. Titan's ionosphere is assumed as cold and to be in thermodynamic equilibrium and the thermal energy of the ions is therefore negligible compared with the kinetic energy. Studies of ion temperatures in Titan's ionosphere indeed show ion temperatures to be small when compared with the ELS energy range of 0.58-26,600 eV [*Crary et al.*, 2009]. The ions are therefore assumed stationary and the energy bin at which they are measured equated to the relative kinetic energy between the ions and Cassini, and thus used to calculate the ions mass as:

$$m_i = \frac{2E}{Z_i \mathbf{v}_{sc}^2} \tag{3.15}$$

where v_{sc} is the spacecraft ram velocity, E the ion kinetic energy in the spacecraft frame, and Z_i is the assumed charge on the ion [*Coates et al.*, 2007a]. This relation indicates that the ELS is capable of measuring a mass range corresponding to its energy range, the exact bounds determined by the spacecraft ram velocity. These assumptions also allows the ion counts to be differentiated from the electron counts. By averaging the counts across the anodes, which are not oriented in the ram direction and have a good FOV, an average value for the isotropically observed electrons can be found and removed, thus leaving behind counts due to negative ions subject to an error of

the standard deviation of the electron counts across the different anodes. In previous analyses the response of the different anodes has also been normalised to one another [*Wellbrock*, 2012]. The number density of the measured species can then be calculated by,

$$n = \frac{R_c}{\varepsilon A \mathbf{v}_{sc}}, \tag{3.16}$$

where ε is the MCP detection efficiency and A is the effective area of acceptance.

3.2.3 MCP response to negative ions

The MCP response to the negative ion species in Titan's ionosphere has been identified as a significant limitation in previous analyses [*Coates et al.*, 2007a; *Wellbrock et al.*, 2013]. In this section the relevant literature on MCP efficiencies for both positive and negatively charged ions are reviewed.

The literature relating to Microchannel Plate efficiencies has roots within the field of ion-surface interactions and the phenomena of electron emission from solid surfaces. Electron emission can be induced by either the kinetic energy of a particle or its potential energy. At higher energies the ion is able to penetrate further into the target material and electrons are primarily emitted via back-scattering and secondary emission processes [*Sternglass*, 1957]. At lower energies, the interaction between the target ion and the surface becomes a function of the potential between them, which results in resonant tunnelling and Auger-type emission processes. Numerous studies have validated that the electron emission flux due to an incident particle with a high kinetic energy is velocity dependent [e.g. *Fraser*, 2002]. The lower limit to this linear dependence upon velocity is as yet not well constrained although studies have shown this limit to be of the order of 10^4-10^5m s^{-1}, or $\sim$1 keV [*Baragiola et al.*, 1979]. Moving towards lower energies the electron yield initially becomes dependent on Potential Emission processes as electrons bound to an ion located externally to a surface interacts with electrons within the surface and trigger electron emission before actually reaching the surface [*Kishinevsky*, 1973].

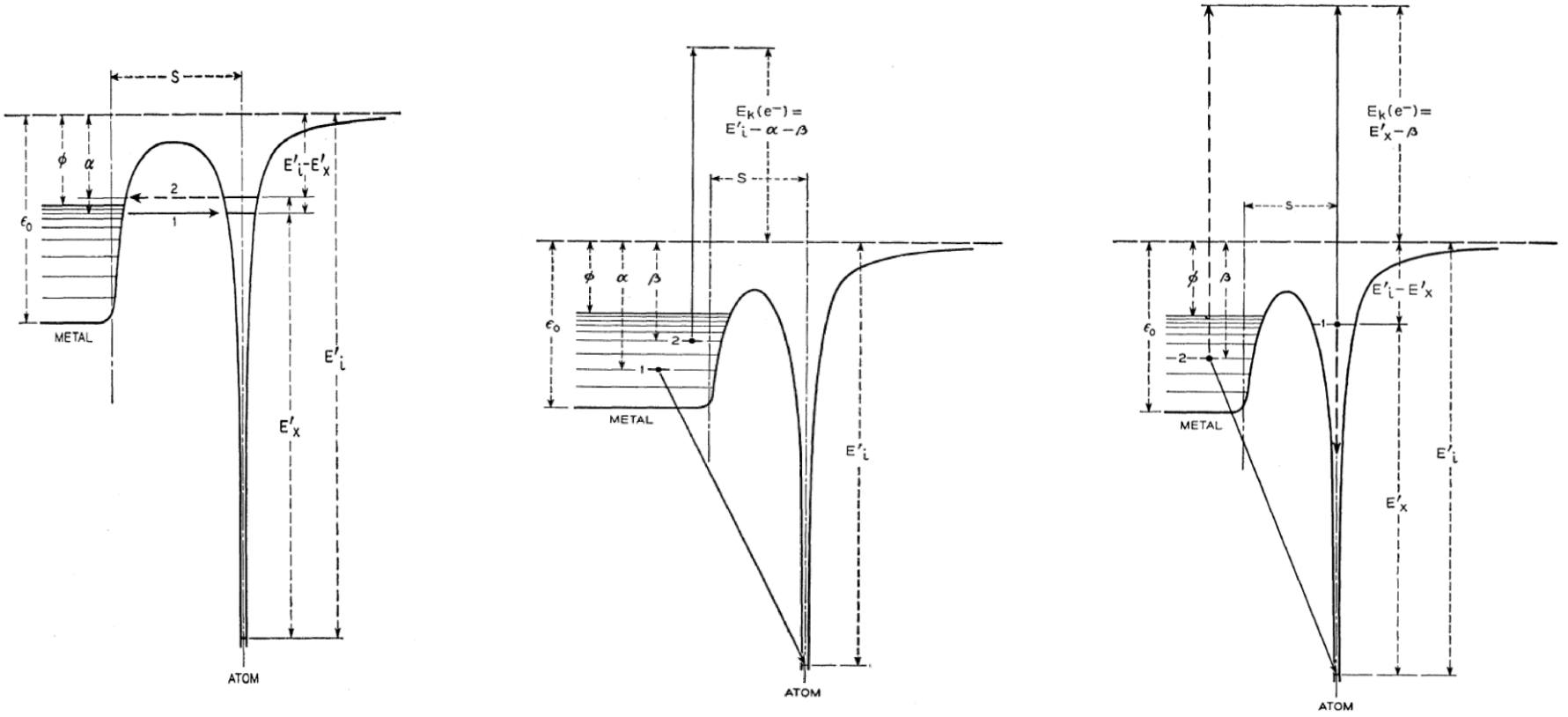

Figure 3.3: Illustration of the electronic transitions resulting from Potential Electron Emission. Resonance neutralisation (Left 1), Resonance ionisation (Left 2), Auger neutralisation (Middle), Auger de-excitation (Right). For further explanation of the processes involved please refer to the source material at *Hagstrum* [1977].

Hagstrum [1977] identifies a two-step potential emission process as dominant, see Figure 3.3. The incoming ion is first neutralised into its ground state, which is followed by a subsequent Auger excitation into an unoccupied state above the Fermi level. Four basic electronic transitions are specified whereby this is achieved. These are; Auger neutralisation as outlined by [*Shekhter*, 1937], Auger de-excitation as discussed by [*Massey*, 1930; *Shekhter*, 1937; *Cobas and Lamb*, 1944], and resonant neutralisation and ionisation [*Oliphant and Moon*, 1930]. To quantify these effects *Kishinevsky* [1973] first determined a physical relationship for the potential yield, where the ground neutralisation of the incoming ion was twice the work function, ϕ, of the target surface. *Baragiola et al.* [1979] improved upon this and subsequently determined the following slightly more accurate empirical relationship,

$$\gamma = 0.032(0.78E_i - 2\phi), \tag{3.17}$$

where, E_i, is the neutralisation energy of the incident ion. The above studies, however, focussed on the case of a positively charged ion impacting upon a surface and the physics of a negatively charged ion with a surface remain to be constrained.

Microchannel plates utilise the phenomena of electron emission for detection purposes. A particle incident on a microchannel plate will cause electrons to be emitted which are subsequently amplified within the narrow channels and causes a cloud of electrons to be emitted, the amount described by the gain function of the MCPs [*Wiza*, 1979]. To calculate the theoretical electron emission flux of a surface bombarded by ions, the matrix elements of the target solid are required, that is the state density function, the transition probability per unit time, and the probability distribution. MCPs are manufactured from lead-silicate glass and involve complex manufacturing and doping processes and as such calculation of the matrix elements is difficult. The emission yields and efficiency functions for MCPs are therefore determined through experimental testing. *Fraser* [2002] derives a universal efficiency function for the efficiency of the MCP, which he applies quite successfully to a number of different datasets. It was in fact this study from which an efficiency value was derived which was applied to the Titan negative ions detections reported by *Coates et al.* [2007a] and *Wellbrock et al.* [2013], the detection of negative ions at Enceladus [*Coates et al.*, 2009] and also the detection of negative nanograins in the Enceladus plumes [*Hill et al.*, 2012; *Dong et al.*, 2015]. This value was used in the absence of laboratory tests to the contrary. This universal model is based on the physics and testing of the MCP response to positive ions, and

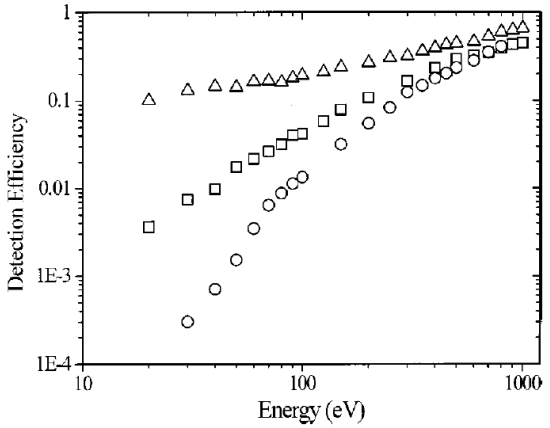

Figure 3.4: Detection efficiencies of O^+ (○), O (□) and O^- (△) [*Stephen and Peko*, 2000].

the model cannot account for experimental results in [*Peko and Stephen*, 2000] and [*Stephen and Peko*, 2000] for negatively charged ions.

Literature relating to the interaction of negatively charged ions with metallic surfaces is sparse and to date only a few experiments have been run for the detection efficiency of MCPs for these species. Several of these studies validate the velocity dependence of electron emission at higher energies [e.g. *Chen et al.*, 2003; *Prasad et al.*, 2013] but few study the physics of the interaction at lower energies. The Cassini CAPS-ELS detection of negative ions are at the lower energy range where potential emission effects are expected to dominate. The energies of interest extent from 150 eV to nearly 2 keV and the only studies relating to this energy range are those of *Peko and Stephen* [2000] and *Stephen and Peko* [2000]. In these investigations, the MCP detection efficiency for positive, negative, and neutral, hydrogen, deuterium, and oxygen was measured at $<$1 keV. It was found that the ratio of the detection efficiency for negatively charged to positively charged ions was greater than one in this energy range and increased significantly with decreasing energy, the disparity eventually spanning two orders of magnitude at the lowest energies. The neutral detection efficiency was found to be higher than the positive ions and lower than the negative ions. In these studies the reason for the increased detection efficiency for negative ions was not discussed, but, with respect to the previous discussions on the process of potential emission, it presumably results from the additional electrons present in a negatively charged ion triggering more frequent, and possibly further, electronic transitions, which result in electron emission ,such as those described for positive ions by *Hagstrum* [1977].

From analysing the detection efficiencies presented by *Peko and Stephen* [2000] and [*Stephen*

and Peko, 2000], see Figure 3.4, it is evident that at a constant particle energy, an increasing mass, which corresponds to a decreased velocity, results in a decreased efficiency. These studies test three different species, hydrogen, deuterium and oxygen, and It is quite plausible that as the mass is further increased, at some point the efficiency will actually also increase as the electronic transition probability will increase due to a greater amount of time spent in proximity to the surface. The quantity of the electron flux emitted due to potential versus kinetic effects is however unknown although the discrepancy between detection efficiencies for positively and negatively charged ions suggest it is a considerable fraction.

3.2.4 Ion Mass Spectrometer

The IMS consists of a top hat toroidal analyser coupled with time-of-flight analyser. Similar to the ELS the ESA steps through 63 energy bins in quasi-logarithmic decrements across an energy range of 1 eV to 50.2 keV. The TOF component uses carbon foils to initiate timing signals for ions bent by a linear electric field, which allows the discrimination between different masses [*Young et al.*, 2004]. A similar MCP set-up is employed to register the incoming particles.

3.3 Hybrid Simulation Technique

The hybrid simulation technique employed in this thesis has been developed from that described in *Winske and Omidi* [1992]. This has been employed extensively in the study of ion-scale instabilities [e.g. *Gary et al.*, 1989; *Convery et al.*, 2002; *Cowee et al.*, 2006; *Omidi et al.*, 2010]. This chapter describes the core equations which are utilised and Chapter 5 provide further information as to the specific simulation set-up for the scenarios examined.

This technique treats ions kinetically and electrons as a massless neutralising fluid. Darwin's approximations of Maxwell's electromagnetic equations are implemented and solved in Gaussian units. Here, the displacement current within Ampere's law is altered to neglect high frequency perturbations such as light waves such that,

$$\nabla \times \mathbf{B} = \frac{4\pi}{c}\mathbf{J}. \tag{3.18}$$

This formulation neglects high frequency perturbations such as light waves and is valid for studying low frequency phenomena. This equation is closed using Faraday's law,

$$\nabla \times \mathbf{E} = \frac{1\partial \mathbf{B}}{c\partial t}, \tag{3.19}$$

and Gauss' law of magnetism,

$$\nabla \cdot B = 0. \tag{3.20}$$

The electrons are specified using a magnetohydrodynamic fluid approximation,

$$\frac{\delta}{\delta t} n_e m_e \mathbf{V}_e = 0 = -eN_e(E + \frac{\mathbf{V}_e \times \mathbf{B}}{c}) - \nabla P_e + en_e R\mathbf{J}, \tag{3.21}$$

with finite electron temperature. The electron pressure and finite electron temperature, T_e, are assumed as isotropic. The resistivity term, R, is used to replace the physical interactions between the electrons and ions and represent the short-wavelength high-frequency anomalous wave-particle scattering due to the electron inertial effects and high frequencies . The electron pressure tensor is expressed as

$$\mathbf{P}_e = n_e T_e \mathbf{1}. \tag{3.22}$$

Within the code quasi-neutrality is enforced instead of solving Poisson's equation such that

$$n_i = n_e + n_{i_{neg}}. \tag{3.23}$$

Ions are treated kinetically within the simulation. The Lorentz force is expressed as

$$m\frac{\delta \mathbf{v}}{\delta t} = e(\mathbf{E} + \frac{\mathbf{v} \times \mathbf{B}}{c}) - e\nu\mathbf{J} \tag{3.24}$$

where the end term accounts for the fluid electrons and corresponds to the end term of Equation 3.21.

The hybrid code is implemented upon a spatial grid where multiple plasma populations are initialised along with a background magnetic field, B_0. The simulation parameters are normalised to the proton gyrofrequency, Ω, the ion inertial length, c/ω_{pl}. Within this formulation, the electromagnetic fields are defined as $e_o\mathbf{E}/m_0\omega_{pi}$ and $e_0\mathbf{B}/m_0\omega_{pi}$ so there are no constants such as 4π or c. Periodic boundary conditions are specified and the simulation is evolved in a leap-frog

timesteps with the fields known at the beginning of each timestep and the particles positions and velocities solved at each half timestep.

This hybrid simulation tool is derived from the original model developed by [*Winske and Omidi*, 1992] and the core equations indeed form the basis for many of the hybrid simulation codes being using today, for example those used in *Cowee et al.* [2008], *Omidi et al.* [2010], and *Fu et al.* [2016]. Codes such as these are extremely powerful in that with modern computer architectures they can be used to represent large physical systems, thereby producing large amounts if quantitative information on the fundamental physical processes examined.

This tool is therefore used in an analogous manner to the Cassini spacecraft. It will be piloted into uncharted waters to perform the first simulation study of this negative ion plasma instability. This will involve careful consideration of the simulation inputs and in-depth examination of the simulation results to verify that the simulation technique is accurately representing the physics at hand. The bulk of the work therefore constitutes understanding how to manipulate the model to produce the desired results and stringent analysis of the results. Following this the simulation results will be analysed with respect to Galileo magnetometer observations to understand whether processes observed at Europa can be better understood.

Chapter 4

Negative ions in Titan's ionosphere

The detections of negatively charged ions and aerosol precursors extending up to 13,800 u/q in Titan's ionosphere [*Coates et al.*, 2007a; *Waite et al.*, 2007] were completely unexpected and remarkable in that they were made by an instrument designed and calibrated for measuring electrons [*Linder et al.*, 1998; *Young et al.*, 2004]. This has presented a number of complications to interpretting the data as the instrument was not specifically designed or calibrated for this purpose. For example, the intrinsic $\Delta E/E$ energy resolution of the instrument is large for mass spectrometric measurements and has limited the positive identification of individual species in previous analyses [*Coates et al.*, 2007a, 2009; *Wellbrock et al.*, 2013]. Spacecraft charging in Titan's ionosphere has also been shown to affect species trajectory when entering the instrument [*Jones et al.*, 2011], thus providing further unconstrained phenomena involved in constraining the detections.

This chapter provides a detailed analysis of the instrument response function to negatively charged ions. An updated model of the instrument response function is developed and successfully applied to these detections. This method is used to statistically identify the lowest mass negative ion species and to constrain the mass ranges of larger negative ion species. The role of these species is then examined with respect to the impending growth of the larger molecules with decreasing altitude.

Results stemming from this chapter have in part been published as an *Astrophysical Journal Letter* with the citation: Desai, R. T., Coates, A. J., Wellbrock, A., Vuitton, V., Crary, F. J., Gonzalez, D. G., Shebanits, O., Jones, G. H., Waite, J. H., Cordiner, M. A., Taylor S. A., Kataria, D. O., Wahlund, J.-E., Edberg, N. J. T., and Sittler, E. C. Carbon chains anions and the growth of complex organic molecules in Titan's ionosphere, *Astrophysical Journal Letters*, 844, 2, L18.

4.1 Introduction

Titan is the second largest moon in the Solar System with radius R_T = 2576 km and possesses a dense extended atmosphere principally composed of ∼96% molecular nitrogen, <4% methane, and <1% hydrogen [*Vervack et al.*, 2004; *Niemann et al.*, 2005; *Waite et al.*, 2005]. Aerosol-type particles envelop the moon in a thick organic photochemical haze [*Danielson et al.*, 1973], a phenomenon also present at Pluto [*Gladstone et al.*, 2016], Triton [*Broadfoot et al.*, 1989], and likely also the Archean Earth [*Miller and Urey*, 1959] and methane rich extrasolar planets. The production mechanisms and composition of these naturally occurring organic compounds are however far from understood.

Solar extreme-UV (EUV), soft X-ray photons, and charged particles from Saturn's magnetosphere, or sometimes shocked Solar Wind, ionise the upper regions and form a significant ionosphere below an exobase of ∼ 1450km. Titan is principally an unmagnetised body [*Wei et al.*, 2010], and ionospheric outflow mass-loads the surrounding space environment [*Cui et al.*, 2010; *Westlake et al.*, 2012; *Coates et al.*, 2012] forming current systems that act to slow down the incident magneto-plasma. This build-up of magnetic flux in front of the conducting obstacle causes magnetic field lines to drape around the moon and form an induced magnetosphere, which diffuses inwards through the moons ionosphere [*Ness et al.*, 1982; *Bertucci et al.*, 2008].

The Cassini spacecraft has sampled the ionised regions of Titan's upper atmosphere down to altitudes of <900 km in-situ and observed positively charged ions (cations) extending up to nearly 1000 u/q [*Crary et al.*, 2009; *Coates et al.*, 2010] and, surprisingly, negatively charged ions (anions) and aerosol precursors extending up to 13,800 u/q [*Waite et al.*, 2007; *Coates et al.*, 2007a, 2009]. The cations were detected at nearly all masses up to 100 u with over 50 species identified in this range [*Cravens et al.*, 2006; *Vuitton et al.*, 2007]. At >100 u, evidence for carbon-based aromatic compounds has been reported, although unique identifications were not possible [*Crary et al.*, 2009; *Westlake et al.*, 2014; *Wahlund et al.*, 2009]. The anions and larger negatively charged molecules were obtained at a lower resolution and classified into broad mass groupings of 12-30, 30-55, 55-90, 90-125, 125-195, 195-625, and 625+ u/q with the higher masses observed at lower altitudes and higher latitudes [*Coates et al.*, 2007a; *Wellbrock et al.*, 2013]. In the deep ionosphere below ∼1000 km the anion/aerosol precursor charge density was observed to exceed that of the electrons resulting in an ion-ion (dusty) plasma [*Shebanits et al.*, 2013, 2016].

A number of studies have modelled the cation and neutral chemistry occurring in Titan's

ionosphere at <100 u/q, but only two studies have attempted to model the anion chemistry [*Vuitton et al.*, 2009a; *Dobrijevic et al.*, 2016]. These focussed on low mass species of <75 u and in particular inferred the presence of the $C_{n-1}N^-$ and C_nH^- anions, where n=2-6. These carbon chain anions have all also been detected in dark molecular clouds, prestellar cores or protostellar envelopes [*Cordiner et al.*, 2013a; *Millar et al.*, 2017], where their reactivity has been identified as acting as a catalyst for the formation of larger larger carbon clusters, unsaturated hydrocarbons and cyanopolyynes [*Millar et al.*, 2000; *Walsh et al.*, 2009; *Cordiner et al.*, 2013b]. These linear anions have also possibly been detected in the Coma of Comet Halley [*Chaizy et al.*, 1991; *Cordiner and Charnley*, 2014]. The presence of significant quantities of negatively charged ions in cold astrophysical environments are facilitated primarily by exothermic radiative processes through electron attachment reactions to high electron affinity neutrals [*Sarre*, 1980] [*Herbst*, 1981] and appear as a ubiquitous feature [*Cordiner et al.*, 2013b]. Larger negatively charged species have since been theorised to exist in these environments with chemical models including higher order carbon-chain anions with up to 23 carbon atoms [*Petrie and Herbst*, 1997; *Millar et al.*, 2000; *Harada and Herbst*, 2008; *Bettens and Herbst*, 1996].

At Titan, chemical schemes are only beginning to provide theories as to how the larger species can be produced. Stochastic charging models provide some explanation for how species of ∼100 u could be ionised and aggregate to form >10,000 u molecules [*Michael et al.*, 2011; *Lavvas et al.*, 2013; *Lindgren et al.*, 2017] but only a few studies have looked at precise chemical routes for producing molecules >100 u. *Westlake et al.* [2014] demonstrate how cations of >100 u are likely formed from smaller hydrocarbon compounds through ion-molecule growth processes and *Ali et al.* [2013, 2015] provided a mechanistic analysis of possible routes from small to large cations of <250 u/q. The latter was based upon Olah's three-membered Hückel aromatic rings [*Olah*, 1972; *Olah et al.*, 2016], and suggest a number of carbocations and their corresponding carbanions are produced through electron attachment to open-shell neutrals. Specific ion and neutral chemistry was not included however and what is still missing is information regarding the intermediary species and chemical pathways leading from the low mass species to the larger negatively charged aerosol-size molecules.

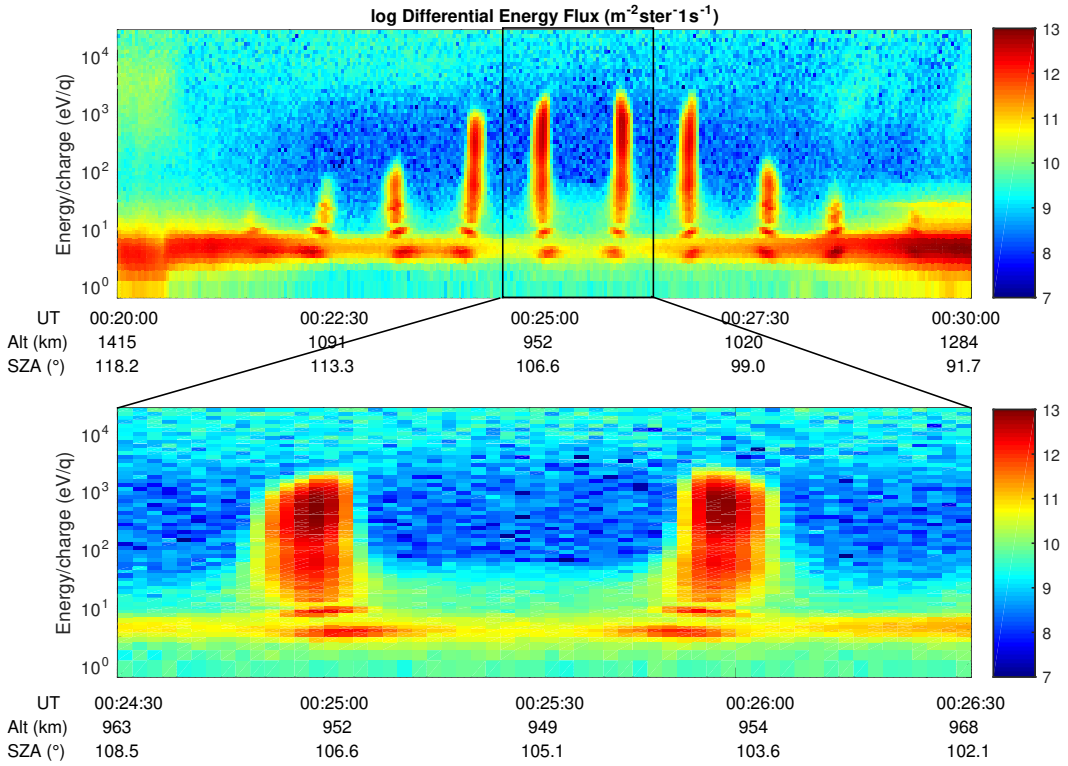

Figure 4.1: *Cassini* CAPS-ELS spectrogram showing the DEF during the T16 encounter. The negative ions are visible as distinct spikes as the ELS samples in the ram direction. The lower panel shows two actuator scans showing that the lower and high mass negative ion detections are temporally separated.

4.2 The CAPS-ELS energy-angle response function

Negative ions were observed as CAPS, located on the Cassini fields and particles pallet, actuated across the spacecraft ram-direction. On closer analysis, however, see Figure 4.1 and also Figure 4.7, it can be seen that these particles don't arrive precisely from the ram direction, in fact arriving at multiple angles of incidence and across multiple energy bins. In order to constrain these observations the energy-angle response of the instrument is examined in some depth.

The energy resolution of the instrument corresponds to the FWHM azimuthal angular acceptance of the instrument as particles entering the ELS aperture at different angles will have different velocity components relative to the electrostatic forces applied by the Electrostatic Analyser. Particles measured in a specific energy bin could therefore possess a kinetic energy 8.5% above or below the specified energy bin depending upon their trajectory. Figure 4.2 shows the energy-angle response function of anode four of the ELS as measured during ground calibration. A schematic of the instrument is also shown to illustrate how this corresponds to a particle entering the ELS

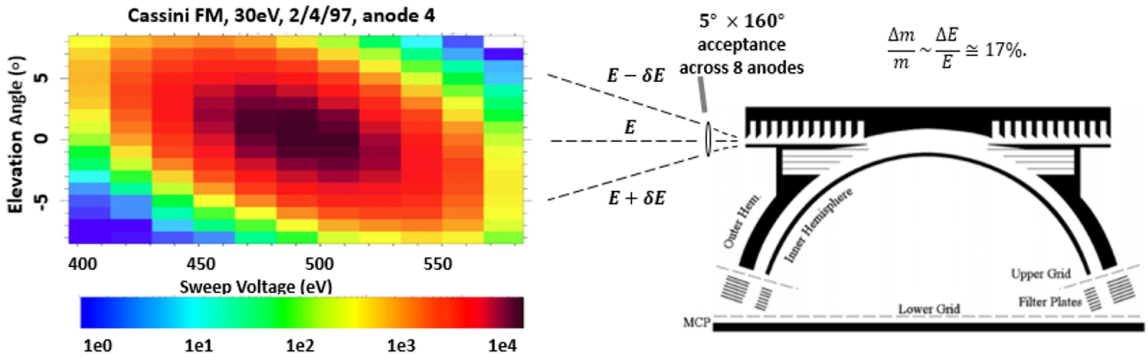

Figure 4.2: The left spectrogram shows CAPS-ELS calibration data recorded at UCL-MSSL on 2nd April 1997 showing the ELS anode 4 response as a function of varying ESA voltage and elevation angle. The schematic to the right shows how this corresponds to a negatively charged particles trajectory when entering the instrument.

aperture. The count rate drops on each side of zero angle of incidence and the bulk of the counts shift in energy as the angle changes. Beyond $\sim 10^{\circ}$ in elevation the count rate has become essentially zero. The quasi-logarithmic increments, which the ELS steps through during a full energy sweep, takes this phenomenon into account such that if the energy of a plasma population falls between two different energy bins, the full distribution is measured across the two neighbouring bins.

Figure 4.3 displays the ELS response to incident electrons with respect to a varying elevation angle and a varying ESA voltage as reproduced from *Linder et al.* [1998]. A Gaussian distribution is also shown fitted to one individual scan to demonstrate the ΔE/E energy resolution is well described by such a distribution function.

In previous analyses, negative ion parameters, such as mass and density per unit charge, have previously been derived from the peak count rate during each azimuthal scan across the spacecraft ram direction [*Wellbrock*, 2012]. The high rate at which the scans in energy are performed, ~ 2 s, compared to the rate at which the sensor is actuated, $\sim 1^{\circ}$/s, allows the fine structure of the anion signatures to be characterised and further information derived than is immediately apparent. In Figure 4.1 the negative ion observations are displayed in high resolution between 00:24:30 and 00:26:30. Here, the low mass negative ions mass are differentiated to some degree but the higher mass detections merge into one another due to the logarithmic increments of the energy scale. Two clear peaks are identifiable at the lower energy range and are observed over a significant time

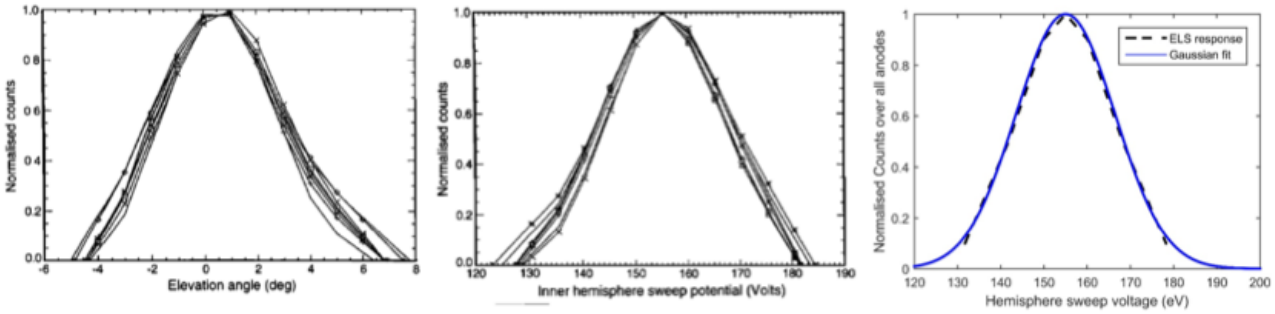

Figure 4.3: The left-hand and middle panels show CAPS-ELS calibration data from *Linder et al.* [1998]. This data corresponds to a two-dimensional slice from Figure 4.2 although this is for a different energy range. The right-hand panels show a Gaussian distribution with a FWHM of 16.7% fitted to the calibration data showing such a function.

scale and angular range. The low and high mass negative ions are also temporally separated with the lower mass negative ions being detected further from the nominal ram direction. This effect has been identified as being imposed by the electric field associated with the spacecraft charging to negative potentials in Titan's relatively dense ionosphere and acting to alter the trajectories of the incoming ions and anions [*Jones et al.*, 2011]. The low mass ions are therefore deflected the most due to their lower inertia and the high mass negative ions deflected the least.

Within the first and second negative ion peaks, the maximum count rates shift towards lower energy bins as the actuator position moves towards the spacecraft ram direction. This effect is most evident for the second peak at $\sim$10 eV. These sub-structures appear to be at odds with the overall physical structure of the negative ion detections where the higher energies, which correspond to higher masses, are detected closest to ram. If each mass group is indeed comprised of multiple species of different masses, as their large mass ranges initially appear to suggest, the higher masses would be consistently detected at a smaller angle to the ram vector. To further analyse this effect we focus specifically on the distinct peak at $\sim$10 eV. In Figure 4.4 the spectra for this range is displayed with each subplot corresponding to a single subsequent energy sweep of the instrument converted into mass per unit charge using Equation 3.16. The horizontal error bars represent the energy resolution of the instrument at FWHM and demonstrate how the energy bins meet at this energy range. The peak of the detections in this group initially appears at $>$50 u at 00:23:50, then reduces down to $\sim$45 u at 00:23:58, and then reduces further to less than $<$40 u at 00:24:06. The reverse structure is also apparent within the next peak near 00:25:45 as the actuator scans in the reverse direction. This shifting of the maximum count rate takes place over multiple successive

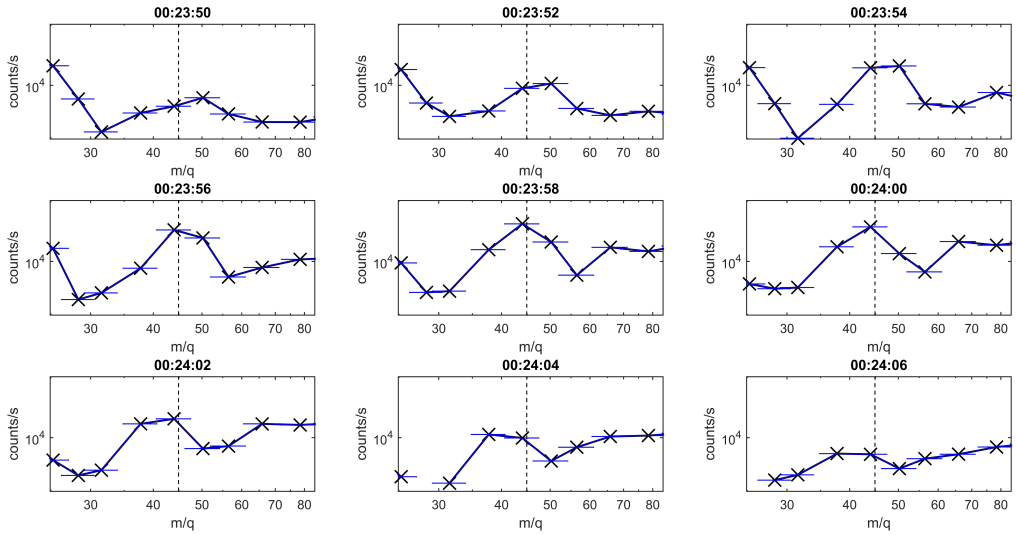

Figure 4.4: CAPS-ELS timeslices taken from Figure 4.1 between 00:23:50 and 00:24:06 for the second peak in the ELS spectrum near 10 eV. The energy/charge is converted to mass/charge using Equation 3.15 neglecting spacecraft potential. The peak can be seen to shift as the ELS actuates across the spacecraft ram direction.

energy bins and appears to corresponds to a range of ≈17% of the centre energy bin.

To further analyse these trends in the data we convolve the energy-angle response of the instrument with the negative ion observations. Using the ground calibration data displayed in Figures 4.2 and 4.3, an energy-angle correction is applied to the Titan dataset in-line with the theoretical anticipated response function. Assuming the maximum count rate as the zero angle of incidence, the counts observed on either side are shifted by the change in energy associated with the angle at which the detections are made. The results of this correction are displayed in Figure 4.5. From this correction it becomes evident that the shift in the peak of the mass group is an artefact of the energy-angle response of the ELS, the instrument detecting the same species in different energy bins as they arrive at different angles of incidence. Within the adjusted energy spectra the peak of mass group two now appears consistently at the same location.

Figure 4.6 now shows the same data displayed as a histogram with a ELS Gaussian response function fitted to the detections. This can be seen to fit well to the data and when plotted together reveals that the peak of the negative ion distribution appears to have been missed by the motion of the actuator. By combining the measurements on either side it is however possible to reconstruct the centre and peak of the negative ion distribution function as is plotted in red. Such a correction is important when converting count rates into number density and also for interpreting the exact

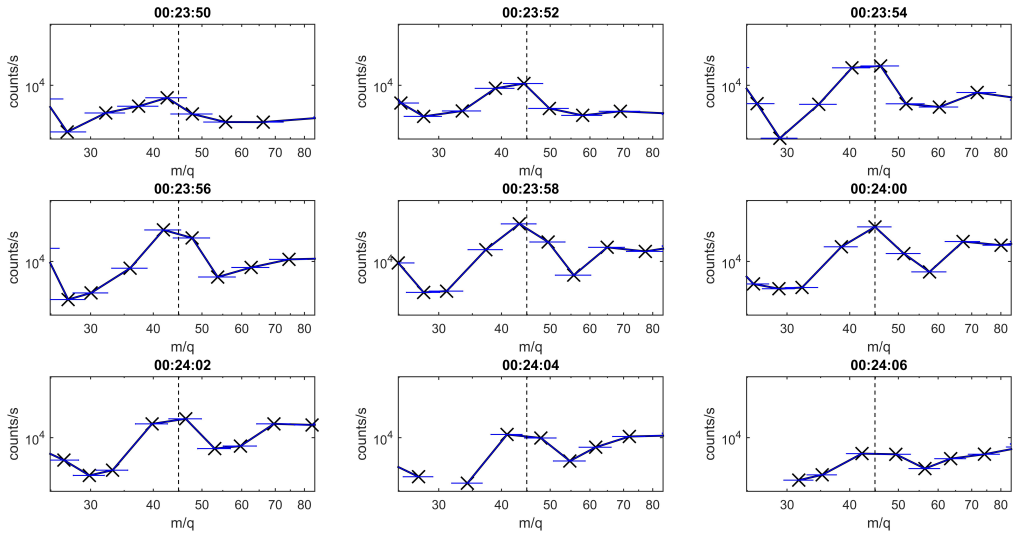

Figure 4.5: Corrected CAPS-ELS timeslices taken from Figure 4.1 between 00:23:50 and 00:24:06 for the second peak in the ELS spectrum near 10 eV. The energy/charge is converted to mass/charge using Equation 3.16 neglecting spacecraft potential and an energy angle correction is applied based upon the ELS response shown in Figure 4.3. The peak now remains fixed as the energy bins, which measure different energies/masses depending upon their angle of incidence.

centre of a distribution function.

4.3 Spacecraft charging

Bodies immersed in a plasma have a tendency to gain a potential according to the current balance between the positively and negatively charged components of a plasma [*Whipple*, 1981],

$$I_{ion} + I_{anion} + I_{photoelectron} + I_{secondary} = 0 \tag{4.1}$$

Solar UV photons impinging upon a surface results in the photoemission of electrons, which drives the potential towards positive values. Conversely a flux of electrons will drive the surface towards a negative potential but also causes the emission of secondary electrons through kinetic and potential effects [*Sternglass*, 1957; *Hagstrum*, 1977]. Incident positively and negatively charged particles will also have a similar effect, acting to charge the surface towards positive and negative potentials respectively. This phenomena has resulted in spacecraft charging to potentials as high as tens of kilovolts [*Whipple*, 1981], and astrophysical bodies acquiring negatively charged surfaces such as observed at the Earth's moon [*Reasoner and Burke*, 1972; *Halekas et al.*, 2002], and the Kronian moon Hyperion [*Nordheim et al.*, 2014]. Determining an accurate value of the spacecraft

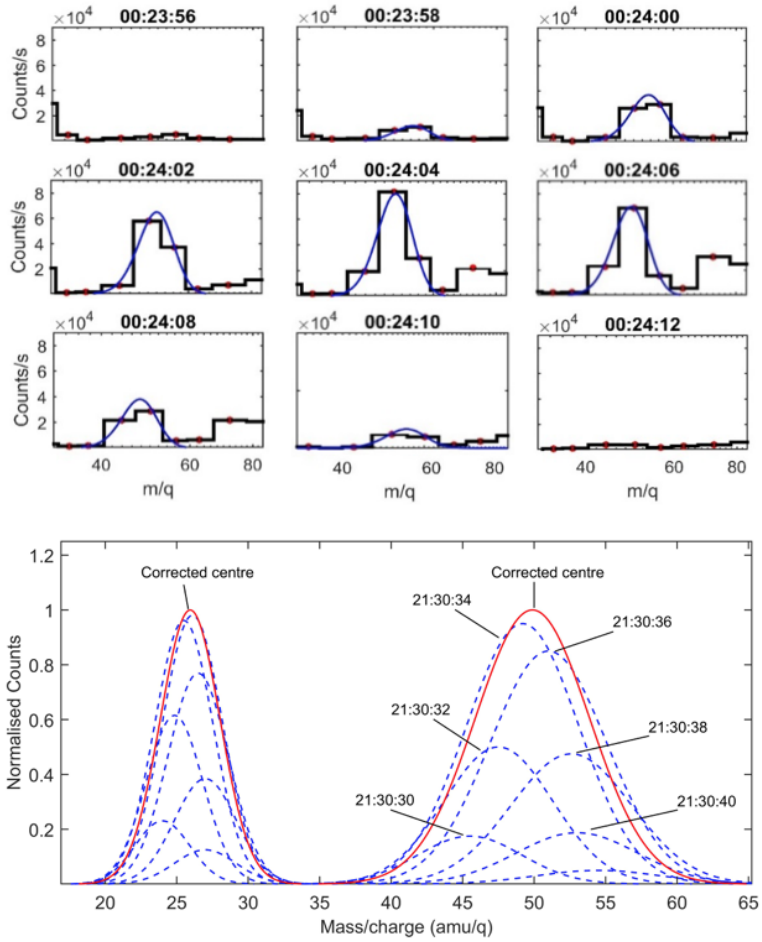

Figure 4.6: (The upper panel displays histograms of CAPS-ELS timeslices taken from Figure 4.1 between 00:23:50 and 00:24:06 for the second peak in the ELS spectrum near 10 eV. The energy/charge is converted to mass/charge using Equation 3.15 neglecting spacecraft potential. The ELS Gaussian response is fitted to these detections at each energy scan. The lower panel displays these Gaussian distributions plotted together and the corrected centre and peak also plotted.

potential remains a significant challenge in the analysis of low energy plasma data as a significant proportion of an incident particle energies can be altered by the potential they experience.

The determination of a positive spacecraft potential from the CAPS-ELS data was first explained in *Rymer* [2004] and also in *Lewis et al.* [2008]. For a positive potential, incident electrons will be accelerated to higher energies, and electrons observed below the potential value are associated with photoelectrons stripped from the spacecraft's surfaces. The division in energy between the ambient electron and the photoelectron populations represents the potential at which the spacecraft is floating. To correct the instrument counts so that only the ambient electrons are observed at their original energy before entering within a Debye length of the spacecraft, the count rates

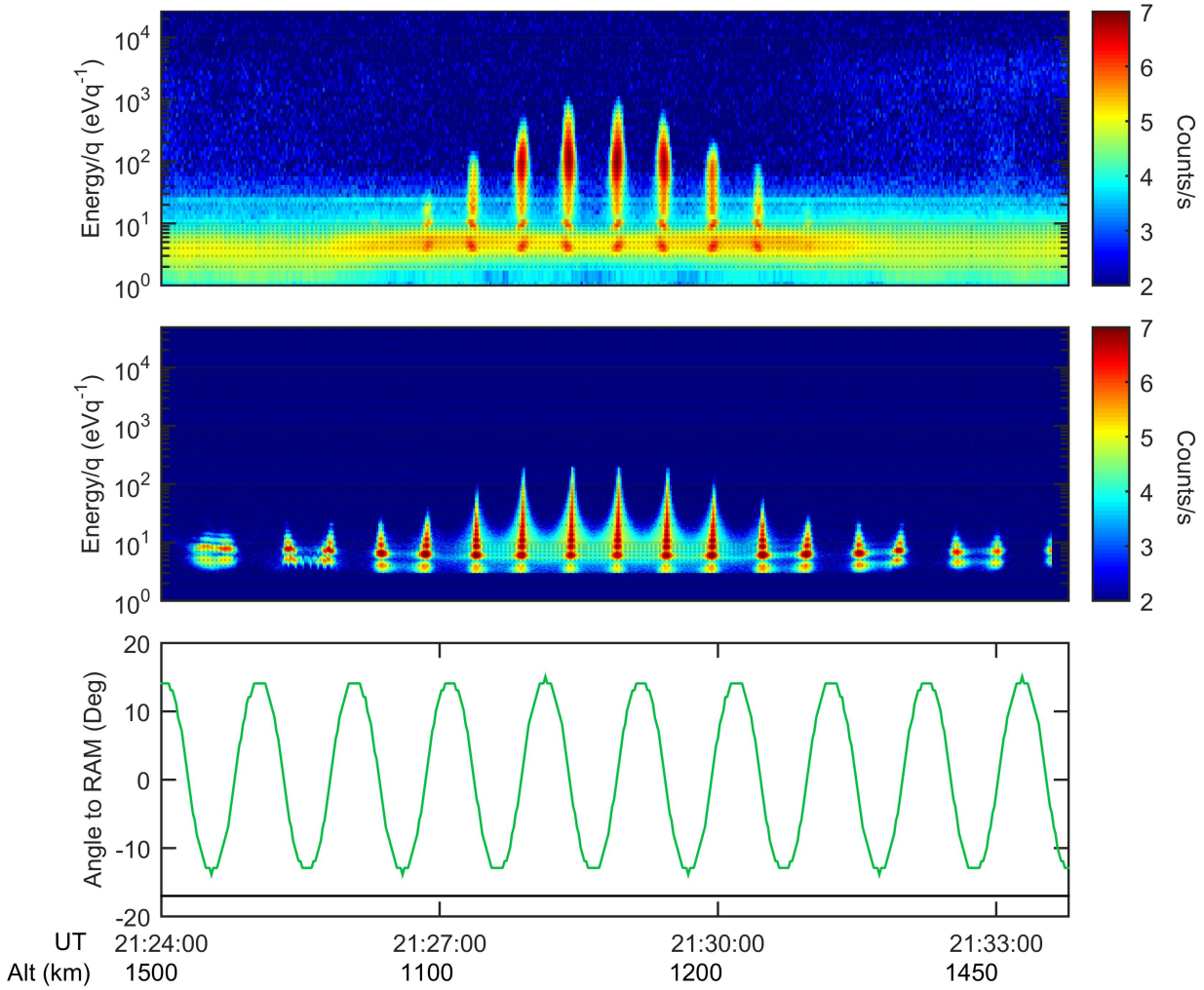

Figure 4.7: The upper panel shows the CAPS-ELS spectrogram of the T40 encounter where the negative ions appear as distinct spikes. The middle panel shows the corresponding CAPS-IBS spectrogram and the lower panel shows the angle of the actuator to the ram direction. The negative and positive ion

must first be converted into phase space and then shifted in energy. This must be carried out in accordance with Louiville's theorem, which specifies that the phase-space distribution function, in this case the positions and velocities of the measured particles, is constant with time. The phase space density can then be converted back into a count rate. To a first approximation, a spacecraft potential can be estimated to be of the order of the electron temperature, due to the relative velocity of electrons with respect to ions resulting in an abundance of electrons sticking to the spacecraft surfaces.

For a negative spacecraft potential, incident negatively charged particles will be retarded and

the lowest energies may not reach the spacecraft. Whilst in Titan's relatively dense ionosphere, Cassini indeed acquires a net negative potential [*Wahlund et al.*, 2005]. The exact current balance is a complex function of the incident currents upon it and the reactions of Titan's chemically complex ionospheric populations with the spacecraft surfaces. Populations of low energy electrons may be present, which cannot be measured be the ELS as they are deflected by the electric field associated charged surfaces.

Chemical modelling of the negatively charged ions and aerosols in Titan's ionosphere have highlighted the lack of literature relating to the reaction rates of many of the exotic species observed at these low temperatures [*Vuitton et al.*, 2009a]. The interaction of the negative ions and aerosols with the spacecraft surfaces with respect to the sticking coefficients and electron emission phenomena represents a significant barrier in theoretically calculating or modelling the spacecraft potential experienced on the various spacecraft surfaces.

Cassini's RPWS Langmuir probe is however able to calculate a potential value through determining the current balance between the positively and negatively charged species. Within Titan's ionosphere the RPWS-LP derived potentials has been reported to be negatively charged but always $\geq$-3.5 V , the reason behind the variation in values not immediately apparent (Shebanits, personal communication, 2016). Whether these values can be directly applied to CAPS data is questionable. The Langmuir probe is located on a 1.5m boom and is coated in titanium-nitride, chosen to enable accurate measurements of a floating potential with respect to the surrounding plasma [*Gurnett et al.*, 2004]. CAPS is however covered by a conductive, carbon impregnated kapton thermal blanket [*Young et al.*, 2004], and could therefore be charging differently to the LP. The location of the LP on a boom also means the measured potential doesn't directly correspond to that on any other part of the spacecraft. As the potential will drop exponentially across the Debye according to $e^{\frac{-r}{\lambda_D}}$, where r is the length of the probe's boom and λ_D is the Debye length, corrective factors need to be applied to the potential at the Langmuir Probe. The spacecraft however isn't a sphere, which presents further complications in accurately applying these corrective factors. Additionally, for an electrostatic analyser, the voltage applied is only a fraction of the measured particle's energy. For example 1 V on the analyser transmits 19 eV for CAPS-IBS and 6.3 eV for the CAPS-ELS. That means an apparent 0.5 eV shift in an IBS peak could be a result of a 0.026 V error in the actual potential on the surface of the plates.

Crary et al. [2009], determined that a corrective factor was required to match the CAPS-

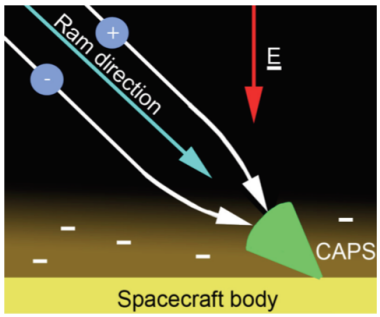

Figure 4.8: Schematic of incoming oppositely charged particle being deflected by the charged spacecraft surface.

IBS ion measurements with those from the Ion and Neutral Mass Spectrometer (INMS), even though these two instruments are situated on the same particle and fields pallet, see Figure 4.8. This lends weight to the idea that differential charging could be occurring on different surfaces of the spacecraft. The corrective factors required in *Crary et al.* [2009] were also determined to have a systematic dependence upon energy. The IBS and ELS electrostatic analysers are tied to a common ground, but they are also coated with a copper oxide to reduce scattered light reaching the detectors. This could potentially introduce resistance and thus capacitance between the metal of the electrodes and the surfaces.

4.4 Spacecraft charging effects

Figure 4.7 shows the CAPS-ELS negative ion signatures as leaning in the opposite direction to the positive ion signatures detected by the CAPS-IBS. This phenomenon has been attributed to the spacecraft potential acting to oppositely deflect incoming positively and negatively charged particles [*Jones et al.*, 2011]. This effect is depicted in in Figure 4.8.

The electric field generated by the spacecraft charging to negative values in Titan's ionosphere is a complex function the plasma interaction of the various surfaces and also the sub-Alfvénic interaction of the spacecraft with the surrounding ionospheric plasma through which it is travelling. This will result in localised effects such as build-up of plasma in front of the spacecraft and a wake region forming behind.

In order to further understand these effects on the CAPS-ELS measurements, the angle at which these detections are made is further examined as a function of the energy bin. Figure 4.9 display the projection of the spectrograms onto the field of view of the ELS. The spacecraft ram direction, parts of Cassini which blocks the ELS FOV, and the local horizon are also displayed. In

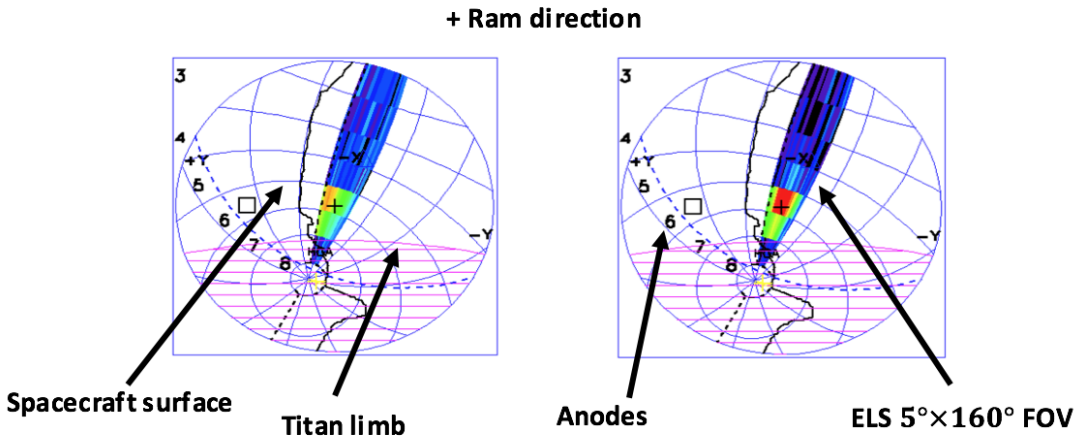

Figure 4.9: (CAPS-ELS FOV projections with the detections of the 3.9 eV (left) and the 22 eV detections (right) overlaid. The data correspond to a full actuator cycle as it scans within a reduced range within Titan's ionosphere. The lower mass negative ions consistently arrive from closer to the spacecraft surfaces (black line) and further from ram (black cross). The local horizon is displayed in pink. [*Jones et al.*, 2011].

these plots the anodes are approximately aligned with the surface of the spacecraft, which the ions are travelling parallel to, and the axis running perpendicular to this surface represents the ELS measuring the ions as function of time and angle as it scans within the reduced angular range. Here, the low mass negative ions are shown to arrive at significantly larger angles to the spacecraft ram direction than the higher mass negative ions. The deflection is always normal to the spacecraft surface and thus compatible with the hypothesis that the negative ions are being deflected away from the spacecraft surface by the negative spacecraft potential, the lower mass ions indeed being deflected more due to their lower inertia.

The orientation of CAPS during the Cassini encounters is such that particles detected will travel parallel to the spacecraft surface for $\sim$1m before being detected. Such an orientation is important as a particle arriving from closer to the spacecraft surface will be subject to a greater electric field strength of that imposed by the spacecraft due to this field decreasing exponentially with distance from the spacecraft. A particle arriving from closer to the spacecraft surface will thus not only be deflected to a greater extent but also subject to a greater force normal to the angular deflection. This force will act to reduce the energy of the particle. Previous corrections to the negative ions energy spectra due to the spacecraft potential could therefore be an oversimplification when trying to obtain an increased accuracy. As a result of this effect, a beam of ions arriving parallel to one another will be deflected by a differing amount and also retarded by a

differing amount as a function of their radial distance to the spacecraft surface. In the spacecraft frame, the mono-energetic beam of a single species of negative ions will thus be altered in energy by a varying amount according to their angle of incidence and hence mass. This phenomenon is compatible with the findings of *Crary et al.* [2009], that an energy dependent corrective factor is required to explain CAPS-IBS observations. It can thus be argued that the lower mass CAPS-ELS negative ion mass groups may be observed over a continuously changing energy range as the result of a single distribution function being subjected to the complex spacecraft-plasma sub-Alfvénic interaction.

To further examine this effect, Figure 4.10 shows the deflection of negative ions detected in the 3.9 eV energy bin during 12 different flybys. The upper six subplots corresponds to flybys where the RPWS-LP measured spacecraft potentials of $>$-1 V and the lower six sub plots correspond to RPWS-LP measured potentials of $<$-1 V. From this grouping it is evident that an increased floating potential on the RPWS-LP corresponds to an increased angular deflection of the negative ion detections. This trend appears to be approximately grouped together in time but does not obviously correspond to any other parameter such as electron density, Solar Zenith Angle or spacecraft attitude. The aforementioned complexity involved in theoretically or analytically calculating spacecraft charging does however limit further analysis of this affect.

4.5 Photoelectrons

A further notable feature in Figures 4.1 and 4.7 is the 24.1 eV photoelectron population produced by the HeII Lyman-alpha (30.4nm) solar line ionisation of N_2 into the A state [*Haider*, 1986; *Galand et al.*, 2006; *Coates et al.*, 2007b, 2011]. This electron population is produced in sunlit regions of Titan's ionosphere and is visible throughout Figure 4.7 and at Solar Zenith Angles of less than 95° in Figure 4.1. Spacecraft charging will result in locally produced photoelectron populations being observed at an energy shifted by the spacecraft potential [*Frahm et al.*, 2006; *Coates et al.*, 2008]. In Titan's ionosphere the N_2 photoelectron population is observed primarily within the 22.2 eV energy bin but with a contribution from the 19.3 eV bin. From Figures 4.11 an ELS correction is calculated to be in the range of -1.0 and -1.6 V, the spacecraft tending to more negative values at lower altitudes. This is lower than the RPWS-LP measurement of -0.8 V, which was acquired at the same time. While the spacing of the ELS energy bins does not allow a more precise measurement of this effect a systematic analysis of this trend throughout further

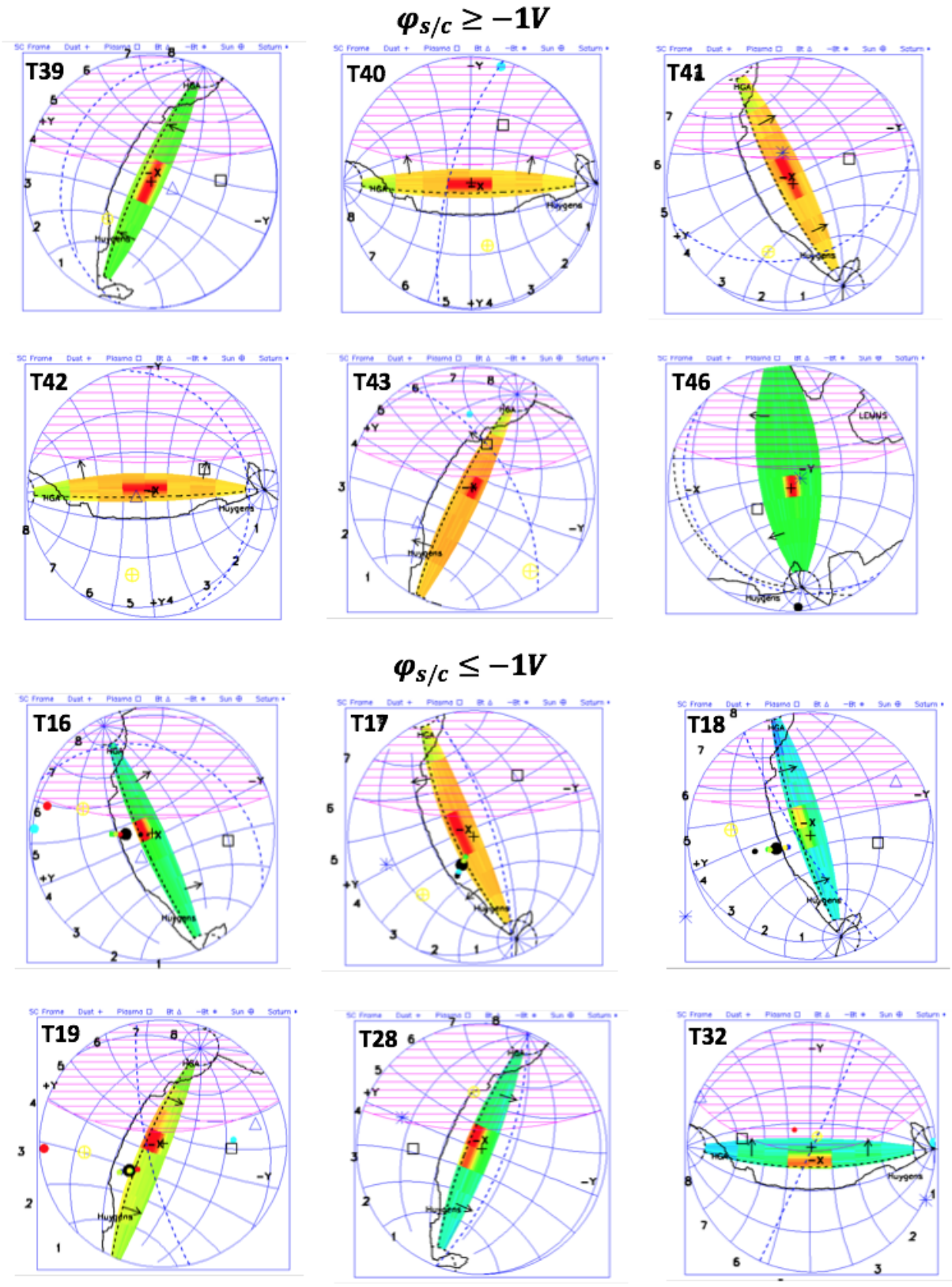

Figure 4.10: CAPS-ELS FOV projections with the detections of the 3.9 eV energy bin overlaid for 12 different encounters. The data correspond to a full actuator cycle as it scans within a reduced range within Titan's ionosphere. The upper six panels corresponds to encounter when the spacecraft potential is $>$ -1 V and the lower panels corresponds to $<$ -1 V. During the increased spacecraft potentials the negative ions arrive at larger angles from the ram direction.

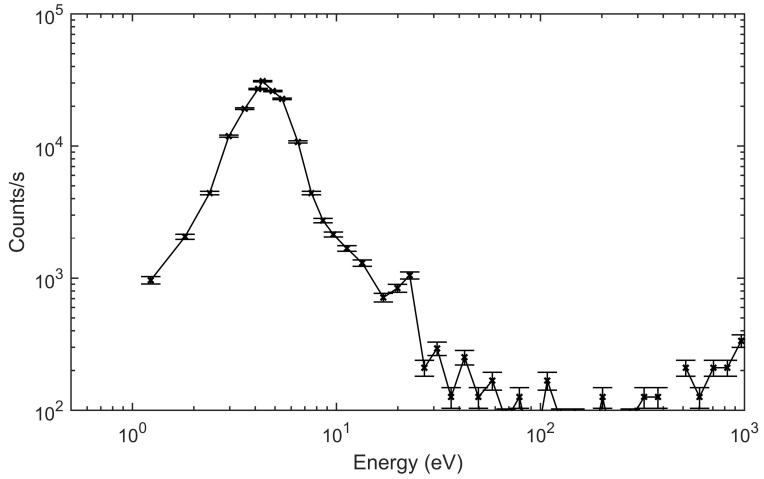

Figure 4.11: CAPS-ELS energy spectrum obtained during the T16 encounter through Titan's ionosphere at 00:29:30. The 24.1 eV photoelectron population is distinct visible above the background distribution function but is shifted due to a negative spacecraft potential into the 19.3 eV and 22.1 eV energy bins.

Titan encounters could further constrain this effect.

4.6 Modelling the negative ion detections

The results presented in this section are derived from CAPS-ELS observations obtained during the T16, T18, T32, T40 and T48 encounters. These include measurements across Titan's sunlit (T16 ingress, T18, T32 ingress, T40, T48) and anti-sunlit (T16 egress and T32 egress) hemispheres, a variety of latitudes and also when Titan was immersed directly within the solar wind (T32). Further information on the geometry and ambient conditions of the Titan encounters can be found in *Coates et al.* [2009].

The CAPS-ELS is a top-hat electrostatic-analyser sensitive to negatively charged particles in the 0.6 - 28,000 eV range [*Young et al.*, 2004]. Anions can be identified within the ELS three-dimensional velocity distribution due to being highly super-sonic in the spacecraft frame and preferentially registering in anodes aligned with the spacecraft velocity vector. Thus as Cassini travels through Titan's ionosphere, the ELS observes an anion mass/charge spectrum,

$$\frac{m}{q} = \frac{2}{q v_{sc}^2} \left(E_{ELS} - \phi_{sc} \right), \tag{4.2}$$

where E_{ELS} is the nominal acceptance energy, v_{sc} is the spacecraft velocity relative to Titan and ϕ_{sc} is the ELS spacecraft potential shift applied in accordance with Liouville's theorem [*Lewis*

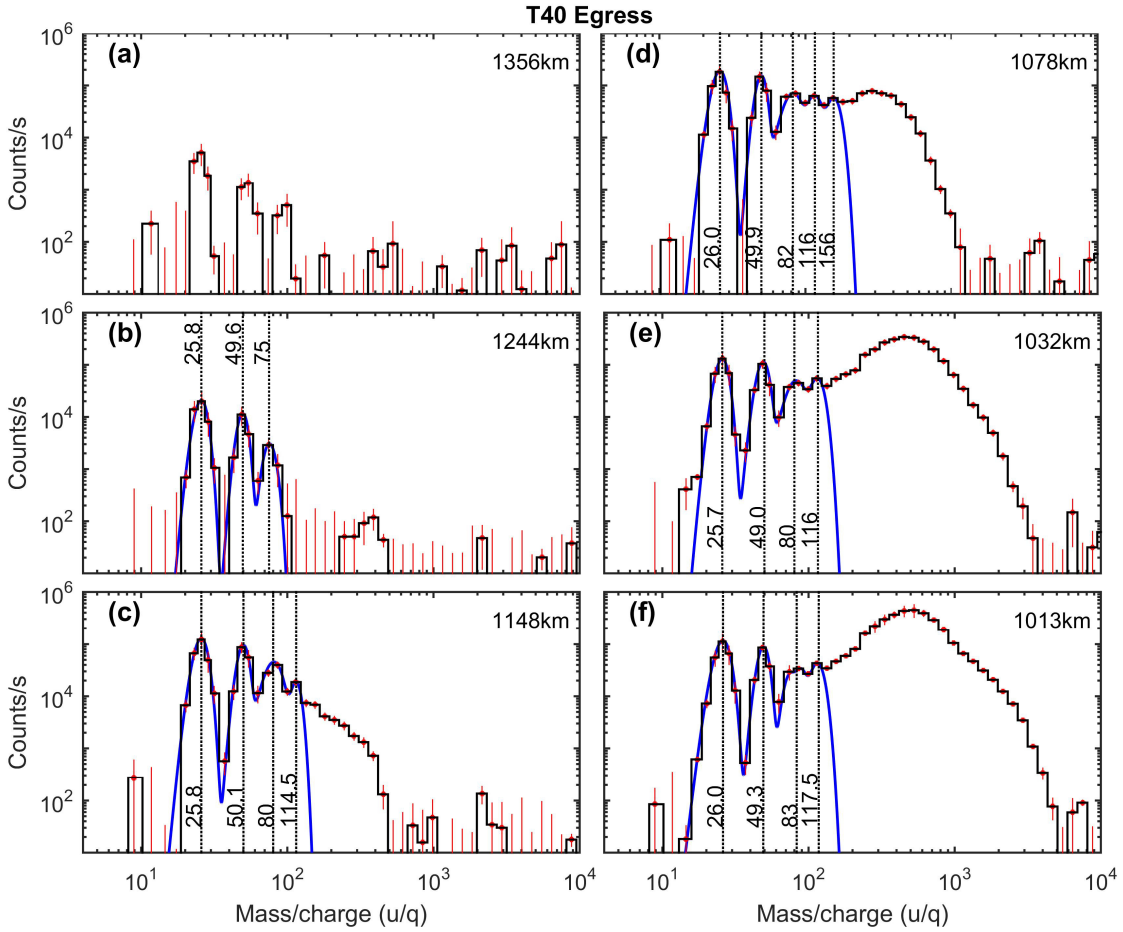

Figure 4.12: Histogram of the CAPS-ELS anion ion mass/charge spectrum at various altitudes within Titan's ionosphere during the T40 encounter. The fitting routine (blue) and errorbars (red) are calculated as described in Equations 4.2-4.8. The nominal centre of each group is marked (dotted black line) and the fitting parameters are given in Table 5.1.

et al., 2008].

To isolate the anion detections, the count rates are taken from each scan across the ram direction and the isotropically observed electrons on non-ram pointing anodes averaged and subtracted. The count rate R_C, can then be related to the number density, n_{ni}, using the ion current approximation [*Waite et al.*, 2005; *Coates et al.*, 2007a],

$$n_{ni} = \frac{R_c}{v_{sc} A_F \varepsilon}, \tag{4.3}$$

where $A_F = 0.33$ cm^2 is the effective area of acceptance, and ε is the Microchannel Plate (MCP) anion detection efficiency function which is energy dependent. A value of $\varepsilon = 0.05$ was used in previous studies based upon the extensive study by *Fraser* [2002], which remains the best estimate

for the larger species. Studies have however shown that at lower energies this could be significantly larger for negatively charged molecules [*Stephen and Peko*, 2000; *Peko and Stephen*, 2000] where electron multiplication is increasingly dependent on potential as well as kinetic emission processes [*Hagstrum*, 1977].

The ELS energy bins are quasi-logarithmically spaced to match the energy resolution and overlap at FWHM and results in a nominal electron or anion distribution registering counts across multiple energy bins. To take this into account we forward model the ELS response to negative ions. The ELS $\Delta E/E$ resolution can be represented using a normalised Gaussian of the form

$$f(E) = R_{nc} \exp\left(-\frac{1}{2}\left(\frac{E-E_0}{E_W}\right)^2\right) \tag{4.4}$$

where E_0 is the center of the distribution, E_W is the width and R_{nc} is the normalised count rate. Here, E_W corresponds to $\Delta E/E = 16.7\%$ in the case of a single anion distribution but can be larger in the case of multiple overlapping distributions close together. The thermal energy spread of the anions is approximated by a drifting Maxwellian expressed in count rates,

$$g(E) = \frac{2nE^2G}{\sqrt{m}}\left(\frac{1}{2\pi kT}\right)^{\frac{3}{2}} \exp\left(-\frac{(E-E_0)}{kT}\right), \tag{4.5}$$

as adapted from *Rymer et al.* [2001] for the case of a drifting Maxwellian in the spacecraft frame, where T is the ion temperature in Titan's ionosphere and G the geometric factor,

$$G = A_F \frac{\Delta E}{E}\varepsilon, \tag{4.6}$$

which is derived under the assumption that the negative ion current fills the ELS aperture. The ion temperature in Titan's ionosphere has been determined to be significantly less than the $\Delta E/E$ instrument sensitivity and tests with or without this thermal contribution produced similar results. In this study it is therefore held constant at $kT = 0.02$ eV ($\sim$150K) [*Crary et al.*, 2009] and included for completeness. The ELS response function and the anion distribution can then be convolved,

$$h(E) = f(E) * g(E), \tag{4.7}$$

and the resulting function modelled to fit the observed data using a χ^2 minimisation routine. Of further mention is that the spacecraft surfaces charge to negative values in Titan's relatively dense

ionosphere and the various surfaces will also charge to different potentials based upon variations in material conductivities and incident electron and ion currents [*Crary et al.*, 2009]. This results in the exact potential correction, ϕ_{sc}, also being unknown and the centers of the fitted distributions are therefore established relative to one another. Errors in the observed count rates are taken as

$$\sigma = \sigma_p + \sigma_{std} \tag{4.8}$$

where σ_p corresponds to the Poisson counting statistics and σ_{std} corresponds to the standard deviation of counts on non-ram oriented anodes. This is used as a measure of electron anisotropies and inter-anode scaling uncertainties, introduced when isolating the anion detections.

4.7 Results & Analysis

Figure 4.12 shows the anion mass/charge spectrum measured at various altitudes during the T40 encounter. At higher altitudes ($>$ 1300 km) the larger $>$100 u/q species are absent and at the highest altitudes it is difficult to identify anions due to decreased densities. As Cassini descends, clear detections appear at $<$200 u/q and the larger $>$200 u/q distribution starts to grow below $\sim$1250 km. The five resolved clustered detections in the spectra are hereafter referred to as peaks 1-5 and fall within the range of mass groups 1-5 as described by *Wellbrock et al.* [2013]. Figure 5.3 also shows anion spectra obtained during encounters T16, T18, T32 and T48.

The fitting procedure applied to peaks 1 and 2 finds the center of the primary two peaks to be separated by $23-24.3$ u/q in all encounters, see Table 5.1. Chemical models for Titan's atmosphere predict efficient production of C_nH^- and $C_{n-1}N^-$ to result from dissociative electron attachment to, or de-protonation of, parent neutral species C_nH_2 and $HC_{n-1}N$ [*Vuitton et al.*, 2009a; *Dobrijevic et al.*, 2016]. For example, CN^- and C_3N^- are produced by

$$HCN + e^- \rightarrow H + CN^-, \tag{4.9}$$

$$HC_3N + CN^- \rightarrow HCN + C_3N^-, \tag{4.10}$$

which proceeds rapidly due to abundant HCN and HC_3N. A similar reaction sequence exists for hydrocarbons where C_2H^- and C_4H^- are produced by

Table 4.1: Fitting Results for Peaks 1-5 in the CAPS-ELS Anion Mass/Charge Spectrum at <200 u/q. The reduced χ^2 values are for 3 DOF fits within the 20-60 u/q range and the super- and sub-scripts represent a 2 σ deviation. Here, note that for p=0.05, χ^2=2.60. The ELS FWHM for a single distribution is 16.7% and the spacecraft potentials correspond to the nearest RPWS-LP measurement to closest approach.

			Peak 1		**Peak 2**		**Peak 3**	**Peak 4**	**Peak 5**	**Potential** (Φ_{sc})	
Flyby (#)	**Alt (km)**	χ^2 **(-)**	**Centre (u/q)**	**FWHM (%)**	**Centre (u/q)**	**FWHM (%)**	**Range (u/q)**	**Range (u/q)**	**Range (u/q)**	**RPWS-LP (V)**	**ELS (V)**
T40	1244	$\rightarrow$0	$25.8^{+0.8}_{-0.6}$	$20.1^{+2.6}_{-4.6}$	$49.6^{+1.8}_{-1.5}$	20.9+	72-78	-	-	-0.63	-1.05
-	1148	1.50	$25.8^{+0.9}_{-0.5}$	$21.7^{+2.1}_{-3.3}$	$50.1^{+1.1}_{-0.8}$	$17.9^{+1.5}_{-2.7}$	71-89	109-120	-	-0.59	-1.20
-	1078	0.67	$26.0^{+0.4}_{-0.6}$	$21.6^{+0.6}_{-2.8}$	$49.9^{+2.0}_{-1.1}$	$17.0^{+2.2}_{-3.5}$	73-91	108-122	146-166	-0.58	-1.20
-	1032	0.72	$25.7^{+0.5}_{-0.5}$	$22.7^{+0.6}_{-2.0}$	$49.0^{+0.8}_{-0.5}$	$19.6^{+1.4}_{-2.0}$	73-91	109-123	-	-0.57	-1.20
-	1013	2.46	$26.0^{+0.8}_{-0.6}$	$22.7^{+1.9}_{-2.9}$	$49.3^{+0.6}_{-0.6}$	$18.1^{+1.0}_{-1.6}$	72-94	107-128	-	-0.59	-1.20
T16	1031	0.88	$25.9^{+0.4}_{-0.6}$	$22.8^{+2.5}_{-6.0}$	$48.9^{+0.7}_{-0.7}$	$19.6\ ^{+1.6}_{-2.2}$	72-77	108-118	141-160	-0.66	-1.40
T18	969	0.73	$26.0^{+0.9}_{-1.0}$	$22.8^{+3.7}_{-6.2}$	$49.0^{+1.5}_{-0.7}$	$17.0^{+2.0}_{-2.1}$	74-82	113-123	148-166	-1.65	-2.50
T32	1036	0.92	$25.8^{+0.6}_{-1.1}$	$18.5^{+3.7}_{-2.4}$	$49.5^{+0.8}_{-1.2}$	$18.5^{+1.8}_{-3.5}$	74-94	114-125	-	-0.80	-1.55
T48	1082	2.18	$26.0^{+0.2}_{-0.2}$	$18.3^{+0.7}_{-0.4}$	$49.7^{+0.7}_{-0.6}$	$17.7^{+1.1}_{-1.8}$	74-88	110-121	147-164	-0.80	-1.40

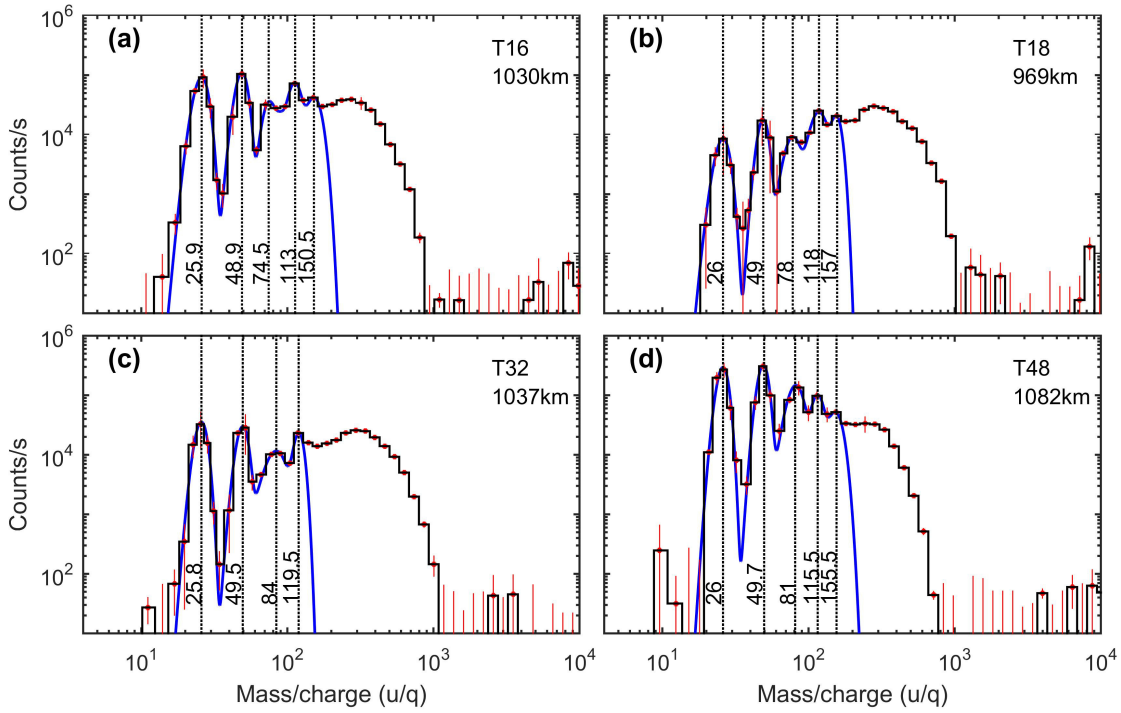

Figure 4.13: Histogram of the CAPS-ELS anion mass/charge spectrum during the T16, T18, T32 and T48 encounters. The fitting routine (blue) and errorbars (red) are calculated as described in Equations 4.2-4.8. The nominal centre of each group is marked (dotted black line) and the fitting parameters provided in Table 5.1.

$$C_2H_2 + e^- \rightarrow H + C_2H^-, \tag{4.11}$$

$$C_4H_2 + C_2H^- \rightarrow C_2H_2 + C_4H^-. \tag{4.12}$$

due to abundance C_2H_2 and C_4H_2. This $23-24.3$ u/q separation in the ELS mass/charge spectrum is indicative of these processes and the CN^-/C_2H^- and C_3N^-/C_4H^- carbon chain anions as the dominant constituents within the primary and secondary peaks respectively. It is not possible to further resolve the 1 u difference between these nitrile and hydrocarbon compounds but CN^- is estimated to be two orders of magnitude more abundant than C_2H^-, and C_3N^- and C_4H^- are predicted in comparable abundances [*Vuitton et al.*, 2009a]. The main anion loss process considered is associative detachment with neutral radicals.

The width of the primary peak is however often larger than the ELS $\Delta E/E \approx 16.7\%$. This can be explained by a multi-species composition, with further possible anion species such as C_2^-, $CH^-_{1,2,3}$, $NH^-_{1,2,3}$ and CO^- possibly contributing, the latter due to the introduction of water-group

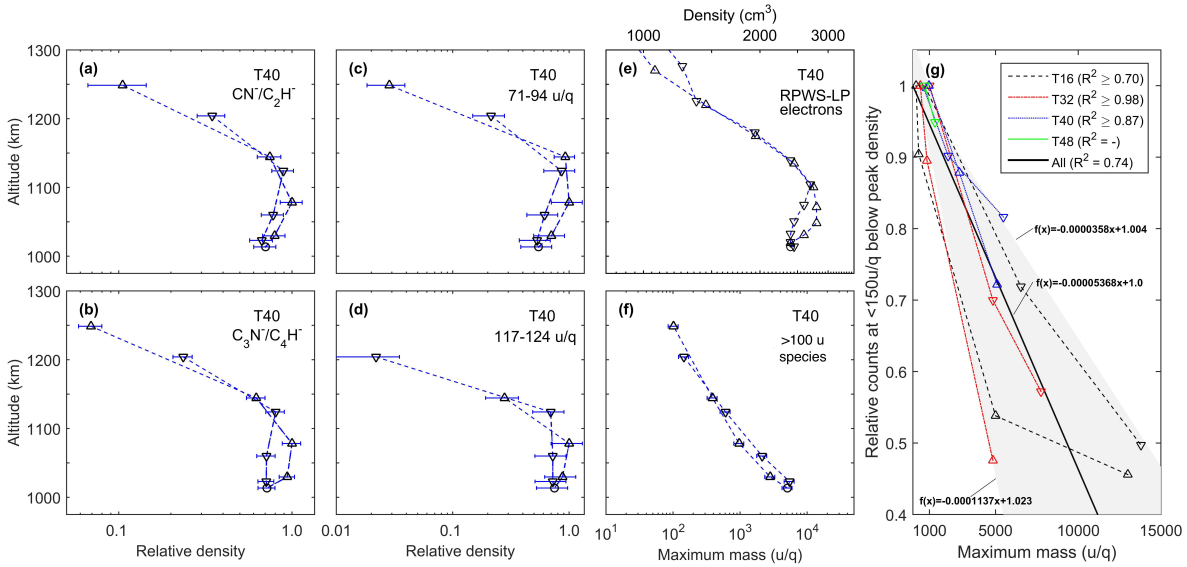

Figure 4.14: Altitude profiles with ingress (△) and egress (▽) marked. (a-d) Shows the T40 relative anion densities, (e) the electron density, (f) the maximum mass detected and (g) the correlation between the depletion of the low mass ($<$ 150 u/q) anions below the altitude of peak density and corresponding increase in the maximum mass. A linear trend line (black) is fitted as well as individually to the ingress and egress of each encounter, the maximum and minimum of which encompass the region shaded grey. Relative errors are assumed small compared with the overall spread.

ions (O^+, OH^+, H_2O^+, H_3O^+) from Enceladus [*Hartle et al.*, 2006; *Cravens et al.*, 2008]. It is however possible that the spacecraft potential also acts to spread a given distribution's energy relative to the spacecraft, an effect which would be more pronounced for lower mass ions due to their lower inertia. The width of the secondary C_3N^-/C_4H^- peak falls across a range which encompasses the FWHM of the ELS, indicating this is likely composed of a single distribution function with only a minor contribution from further species possible.

This analysis indicates the spacecraft potential experienced by the ELS is $0.4-0.9$ V more negative than that measured by the Radio and Plasma Wave Science (RPWS) Langmuir Probe (LP) although within the -3.5 V absolute range observed by the instrument in Titan's ionosphere [*Crary et al.*, 2009]. An ∼-0.3 V discrepancy was found between conjugate CAPS Ion Beam Spectrometer (IBS) and Cassini's Ion and Neutral Mass Spectrometer (INMS) observations [*Crary et al.*, 2009] and a more negative spacecraft potential correction is expected for anion detections [*Jones et al.*, 2011]. This is due to focussing effects where the spacecraft-generated potential field acts to deflect incident ions such that the anions arrive from a direction closer to the spacecraft surface.

At 1244 km (Figure 4.12b) the third peak is also visible where at higher altitudes it appears compatible with C_5N^-/C_6H^-, although this cannot be statistically verified as at >50 u/q there are fewer measurements than free parameters. At lower altitudes this peak widens, extending as high as ∼94 u/q in some instances. This range does not include any previously observed anions and indicates the presence of anionic structures other than linear chains. INMS and CAPS-IBS measurements at these altitudes also show a grouping of neutrals and cations over a similar range [*Waite et al.*, 2007; *Crary et al.*, 2009], the most abundant of which was inferred to be benzene (C_6H_6) [*Vuitton et al.*, 2008]. This is particularly relevant as benzene and benzene products are thought to be the seeds for larger aromatic compounds [*Vuitton et al.*, 2009b]. The lack of reaction rates and known chemical pathways at these high masses severely restricts the analysis of the anion chemistry but several candidate species can be suggested. For example, the cyclic radical $C_6H_5^+$ is observed in appreciable quantities [*Vuitton et al.*, 2009b] and can be a source for $C_6H_5^-$ anion radical production [*Fenzlaff and Illenberger*, 1984]. The stable $C_6H_7^-$ cyclic anion can also be produced through the interaction of benzene with H^- [*Coletti and Re*, 2012]. H^- cannot be measured however due to constraints imposed by the spacecraft velocity, see Equation 4.2, but H^- fluxes can result from the interaction of methane with ionospheric electrons [*Dobrijevic et al.*, 2016].

The four further encounters in Figure 5.3 also show this third peak to be the most variable between encounters, possibly indicating an enhanced sensitivity to the ambient conditions. A number of azine anions resulting from benzene, pyridine, pyridazine, pyrazine, and s-triazine have been explored by *Wang et al.* [2015] with application to Titan, and determined to be highly reactive with nitrogen and oxygen. These include $C_6H_3^-$, $C_5H_2N^-$, $C_5H_3N^-$, $C_5H_4N^-$, $C_4H_3N_2^-$ and $C_3H_2N_3^-$ and are of high astrobiological interest. The higher end of this third mass range is however less explored and further anions such as the benzyl anion $C_7H_7^-$ and anilinide anion $C_6NH_6^-$ [*Wang and Bierbaum*, 2016], could be derived from the > 20 mostly Polyaromatic Hydrocarbons and nitrated heterocyclic species suggested in this range.

At altitudes <1200 km a fourth distinct peak, with consistent detections at ∼117±3 u/q, is identified during every encounter. This appears at count rates comparable to the primary peaks and sometimes double that of the neighbouring peaks. This is most evident during T16 where the highest mass species at 13,800 u/q were observed [*Coates et al.*, 2009]. A smaller fifth peak, with detections consistently at ∼154±8 u/q, is also sometimes present.

The >100 u/q regime is however even more unconstrained with the further peaks at >100 u/q notably not occurring at further carbon-chain multiples and therefore also pointing to the role of more complex structures. The $114-120u/q$ and $148-164u/q$ range corresponds to a number of aromatic hydrocarbon and hetorocyclic anionic compounds, which could result from the cationic chemistry identified in *Crary et al.* [2009] and *Ali et al.* [2015]. Anionic species in the $114-120$ u/q range include the indenyl anions $C_9H_7^-$ and $C_9H_8^-$, the cyclononatetraenyl anion $C_9H_9^-$ and their heterocyclic counterparts where a function CH group is replaced by a Nitrogen atom [*Wilson and Atreya*, 2003]. Within the slightly larger $148-164$ u/q range the $C_{12}H_{8-13}$, have all been suggested as constituting the IBS mass/q spectrum [*Crary et al.*, 2009; *Ali et al.*, 2015] and, together with their heterocyclic counterparts $C_{11}H_{7-12}N$, could feasibly exist in a negatively charged state. It should be noted that *Trainer et al.* [2013] detected ring structures near 117 u in laboratory simulations of aerosol-tholin production, which could represent growth processes involving aromatic rings observed by the ELS at Titan. These further peaks show the negative charge in Titan's upper atmosphere markedly transfers from carbon chains to more complex structures below $\sim 1200km$.

Multiply charged anionic states are not considered here due to interelectron repulsive forces making this phenomena increasingly unlikely for smaller molecules. This is evident as the smallest known multiply charged anions, C_n^{2-} (n=7-28), have lifetimes of tens of micro-seconds in the gas phase whereas the larger $C_{60,70}^{2-}$ molecules can persist for milliseconds [*Wang and Wang*, 2009]. It therefore appears that multiple charges are much more likely on molecules larger than a few hundred u in Titan's ionosphere, as indeed was reported by *Shebanits et al.* [2016].

4.8 Molecular growth

Figure 4.14 (a-d) shows the altitude profiles of peak 1 (25.8-26.0 u/q, associated with CN^-/C_2H^-), peak 2 (49.0-50.1 u/q, associated with C_3N^-/C_4H^-), peak 3 (71-94 u/q), and peak 4 (107-123 u/q) during the T40 encounter. Figure 4.14 (e-f) shows the electron densities and maximum detected mass of the larger molecules as obtained in *Coates et al.* [2009]. The altitude profiles in Figure 4.14 show the carbon chain anions to peak in density above the region where the highest mass aerosol monomer are observed and to extend several scale heights above this to where the larger species are not present in measurable quantities. While the precise relative densities are not known, the profiles show the negative charge to be increasingly carried by the larger species at lower altitudes. This trend is also observed in further encounters, see *Wellbrock*

et al. [2013], Figure 3.

Below ∼1100 km the depletion of the <150 u/q anions can be seen to be related to the size increase of the larger molecules. Figure 4.14 (g) shows this correlation for all encounters except T18, which was omitted as the altitude of peak density of the low mass ions was not definitively surpassed (indeed during T48 this was only surpassed for a brief instance). The two parameters can be seen to be linearly proportional although there is some spread to the data at the higher masses. This overall proportional decrease in the low mass species with the increase of the larger species points to dependencies between these.

The data also point to a possible diurnal variation with the day-side measurements grouped together at and above the fitted trend line (black) and the night-side measurements appearing below this and with T16 and T32 crossing Titan's solar terminator. *Coates et al.* [2009] previously determined significant spatial variations of the high mass monomers and these data point to this being echoed in the smaller species. Further statistical analyses are however required to fully disentangle such influences.

Figure 4.15 shows the altitude profiles for this Titan encounter. The errorbars correspond to MCP efficiency limits of 0.05 and 0.5 as take from the studies of *Fraser* [2002]; *Peko and Stephen* [2000]; *Stephen and Peko* [2000], the lower and upper limits deriving from positively and negatively charged MCP efficiencies respectively. Despite the limited number of scans across the ram direction, the rough trend is evident in Figure 4.15 and in further encounters (not shown) that each successive higher mass anion grows and peaks at a successively lower altitude. The $C_xN^-(x = 1,3,5)$ anions and further peak at 113±5 u/q also appear to have reached their altitudes of peak density within the altitude range that Cassini observed of >950km.

The apparent agglomeration process observed in the ELS dataset is in good agreement with aerosol charging models of Titans ionosphere, which indicate that species of <10nm (>100 u) are the seed particles for the growth of more massive species [*Michael et al.*, 2011; *Lavvas et al.*, 2013]. The intermediary species in the ELS mass spectrum may therefore present the first opportunity to understand the direct production processes and composition of Titan's haze particles. This concept is schematically represented in Figure 4.16, which was produced by ESA with the publication of *Desai et al.* [2017a].

Further comparisons can also be drawn to molecular clouds beyond our Solar System where *Lepp and Dalgarno* [1988] showed negatively charged PAH molecules could outnumber electrons

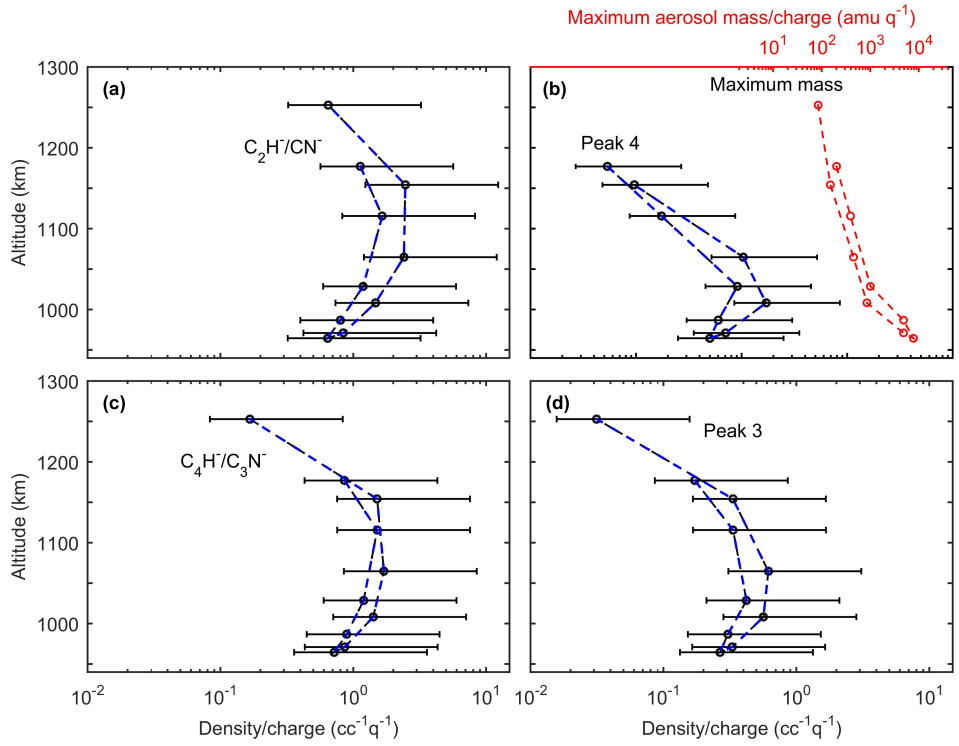

Figure 4.15: Altitude profiles with ingress (△) and egress (▽) marked. (a-d) Shows the T40 relative anion densities, (e) the electron density, (f) the maximum mass detected and (g) the correlation between the depletion of the low mass ($<$ 150 u/q) anions below the altitude of peak density and corresponding increase in the maximum mass. A linear trend line (black) is fitted as well as individually to the ingress and egress of each encounter, the maximum and minimum of which encompass the region shaded grey. Relative errors are assumed small compared with the overall spread.

and simulations of the L1275 protostellar core by *Harada and Herbst* [2008] demonstrate that the abundance of high mass carbon-bearing negatively charged molecules could eventually outnumber the lower mass molecules. An analogous trend appears within the the ELS mass spectrum where the high mass negative ions appear at higher count rates to the lower mass negative ions deep within Titan's ionosphere. A trend of decreasing MCP efficiency with increasing mass is also expected which would revise the surprising ratio ($>$1) of high to low mass negative ion densities further upwards from the current estimates which use a uniform MCP efficiency.

4.9 Summary & Conclusions

This study carried out a detailed model of the CAPS-ELS response function to negative ions and determined the following:

- The change in energy of each negative ion group as CAPS scanned across the ram direction

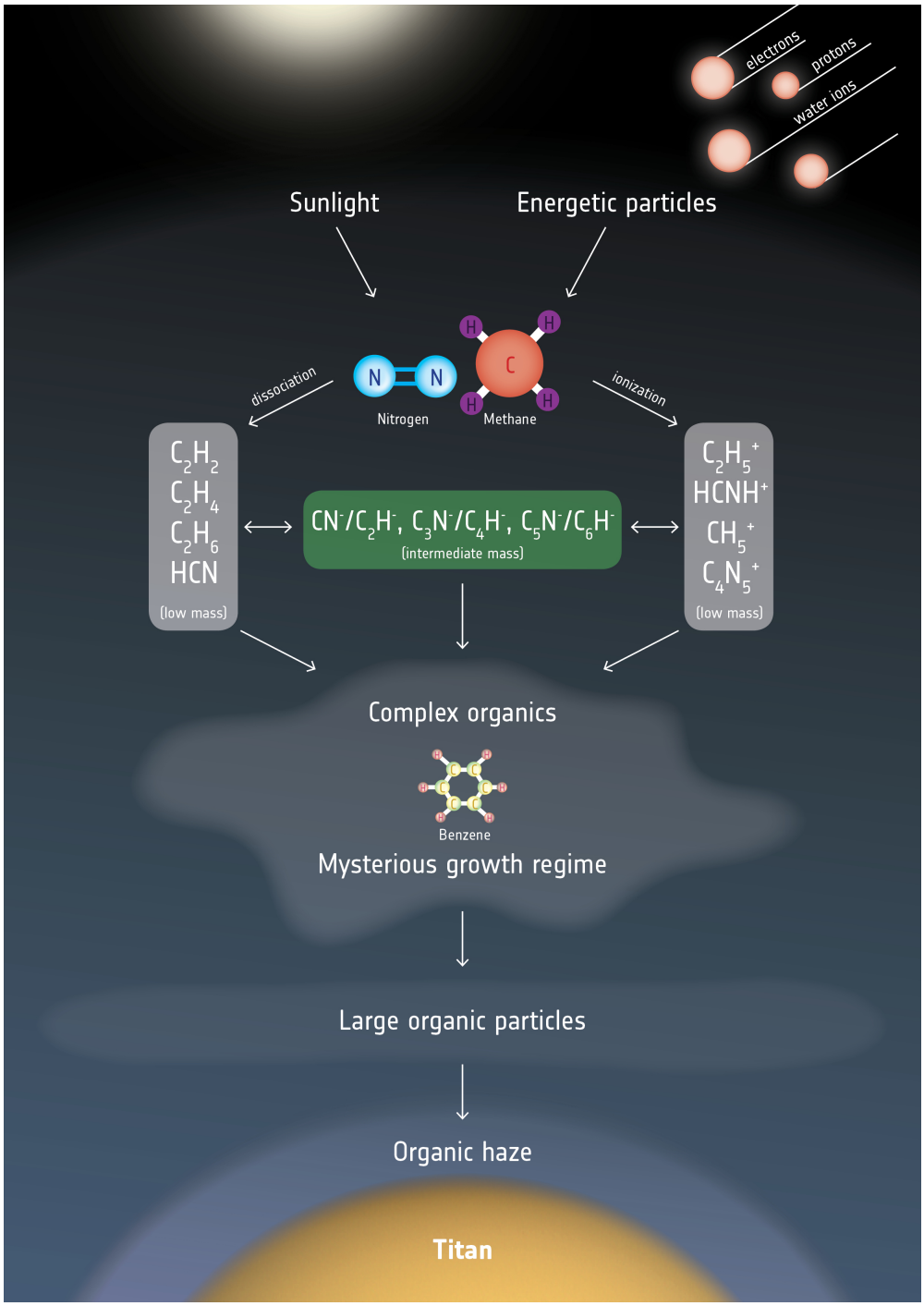

Figure 4.16: Graphic depicting some of the chemical reactions taking place in Titan's atmosphere that lead to the generation of organic haze particles. In the upper atmosphere, the nitrogen and methane are exposed to energy from sunlight and energetic particles in Saturn's magnetosphere. The energy sources drive reactions involving nitrogen, hydrogen and carbon, generating a 'soup' of progressively more complicated compounds. These include the newly identified, negatively charged carbon chain anions (highlighted in the green box), and eventually ring-type molecules such as benzene, although the processes in this region are hard to explore. The carbon chains are thought to be involved in growing bigger and more complex organic molecules that drift down to create Titan's iconic haze, and which are the building blocks towards more complex molecules. This schematic was created by ESA and based, in part, from that presented in *Waite et al.* [2007] to represent these new findings.

is an artefact of the instrument angle response function and must be considered when examining the detections and deriving plasma properties. This phenomenon was not identified prior to this analysis. This findings therefore inform on how electrostatic analysers detect negative ions.

- The spacecraft potential measurements by the RPWS-LP appear different to the spacecraft potential experienced by the CAPS-ELS. This phenomenon was highlighted by [*Jones et al.*, 2009] and herein this concept is further analysed and its impact on the detections assessed. The spacecraft potential appears to significantly affect the arrival angle of the particles as they are detected. Consequently, spacecraft potential values can be determined from examining the mass spectra. The effects of focussing effects on measured plasma distributions is currently completed unconstrained and these results highlight that it is relevant to measuring plasma populations in this environment and might well be in further environments.

- The ΔE/E energy resolution of the instrument was found to smear the detections in energy. An updating fitting procedure is able to better constrain the detections and highlights that the broad mass groups identified by *Wellbrock et al.* [2013] are actually just a function of the instrument response. These broad mass groups are identified as being explained by a single species although further species at nearby mass ranges could also be possible.

- When applying this improved model of the instrument response function to the detections, the first peak ($25.8-26.0$ u/q) and second peak ($49.0-50.1$ u/q) in the anion spectrum were statistically shown to be compatible with the CN^-/C_2H^- and C_3N^-/C_4H^- respectively, although it was not possible to differentiate between these nitrile or hydrocarbon compounds. These species were highlighted by *Vuitton et al.* [2009a, Figure 2 herein], but this was a model based identification and the mass range of peak 3 in particular clearly does not correspond to C_5N^- at 74 u. These study therefore provides quantitative evidence base upon an improved understanding of the instruments response and increased spacecraft potential.

- At altitudes above ∼1200 km the third peak is shown as consistent with the further chain anion C_5N^-/C_6H^- but at lower altitudes becomes dominated by higher mass species not consistent with carbon chain anions. This is at odds with the findings of *Vuitton et al.* [2009a]. This therefore highlights that either species other than C_5N^-/C_6H^- are present,

indeed those carbon chain anions could be rapidly converted into larger species as this is indeed the point where rapid growth occurs. Notably, the mass ranges identified provide evidence for the presence of more complex anions and may well come to represent the first astrophysical detection of anions not composed of linear chains, see recent review by *Millar et al.* [2017]. A number of species were suggested to account for this intermediary peak based upon the relatively better understand cation and neutral chemistry.

- Further persistent detections were also constrained at 117$\pm$3 u/q and 154$\pm$6 u/q and appears to also add to the growing body of evidence for growth processes involving ring structures although the current lack of known reaction pathways impedes their definitive interpretation at present.

- The evolution of the low mass ($<$150 u/q) anions was then examined with respect to the impending growth of the larger organic molecules. Deep within the ionosphere the lower mass anions were observed to become depleted as the larger aerosol precursors coincidentally underwent rapid growth. *Coates et al.* [2009] and *Wellbrock et al.* [2013] analysed the altitudes of peak abundances of the low mass anions and the rapid growth of the larger species. This analysis now finds a correlation between the two, a trend which indeed contributes to the idea that smaller species form the seeds for the larger species via a series of reactions and processes which the chain anions and further intermediary anions appear to be tightly coupled to.

These results demonstrate the importance of tracing a route from small to large species in order to fundamentally understand how complex organic molecules can be produced within a planetary atmosphere.

Chapter 5

Hybrid simulations of positive and negative pickup ions at Europa

The mass loading of space environments through the ionisation of planetary atmospheres is a fundamental process governing the plasma interactions and long term evolution of celestial bodies across the solar system. Regions containing significant pickup ion populations have been observed to exhibit a rich variety of electromagnetic plasma wave phenomena, the characteristics and properties of which can be used to infer the ion species present, their spatial and temporal distributions, and the global ionisation rates of the neutral material. In this study we present hybrid (kinetic ion, massless fluid electron) simulations of ion pickup and Ion Cyclotron (IC) waves observed in the Jovian magnetosphere at the moon Europa. Europa has been identified as the secondary mass loader in the magnetosphere, orbiting within a neutral gas torus at 9.38 Rj. Near Europa, Galileo magnetometer observations displayed bursty IC wave characteristics at the gyrofrequency of a number of species including K^+, O_2^+, Na^+, and Cl^+, indicating the localised pickup of these species. Additional evidence for the presence of Chlorine was the occurrence of both left-hand (LH) and right-hand (RH) polarised transverse wave power near the Cl^+ gyrofrequency, thought to be due to the pickup of both Cl^+ and the easily formed Chlorine anion, Cl^-. To test this hypothesis one-dimensional hybrid (kinetic ion, massless fluid electron) simulations are used to simulate both positive and negative pickup ions and self-consistently reproduce the growth of both LH and RH Alfvén-cyclotron waves in agreement with linear theory. The simultaneous generation of LH and RH waves are shown to result in nongyrotropic ion distributions and increased wave amplitudes, and how even trace quantities of negative pickup ions are able to generate an observable RH signal. Through comparing simulated and observed wave amplitudes,

the first constraints on the densities of Chlorine pickup ions in localised regions at Europa are obtained.

A reduced version of this chapter has been published as an *Journal of Geophysical Research Article* with the citation: Desai. R. T. Cowee, M. M. Wei, H. Fu, X. Gary, S. P. Volwerk, M. Coates, A. J., Hybrid simulations of positively and negatively charged pickup ions and cyclotron wave generation at Europa, *Journal of Geophysical Research: Space Physics*, Vol. 122, Issue 10, p. 408-420.

5.1 Background

The Alfvén-cyclotron instability is driven by a $T_\perp / T_\parallel > 0$ anisotropy in the distribution function of a given ion species, where $\perp$ and $\parallel$ are defined with respect to the ambient magnetic field. Anisotropic ion populations can be created by the ionisation of neutral atoms where the newly formed ions are accelerated or "picked up" by an electric field. The ions are thus energised and, for a sufficiently high plasma beta, generate a number of electromagnetic micro-instabilities and plasma wave phenomena [*Gary and Schriver*, 1987]. Electromagnetic Ion Cyclotron Waves (ICWs) associated with this ion pickup instability have been observed in the solar wind at comets, Mars and Venus [*Thorne and Tsurutani*, 1987; *Barabash et al.*, 1991; *Delva et al.*, 2008], in the Earth's polar wind [*Le et al.*, 2001], and within the Jovian and Kronian magnetospheres [*Kivelson et al.*, 1996; *Leisner et al.*, 2006]. This study reports the first study addressing both positively and negatively charged pickup ions generating the Alfvén-cyclotron instability, with application to the Galilean moon Europa.

Within Jupiter's inner magnetosphere ($<$15 R_J), the magnetic field is approximately dipolar and nominally orientated at right-angles to the sub-Alfvénic rotating magnetodisc. Ions picked up from satellites and rings in this environment will have low velocity components parallel to the magnetic field and form perpendicular rings in velocity space unstable to the generation of left-hand (LH) polarised ICWs [*Wu and Davidson*, 1972]. However, if the newly ionised material has a significant velocity component parallel to the ambient magnetic field, the picked up ions will form ring-beam distributions in velocity space, which results in a Doppler shift to the observed ICW resonant frequencies. In supra-Alfvénic plasma flows such as the Solar Wind, this can cause LH ICWs to be observed as right-hand (RH) polarised in the spacecraft frame [e.g. *Jian et al.*, 2009; *Wicks et al.*, 2016]. It is also possible for obliquely propagating ICWs to become linearly

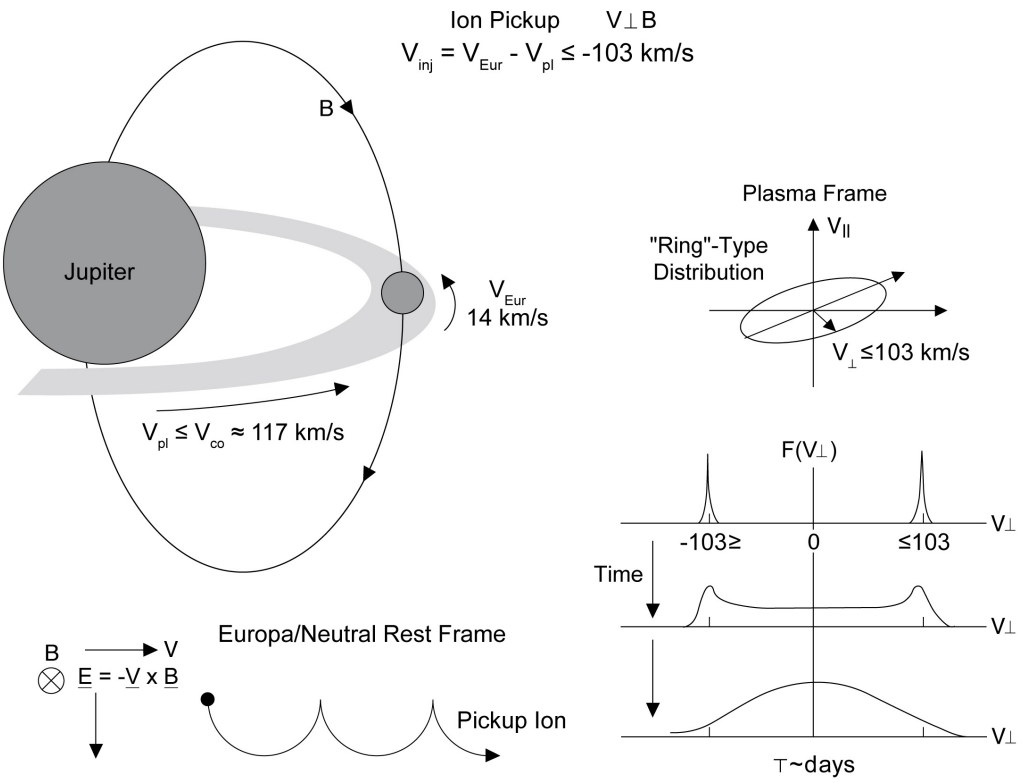

Figure 5.1: Schematic illustration of the pickup geometry for Europan ions, showing the pickup ion cycloidal path in the Europa/neutral rest frame, and velocity-space distributions in the frame of the bulk corotating torus plasma. The plasma flow, v_{pl}, is slowed down in the vicinity of the moon and so will often be less than that of rigid corotation, v_{co}, which results in a variable pickup or injection velocity, v_{inj}. Adapted from *Huddleston et al.* [1998].

polarised and to then reverse polarisation if they attain and pass through the crossover frequency of the multi-component plasma in which they are generated [*Rauch and Roux*, 1982; *Petkaki and Dougherty*, 2001].

These gyroresonant transverse electromagnetic fluctuations have been observed to scatter pickup ion distributions into a bispherical shell distribution and towards thermal equilibrium [*Coates et al.*, 1990; *Tokar et al.*, 2008], with energy distributed between wave growth and ion heating [*Huddleston et al.*, 1998; *Cowee et al.*, 2007].

The moon Europa orbits Jupiter at $\sim$8.8 R_J and has been identified as the secondary mass loading source in the Jovian magnetosphere, contributing an estimated 1-100 kg/s of neutral material [*Kivelson et al.*, 2009; *Shemansky et al.*, 2014]. Galileo's magnetometer recorded a significant amount of plasma wave activity in the vicinity of the moon [*Kurth et al.*, 2001; *Volwerk et al.*,

2001] and, during one upstream encounter and two through the moon's plasma wake, observed bursty ICW characteristics at the gyrofrequencies of a number of species including K^+, Na^+, O_2^+ and Cl^+. A notable trend within this dataset was the occurrence of both LH and RH polarised wave power at the Cl^+ gyrofrequency, a phenomenon absent at the gyrofrequency of other minority species picked up locally at the moon. These observations are shown in Figure **??**. These waves were highly field-aligned and the RH wave power was consequently hypothesised to result from the pickup of both positively and negatively charged Chlorine ions, possible due to the high electron affinity (3.61 eV) and stable configuration of the Chlorine anion, Cl^- [*Volwerk et al.*, 2001; *Kivelson et al.*, 2009].

Negatively charged ions have been observed being picked up from the icy moon Rhea [*Teolis et al.*, 2010], from Saturn's main rings [*Jones and Coates*, 2014], in the Enceladus plumes [*Coates et al.*, 2010], and in Titan's ionosphere [*Coates et al.*, 2007a; *Desai et al.*, 2017a] where the outflow of these species is also predicted [*Ledvina and Brecht*, 2012]. Negatively charged ions have also been observed in abundance at 1P/Halley and 67P/Churymov-Gerasimenko [*Chaizy et al.*, 1991; *Burch et al.*, 2015], and likely form significant plasma populations in the outer solar system where the plasma temperatures are typically lower (lower associative detachment rates) and the solar photon flux is considerably reduced (lower photodetachment rates). The physics of ICWs generated by negatively charged pickup ions has however not been examined. The presence of Chlorine pickup ions at Europa also suggests the moon to be a net source of this species with implications for the abundance of NaCl in the sub-surface ocean.

This work examines the physics of ICWs generated by both positively and negatively charged pickup ions with application to the Europan plasma environment. Section 5.1 describes a self-consistent hybrid simulation approach, which is used to study the growth and non-linear evolution of the modes generated in the plasmas of interest. The analysis first looks to characterise the behaviour of the negative ion ring instability using linear dispersion theory in section 5.3 and hybrid simulations in Section 5.4, which are contrasted to the well known characteristics and properties of the positive ion ring instability. Section 5.5 and 5.6 go on to study scenarios of both instabilities generated within the same system to characterise any interaction between the two and their observable signatures. Section 5.8 then describes a parametric study of the instability saturation energy with ring properties such as density and anisotropy with close reference to the Galileo magnetometer observations.

Table 5.1: Nominal plasma parameters for all simulations runs unless otherwise stated.

j	m_j/m_p	q_j/q_p	$T_\parallel(eV)$	$T_\perp(eV)$	$v_{ring}(kms^{-1})$
Light ion core	8	+1	100	100	-
Cl^- core	35	-1	100	100	-
Cl^+ core	35	+1	100	100	-
Cl^- ring	35	-1	$\sim$0	1830	100
Cl^+ ring	35	+1	$\sim$0	100	100

*B_0 = 400 nT, n_0 = 100/cc, c/ω_{pi} = 134.8 km, $\Omega_i/2\pi$ = 0.17 Hz , c/v_A = 344

5.2 Methodology

Warm plasma dispersion theory and hybrid simulations have previously constrained the behaviour of the Alfvén-cyclotron instability generated by heavy SO_2^+ ion rings in the Io plasma torus [*Huddleston et al.*, 1997, 1998; *Cowee et al.*, 2006], and also for water group pickup ion rings within Saturn's extended neutral cloud [*Leisner et al.*, 2006; *Cowee et al.*, 2009; *Rodríguez-Martínez et al.*, 2010]. This study focuses on the Europan plasma environment and draws comparisons to these studies.

Hybrid codes have successfully reproduced the Alfvén-cyclotron instability for a number of plasma environments [e.g. *Gary et al.*, 1989; *Cowee et al.*, 2006; *Omidi et al.*, 2010]. The code specifies ions kinetically to capture phenomena occurring at ion spatial and temporal scales and approximates electrons as a massless neutralising fluid [*Winske and Omidi*, 1992; *Winske et al.*, 2003]. The simulations consist of one spatial dimension, x, aligned with the ambient magnetic field, $\mathbf{B_0}$, a set-up justified as the main wave power is expected at parallel propagation [*Wu and Davidson*, 1972]. All three components of electromagnetic fields and velocities are resolved to capture the predominantly transverse electromagnetic fluctuations along the y and z axes. The simulations are carried out in the plasma frame with zero-drift velocity and the particle-in-cell simulation technique is employed where all ions are represented by superparticles whose densities and currents are collected on a spatial grid and used as sources to the field equations. Maxwell's equation are implemented in the Darwin limit where the displacement current, $\partial\mathbf{E}/\partial$t, is neglected within Ampére's law to eliminate high-frequency perturbations such as light waves [*Darwin*, 1920]. In these initial value simulations the number of superparticles are specified at the beginning of the run and held as constant, in order to represent an injection of pickup ions from Europa, and particles are initialized with a quiet start configuration to minimize any net currents at the start of the run.

The inputs into the simulation are representative of the general plasma environments around Europa with emphasis on the 11th (E11) and 15th (E15) Galileo encounters. A variety of pickup velocities, from 55-100 km/s, are explored to examine the scaling of the instability with respect to the inherent variations of this parameter due to effects such as: the slow-down of the incident magneto-plasma in front of the moon, the formation of Alfvén wings, pickup ion currents, wake effects and the flapping of the Jovian magnetodisk [*Neubauer*, 1998, 1999; *Khurana et al.*, 1998]. Galileo observed electron densities from 30 cm^{-3} up to several 100 $^{-3}$ during the various encounters, an average ion charge 1.5 q_e and a mean ion mass of 18.5 u with low-charge states of Iogenic sulfur and oxygen dominating [*Kivelson et al.*, 2009; *Bagenal et al.*, 2015]. A nominal ion density of 100/cc and magnetic field of $\mathbf{B_0} = \mathbf{400}$ nT are taken as representative of the Galileo observations during E11 and E15. Further simulation parameters are outlined in Table 5.1, which are used in all runs unless otherwise stated.

The plasma is considered to consist of multiple ion species, either in a zero-drift Maxwellian distribution or a delta-function ring distribution with $T_{\|} \sim 0$. The $\delta\mathbf{E}$ perturbations of the transverse waves act to perpendicularly scatter the ring ions whilst the $\mathbf{v} \times \delta\mathbf{B}$ forces scatters them in the parallel direction. Any other ion population with a similar mass per charge ratio will gyroresonantly interact with these waves and be subject to the same forces and must also be included in the simulations. Ion species with a different mass per charge ratio are not expected to interact with the instability and are represented by a light ion core population to maintain charge neutrality. Each species has mass, m_j, and charge state, q_j, normalised to the proton scale with parallel and perpendicular velocities, $V_{\|j} = (2k_B T_{\|j}/m_j)^{1/2}$ and $V_{\perp j} = (2k_B T_{\perp j}/m_j)^{1/2}$. $V_{\perp}$ is set as the pickup velocity, which is defined as the difference between the near corotational background plasma flow at the orbit of Europa of $\leq$117 km/s and the moon's orbital velocity of $\sim$14 km/s. $V_{\|}$ is set to nearly zero, under the assumption of minimal relative motion between the atmospheric neutrals and the moon.

The temperature anisotropy is defined as $A_j = T_{\perp j}/T_{\|j}$, the Alfvén velocity as $v_A = B_0/\sqrt{\mu_0 n_o m_j}$, the ion gyrofrequency as $\Omega_j = q_j B_0/m_j$, the plasma frequency as $w_{pi}^2 = n_0 q_i^2/\varepsilon_0 m_j$, and the ion parallel plasma beta as $\beta_{\|j} = 2\mu_0 n_0 T_{\|j}/B_0^2$ where the fluid electron beta is equal to the sum of the ion components, $\beta_e = \sum \beta_j$. The subscript p denotes protons, e denotes electrons, and i denotes chlorine ions. The simulation outputs are given in normalised units of the ion Cl^+/Cl^- gyrofrequency Ω_i where $\Omega_i/2\pi$ = 0.17 Hz, the ion inertial length where c/ω_{pi}=134.8 km, and the

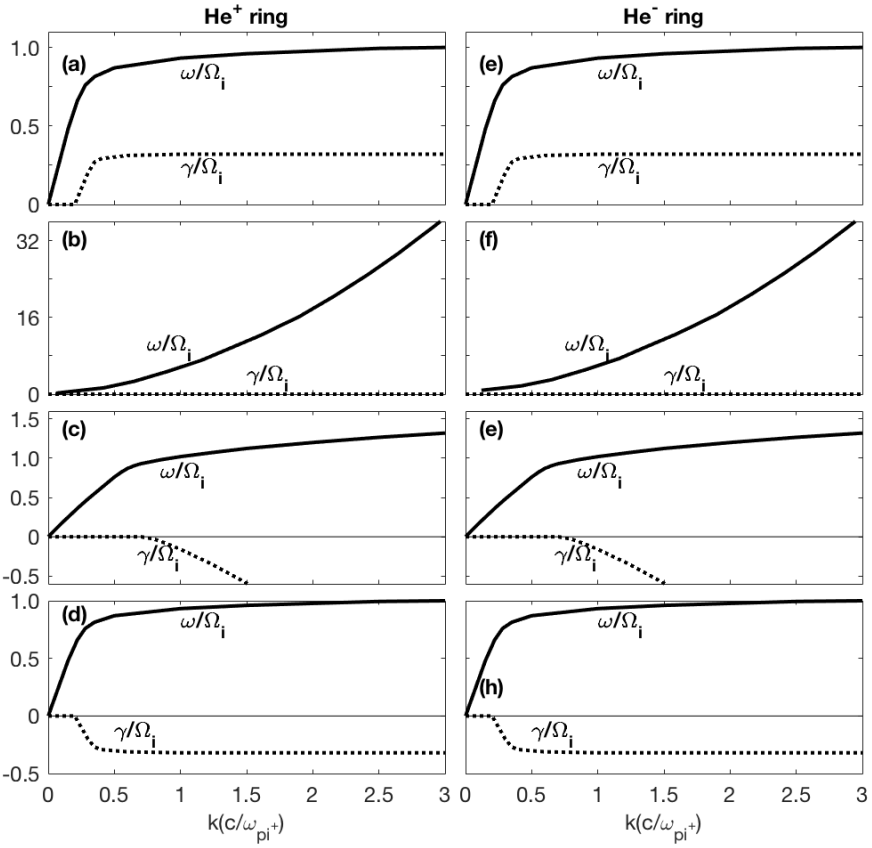

Figure 5.2: Solutions to the kinetic linear dispersion equation for electromagnetic fluctuations at $\mathbf{k} \times \mathbf{B}_o = 0$ in a homogeneous, magnetized, collisionless plasma. There are three components to the plasma: electrons and protons, each with Maxwellian velocity distributions, and a singly charged helium ion or anion component with a cold velocity ring distribution. Here $n_p/n_e = 0.95$ and $n_{He}/n_e = 0.05$. The ring velocity is $v_{ring}/v_A = 0.50$ and the ion beta value (based on the electron density and the proton temperature) is 0.15. The solutions are normalised to the ion gyrofrequency, Ω_i. Panels (a), (b), (c), and (d) show results for He^+ ions, whereas panels (e), (f), (g), and (h) display results for He^- anions. Panels (a) and (e) show dispersion of the unstable left-hand and right-hand Alfvén-cyclotron modes respectively; panels (b) and (f) illustrate dispersion of the stable right-hand polarised magnetosonic waves, panels (c) and (d) represent the stable left-hand polarised stable helium ion cyclotron modes, and panels (g) and (h) illustrate the right-hand polarised stable helium anion cyclotron modes. These solution were calculated by S. Peter Gary.

Alfvén velocity where v_A=147.5 km/s. The simulation domain is 512 c/ω_{pi} in length with 512 grid cells and periodic boundary conditions, and between 50-100 superparticles per cell are used within the various runs. The runs are then stepped forward in time steps of 0.05 ω_{pi}^{-1}, until some time after the instability has reached a quasi-steady saturation energy level.

Table 5.2: Case-study simulations for Runs I, II, III and IV described in the text. Further plasma input parameters are given in Table 5.1.

Run			Run		(both)	(Cl^+)	(Cl^-)
	Components	n_i (1/cc)		Components		n_i (1/cc)	
I	Light ion core	80	III	Light ion core	98	98.5	99.5
	Cl^- core	15		Cl^+ ring	1.5	1.5	-
	Cl^- ring	5		Cl^- ring	0.5	-	0.5
II	Light ion core	60	IV	Light ion core	98	98.1	99.9
	Cl^+ core	15		Cl^+ ring	1.9	1.9	-
	Cl^- core	15		Cl^- ring	0.1	-	0.1
	Cl^+ ring	5					
	Cl^- ring	5					

5.3 Linear Dispersion Theory

Figure 5.2 illustrates solutions to the kinetic linear dispersion equation for electromagnetic fluctuations at $\mathbf{k} \times \mathbf{B}_o = 0$ in a homogeneous, magnetized, collisionless plasma with three components: electrons and protons, each with Maxwellian velocity distributions, and a singly charged helium ion or anion component with a cold velocity ring distribution (e.g., see *Gary and Madland* [1988] with $\alpha = 90^o$). The pickup or ring velocity to Alfvén velocity ratio is specified as $\mathbf{v_r/v_A} = \mathbf{0.5}$ and the parallel plasma beta as $\beta_{||} = 0.15$. These are in the range of observed values, with variations around these parameter not significantly altering the calculated solutions. Although the simulations described in subsequent sections address much heavier ions, the qualitative features of the various modes shown here should be similar to those of the simulations.

Plasma parameters used in Figure 5.2 are given in the figure caption. The complex frequency is $\omega = \omega_r + i\gamma$ with positive γ corresponding to fluctuation growth. The left-hand column shows results for an He^+ ion velocity ring, whereas the right-hand column illustrates results for an He^- anion velocity ring. In both cases the dispersion equation yields four distinct modes near or below the cyclotron frequency with both positive and negative helicities. Magnetic helicity defines the sense of the spatial rotation of the fluctuating field vectors with respect to the wavevector, $\mathbf{k}$, at a given instance and is independent of the reference frame of the observer [*Gary*, 1993]. A positive helicity corresponds to either a forward propagating RH wave or a backwards propagating LH wave and a negative helicity corresponds to either a backwards propagating RH or forwards propagating LH wave.

The fastest growing modes in both cases are the cyclotron-resonant modes shown in panels (a) and (e). The figure suggests that these two modes are unstable to arbitrarily short wavelengths,

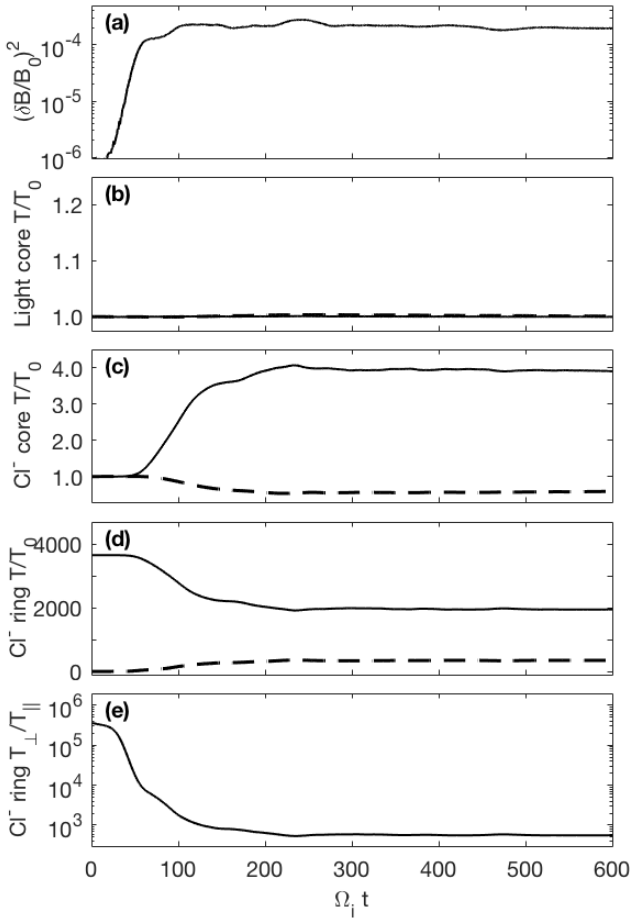

Figure 5.3: Time histories from Run I which includes light ion core, Cl^- core and Cl^- ring ion components. (a) Shows the fluctuating magnetic field energy density, (b-d) shows the perpendicular (solid line) and parallel (dashed line) temperature histories of the different components, and (e) shows the anisotropy of the ring-ions. Input parameters are provided in Table 5.1 and Table 5.2.

however, for the more realistic case of a warm ring ($T_{||} > 0$) ion cyclotron resonances will damp modes at short wavelengths (e.g., Fig. 2 of *Gary and Madland* [1988]) so that we expect maximum growth to arise near kc/ω_{pi}. In addition to these, panels (b) and (f) show the right-handed magnetosonic-whistler mode that is undamped, and panels (c-d) and (g-h) show the $\omega_r \sim \Omega_i$ ring modes, one weakly stable and one weakly damped.

5.4 Negatively charged ring instability

In simulation Run I, the instability is simulated with negatively charged Cl ions. As outlined in Table 5.2, a cold Cl^- ring distribution is initialised with negligible temperature spread parallel to the magnetic field together with a thermalised Cl^- core population. A further positively charged Maxwellian light ion core represents the ambient low-charge state oxygen and sulphur

Table 5.3: Parametric study of the scaling of the Chlorine ion ring instability in the low density regime applicable to the Galileo E11 and E15 encounters with Europa. The parameter n_r represents the ring ion density and n_0 represents the total Chlorine ion density. Further plasma parameters are given in Table 5.1.

Components	Density (1/cc)	n_r/n_0	Pickup velocity (km/s)
Light ion core	95	-	-
Cl^+/Cl^- core	0, 1.9-0.1	-	-
Cl^+/Cl^- ring	0.1-2, 0.1-1.9	0.05, 1	55, 100

background ions of the Jovian magnetodisk. This background population was initially specified as protons although a higher mass ion was later used so that larger timesteps could be taken whilst not affecting the growth of the instability and still accurately resolving the ion gyro-motion. Figure 5.3 shows the fluctuating magnetic field energy density, $(\delta B/B_0)^2$, and temperature evolution of the different species. The instability initially grows rapidly until $\Omega_i t$ =60-70, then grows more slowly until $\Omega_i t = 110 - 120$ where a quasi-steady level of $(\delta B/B_0)^2 = \sim 2.7 \times 10^{-4}$ is reached.

The fluctuations shown in Figure 5.3a act to pitch-angle scatter the anisotropic Cl^- ring distribution toward isotropy as shown in Figure 5.3c-e. The Cl^- core population acts to damp the growth of the waves and is consequently heated in the perpendicular direction, whilst the light ion core remains at a constant temperature as anticipated for components not resonantly interacting with the instability.

The particle positions in velocity space are displayed in Figure 5.4 at two different times during the simulation. At $\Omega_i t = 27$ the Cl^- ring distribution still resembles its initial state, although some scattering has occurred. At time $\Omega_i t = 81$, the fast growth phase has ended and the bulk ring velocity has significantly decreased as particles diffuse in energy and scatter into a bispherical distribution along characteristic energy surfaces prescribed by the perpendicular pickup ion velocity, v_p, and ICW phase velocity, v_{ph}, where $v_{ph}^2 + v_p^2$ is constant [*Huddleston and Johnstone*, 1992]. The heating of the core Cl^- ions in the perpendicular direction is most evident in Figures 5.4e and 5.4f.

Figure 5.5 shows the ω-k spectrum during the growth phase of the instability. The wave power grows out of the Alfvén branch and is concentrated near the Chlorine cyclotron frequency with the bulk wave power occurring between kc/ω_{pi}=1-2. This agrees with the dispersion relations given in Figure 5.2 where positive growth rates and similar frequencies are predicted at $kc/\omega_{pi} \geq 1$. The dynamic spectrum in Figure 5.5 shows the Power Spectral Density (PSD) of Run

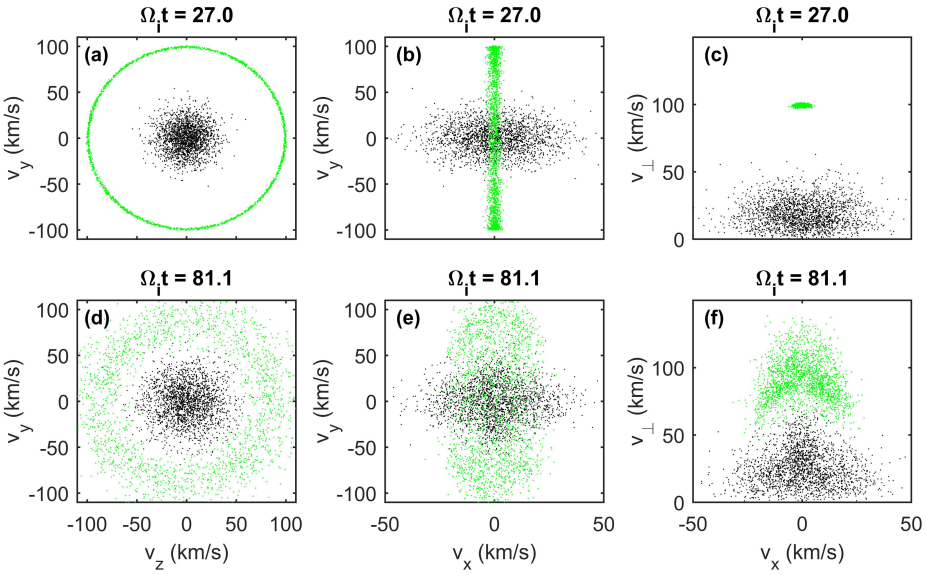

Figure 5.4: Run I velocity space distributions of the ring and core Cl^- ions at two different times. The ring ions (green) scatter from a ring distribution towards a bispherical shell distribution as the core ions (black) are heated in the perpendicular direction. The light ion core is not shown.

I and the magnetic ellipticity as calculated by the UCLA X-waves analysis tool, which utilises the inherently antisymmetric quadrature spectral matrix to provide information on the propagation direction and thus polarisation of separated circularly polarised wave components [*Means*, 1972]. In the case of parallel and anti-parallel propagating waves, or in the case of superimposed wave packets with different polarisations, this technique will return the net resultant ellipticity.

This was generated using a time series determined from one grid cell in the simulation and while other grid cells may yield slightly different results, the simulation conditions are initially uniform and so significant differences between cells are not expected. The wave power occurs at the Chlorine gyrofrequency as in Figure 5.5 but decreases slightly in frequency over time as a result of an inverse cascade to longer wavelengths [*Gary and Madland*, 1988]. The variability in the wave power is due to the superposition of a range of modes excited in the simulation. The resultant ellipticities appear close to $+1$, indicating a RH near-circularly polarised wave near the Chlorine gyrofrequency as predicted by the positive helicity mode in Figure 5.2.

To examine the scaling of the saturation energy of the RH instability, the ring anisotropy and density are varied across the parameter space outlined in Study A in Table 5.3. Linear theory predicts the growth rate of the ion cyclotron instability is proportional to the ring velocity and increases as the ring-to-core relative density increases [*Huddleston et al.*, 1997]. Larger amplitude

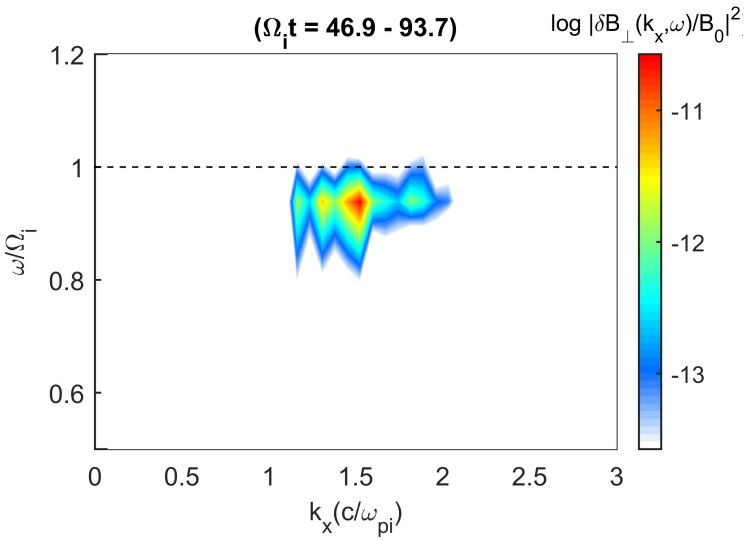

Figure 5.5: Frequency-wavenumber spectrum of the transverse wave power from Run I, which includes light ion core, Cl^- core and Cl^- ring ion components Waves propagate in both directions with the same spectral properties. The wave power is seen near the Cl^- gyrofrequency (dashed line) and at normalised wave numbers between 1 and 2. The spectrum is calculated using a Fourier window over $46.9 < \Omega_i t < 93.7$.

waves are therefore generated due to the increased amount of free energy available, although linear theory is unable to predict at what amplitudes the instability will saturate. Previous studies have however constrained the relationship between saturation amplitudes and ring density and anisotropy [e.g. *Huddleston and Johnstone*, 1992; *Cowee et al.*, 2006; *Fu et al.*, 2016], which is well reproduced in Figure 5.7 for the negative ion ring instability when relating the varying ring energy to the saturation energy levels, $(\delta B/B_0)^2$. This and the further scaling study in Section 5.7 are also important for characterising the pickup of low density minority ion species applicable to the Galileo observations of interest where the instability is only weakly unstable.

The results of the negative ion ring instability presented in Figures 5.3-5.6 show that a negatively charged ring generates a RH instability in-line with the predictions of linear theory and is analogous to that of the LH instability studied in *Huddleston et al.* [1997] and *Cowee et al.* [2006].

5.5 Simultaneous pickup of positive & negative ions

This section examines the co-generation and interaction of both positive (LH) and negative (RH) Alfvén-cyclotron instabilities within the same system. To explore these effects Run II contains equal quantities of Cl^+ and Cl^- ring and core ions as outlined in Table 5.2. This results in twice the amount of free energy available to drive wave growth and, in the absence of interactions

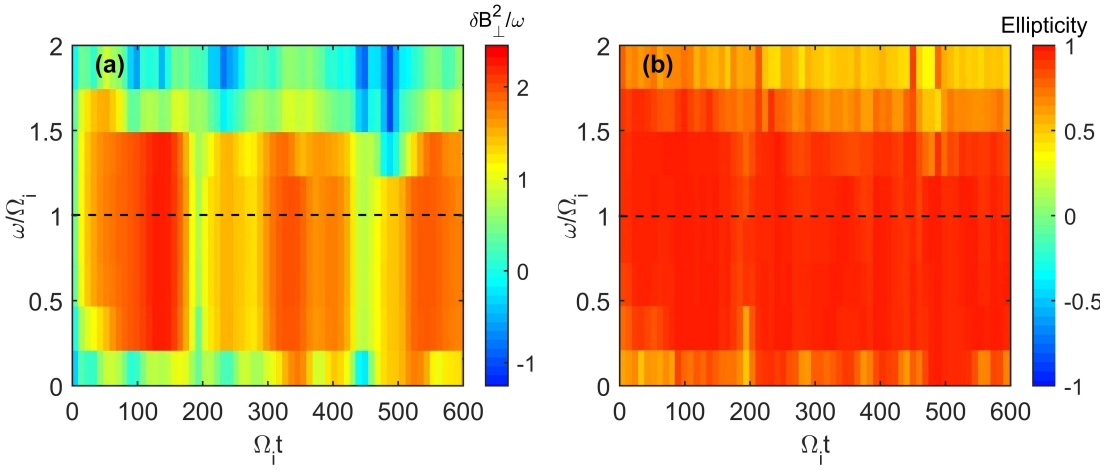

Figure 5.6: Run I dynamic spectrum of (a) transverse Power Spectral Density near the Cl^- gyrofrequency (dashed line) and (b) magnetic polarisation. The corresponding magnetic polarisation in (b) is close to +1 indicating RH polarised wave power.

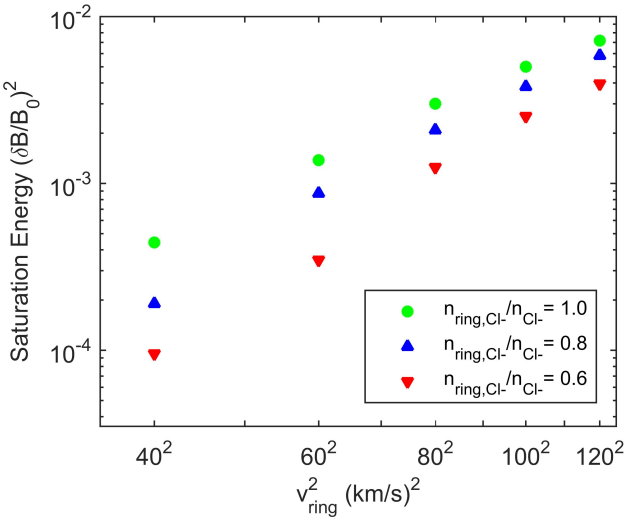

Figure 5.7: Saturation wave energies for ring velocities of 40 to 120km/s for ring-to-total Cl density ratios of 1.0, 0.8, and 0.6. Input parameters are provided in Table 5.3. The scaling of the negative ion instability follows the same trends that of those of pickup of heavy SO_2^+ in the Io plasma torus [e.g. *Cowee et al.*, 2006].

between the two rings, the saturation energy should reach double that of Run I (Figure 5.3a) where only the negative ring ions are initialised. To simplify the physics of these scenarios these runs do not include core $Cl^{+/-}$ components.

Figure 5.8 shows the fluctuating magnetic field energy density growing as anticipated although in this instance intense high frequency perturbations are apparent. These oscillations cause the magnetic field energy density, $(\delta B/B_0)^2$, to reach levels of up to four times that of

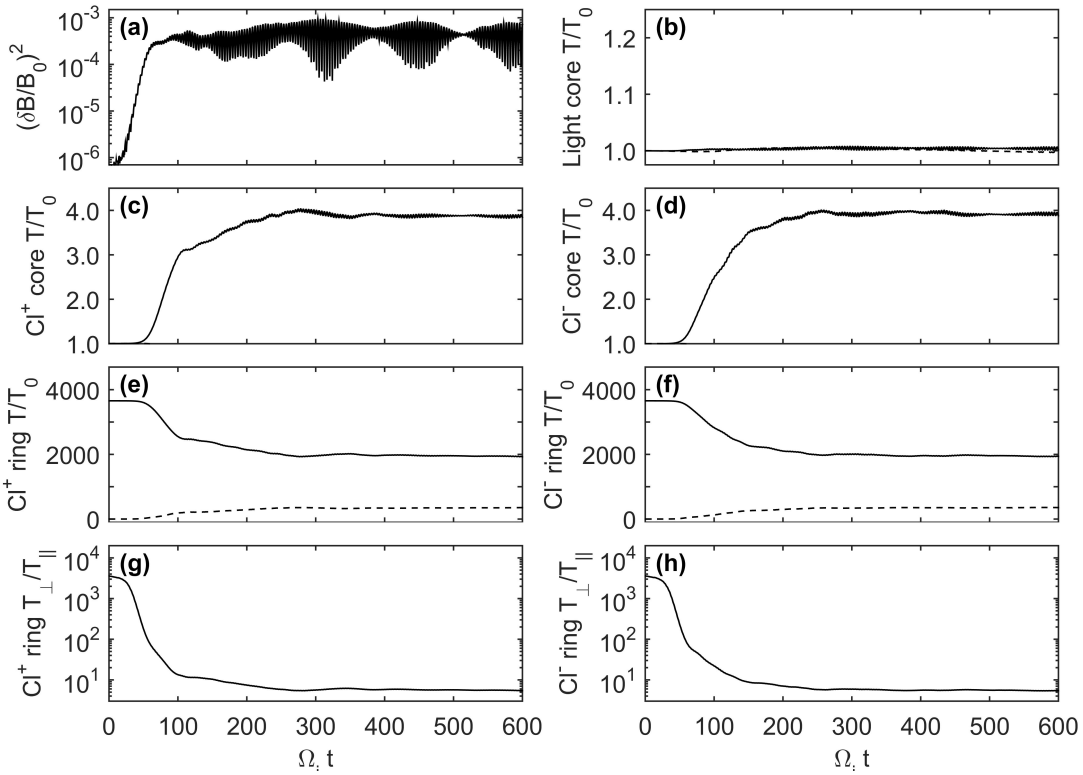

Figure 5.8: Time histories from Run II which includes a light ion core, Cl^- and Cl^+ ion cores as well as Cl^+ and Cl^- ring ion components. (a) Shows the fluctuating magnetic field energy density, (b-f) shows the perpendicular (solid line) and parallel (dashed line) temperature history of the different components, and (g-h) show the anisotropy of the positive and negative ring-ions respectively. Input parameters are given in Table 5.1 and Table 5.2.

Run I, although a running average produces the anticipated saturation energy level of $(\delta B/B_0)^2 = \sim 5.4\times10^{-4}$ (twice that of Figure 5.3a). These high-frequency oscillations occur at a frequency of approximately twice the Chlorine ion gyrofrequency although the intensity also changes in a further beating pattern along a time scale of $\Omega_i t = 25 - 50$ indicating the superposition of multiple modes. The high frequency oscillations are also apparent in the temperature histories of the Chlorine core components and to a lesser extent in the non-resonant light ion core, suggesting this phenomenon may have an electrostatic component. To further examine this behaviour the phase space angular distributions of the different components are plotted in Figure 5.9. Here, both the Cl^+ and Cl^- core and ring components can be seen to be highly bunched in gyrophase space with particles clustered around common positions whilst gyrating about B_0.

Non-gyrotropic ion distributions have been observed at Comet 26P/Grigg-Skjellerup [*Coates et al.*, 1993] and in the distant Earth's magnetotail [*Saito et al.*, 1994]. Subsequent studies on these determined that increasing the non-gyrotropy of anisotropic ion distributions resulted in increased

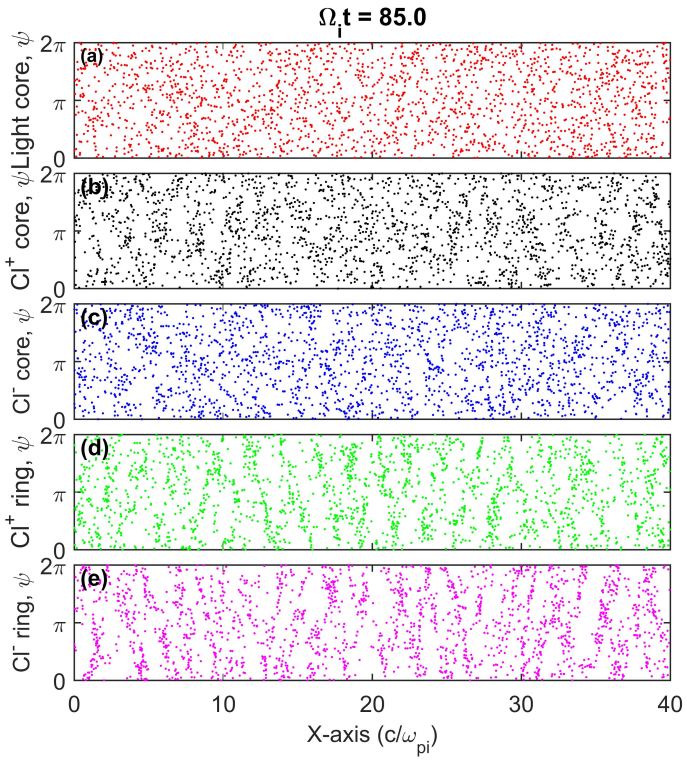

Figure 5.9: Run II plasma component distributions relative to their gyrophase angle, ψ, at $\Omega_i t = 85.0$. Bunching is present in in all four Chlorine ion components due to counter-propagating ICWs.

instability growth rates and a larger range of excited wave numbers [*Brinca et al.*, 1993; *Convery et al.*, 2002]. These studies also show, using hybrid simulations, how non-gyrotropic ring distributions result in large magnetic oscillations as energy is exchanged between the waves and the time-varying bunched ion distributions. These effects appear analogous to what is seen in Run II although in this study the ions are initialised in a gyrotropic state and develop their nongyrotropy as the simulation progresses. Density oscillations at half the wavelength of the ICW mode have previously been observed in simulations of anisotropic ring current ions in the Earth's magnetosphere [*Omidi et al.*, 2010]. These were attributed to develop from oppositely directed ICWs intersecting one another twice within each full wave rotation and introducing periodic effects at twice the resonant wave frequency. This caused the core ions to become bunched in gyrospace as seen in Run II although a significant associated electrostatic periodicity was also reported which is not observed in this study.

The half-length oscillatory behaviour seen in Run II also appears significantly greater than that reported in *Omidi et al.* [2010], presumably due to the presence of both LH and RH waves acting to bunch both positively and negatively charged core components. The co-generation of

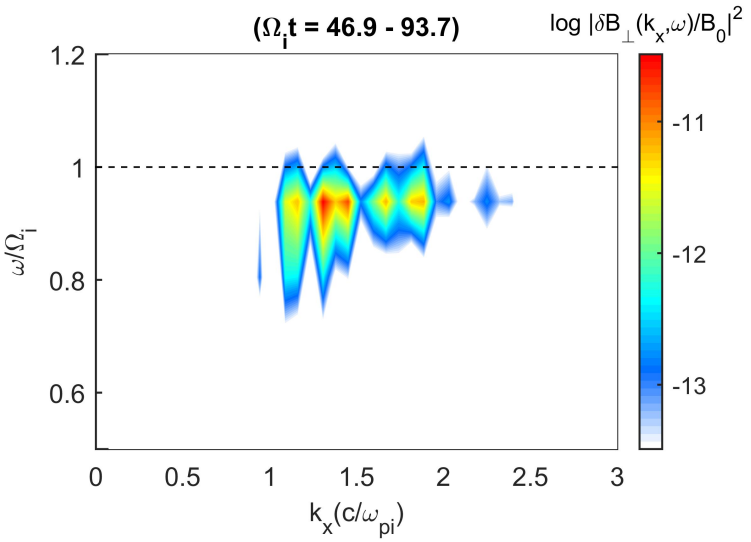

Figure 5.10: Run II frequency-wave number spectrum of the transverse wave power where equal quantities of positive and negative-ring ions are included. Waves propagate in both directions with the same spectral properties near the Cl^- gyrofrequency (dashed line) at normalised wave numbers between 1 and 2. The spectrum is calculated using a Fourier window over $46.9 < \Omega_i t < 93.7$.

the LH and RH instabilities could also introduce multiple half-length modes which will naturally vary over time moving in and out of phase and could explain the large variations in intensity.

Figure 5.10 displays the ω-k spectrum for Run II and shows that the wave power is spread over wave numbers and frequencies similar to those of Run 1 (Figure 5.3a), although in this instance there is increased wave power due to double the density of ring ions included. The dynamic spectra in Figure 5.11 also shows the wave power appearing at and just below the Chlorine ion gyrofrequency. The wave power however displays no clear circular polarisation with ellipticity values sometimes displaying positive or negative values. This effective near linear polarisation agrees with the theoretical expectation of the summation of LH and RH circularly polarised waves at similar frequencies and wave numbers. The variability in the polarisation is attributed to the time-dependent fluctuating wave amplitudes, frequencies and wave numbers for each instability, which allows either the LH or the RH mode to appear dominant for short intervals. This effect could also be amplified as a result of the gyrophase bunching.

5.6 The magnetic signature of negative ion pickup

This section describes an ensemble of simulations, which further characterise the interaction and scaling of the two instabilities and explore how a trace negative ion population is able

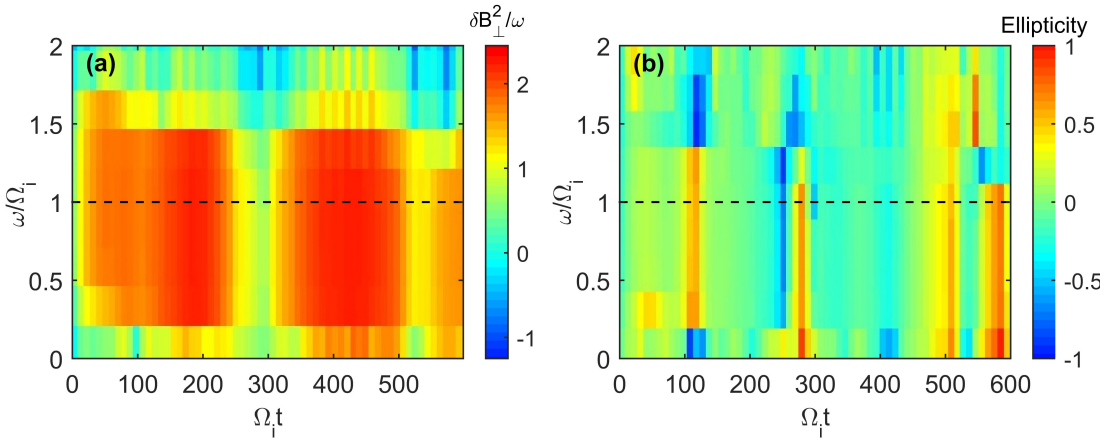

Figure 5.11: Run II dynamic spectrum for both the Cl^+ and Cl^- instabilities. (a) shows the transverse Power Spectral Density and (b) magnetic polarisation, near the Chlorine ion gyrofrequency (dashed black line). The wave power is observed in the same regions as in Figure 5.10 and the magnetic polarisation is approximately linear as anticipated from the summation of the LH and RH near-circularly polarised components although periods of both LH and RH polarisations are present.

to generate an observable signal. These runs cover a wide range of Cl^+ and Cl^- densities and two specific runs are chosen, termed Run III and Run IV in this chapter, to illustrate the key findings. Run III and Run IV nominally contain a 3:1 and 19:1 Cl^+:Cl^- pickup ion density ratio respectively, as outlined in Table 5.2. Figure 5.12 shows the fluctuating magnetic field energy density and temperatures of the various components for both Run III and Run IV. Figure 5.13 shows the magnetic polarisations and Figure 5.14 shows the ω-k spectrum.

In Run III and IV the Cl^+ instability has an increased growth rate and wave amplitudes compared with the significantly reduced Cl^- instability and the sum of the LH and RH instabilities are in good agreement with the amplitudes produced when both components are included. In ω-k space the LH and RH instabilities appear as distinct pockets of wave power at different wave numbers. The wave power still occurs near the Chlorine ion gyrofrequency but the Cl^- instabilities are excited at slightly different frequencies to the Cl^+ instabilities in both instances.

During Run III the magnetic polarisation near the Chlorine ion gyrofrequency is predominantly LH polarised although, at $\Omega_i t = 200$, when the weaker Cl^- RH instability amplitudes become comparable and briefly exceed those of the Cl^+ LH instability, a polarisation reversal occurs and ICW power becomes predominantly RH polarised before returning to a LH polarisation. In Run IV however, despite the Cl^- wave amplitudes never exceeding those generated by the Cl^+ ring, a polarisation reversal is surprisingly also present and a brief burst of RH polarised wave

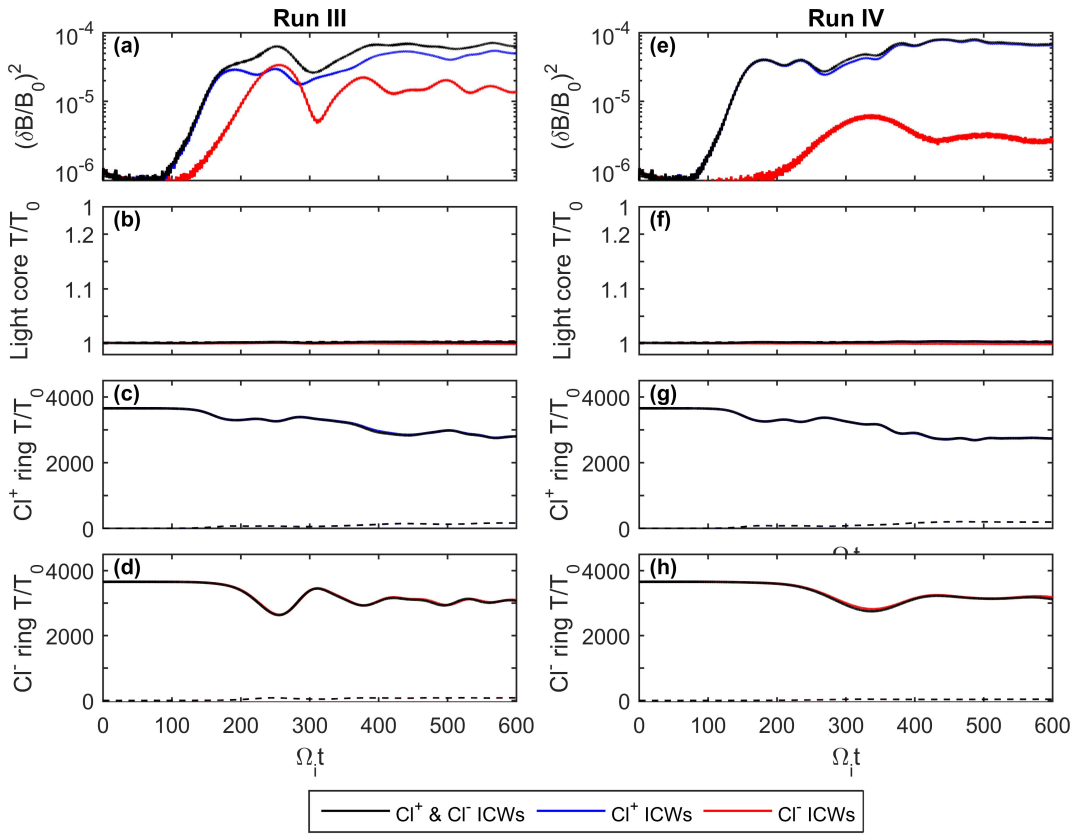

Figure 5.12: Time history for Run III and Run IV. (a) and (d) shows the fluctuating magnetic field energy densities, and (b-c) and (e-f) shows the ring and core perpendicular (solid line) and parallel (dashed line) temperatures. The black line shows the Cl^+ and Cl^- instabilities simulated together, the blue line the Cl^+ instability and the red line the Cl^- instability. The input parameters are given in Table 5.1.

power results at $\Omega_i t = 250$. This phenomenon is attributed to the two instabilities having different growth rates and generating wave power at different wave-lengths and frequencies. The ω-k spectrum indicates that during this brief instance of a RH dominated spectrum, the RH wave power is generated very close to the Chlorine ion gyrofrequency whereas the LH instability saturates earlier and although possessing more wave power, this wave power is spread across a wider range of wave numbers and centres at a lower frequency. This effect means that despite the reduced growth rate of the Cl^- instability, the wave power is still able to generate an observable RH signal as a result of the natural time-dependent variability of the wave amplitudes.

The high-frequency oscillatory behaviour is also reduced in Runs III and even more so in Run IV, presumably due to the LH and RH components occurring at different wave numbers. This suggests that this half-length mode is also more strongly driven when LH and RH ICWs of a

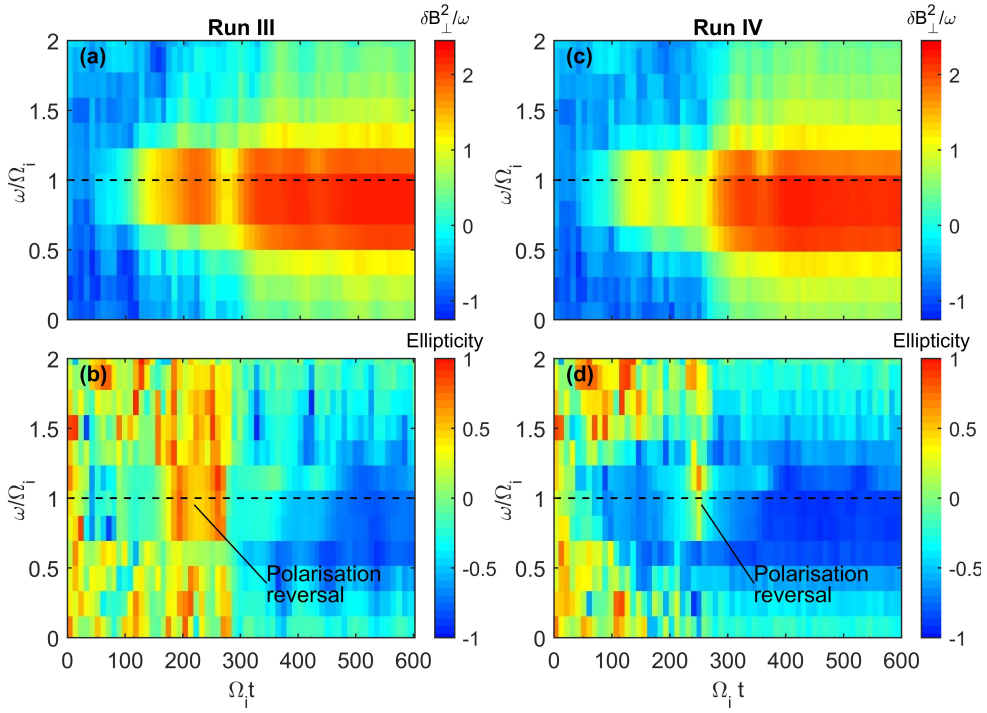

Figure 5.13: Run III and Run IV dynamic spectra. (a) and (c) shows the transverse Power Spectral Density and (b) and (d) shows the magnetic polarisation. The wave power is observed near the ion gyrofrequency (dashed black line) and several polarisation reversals result in LH and RH wave power in either case. Each spectrum was calculated using a 32 point Fourier window.

similar wave number and frequency are present.

The results obtained from Runs III and Run IV demonstrate how positive and negative ring instabilities, although similar in nature, can have different spectral properties as a result of differences in the initial ion distribution functions. The simulations thus show how the appearance of RH wave power within a predominantly LH signal, as was observed by Galileo, can be evidence of negatively charged pickup ions generating a RH Alfvén-cyclotron instability. The simulations also indicate how an inherent polarisation variability will be present in systems containing instabilities driven by both positive and negative ion rings.

5.7 Application to Europa

To better understand the processes occurring at Europa, the simulated waves are compared to the ICWs observed by Galileo. The dominant pickup ion at Europa is O_2^+ produced from the moon's oxygen-based exosphere [*Hall et al.*, 1995; *Johnson et al.*, 2009], but large con-

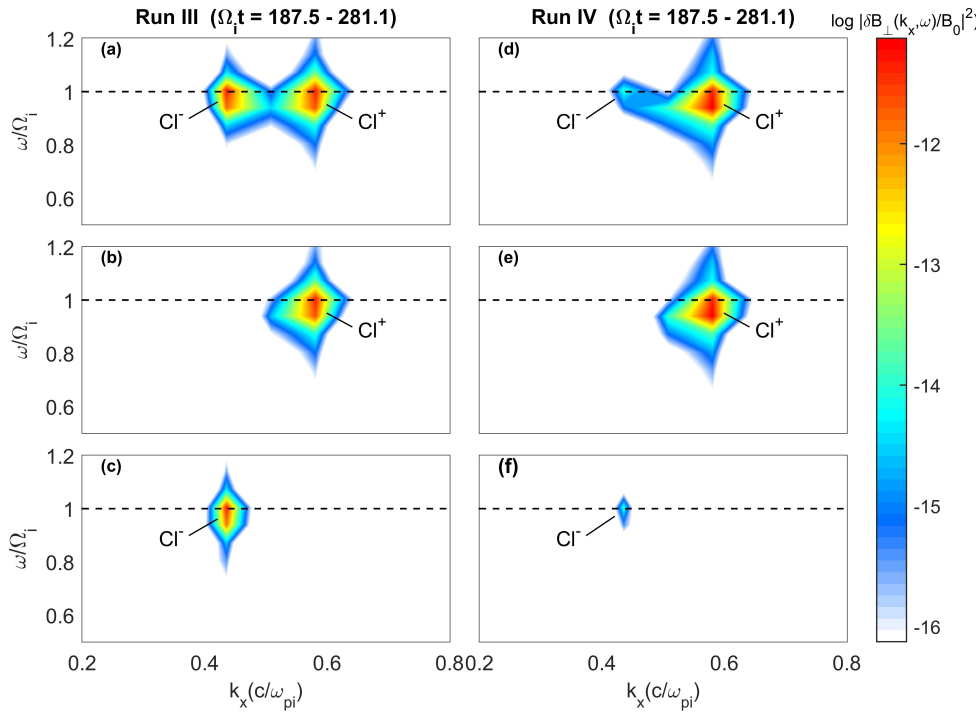

Figure 5.14: Run III and Run IV frequency-wave number spectrum near the $Cl^{+/-}$ gyrofrequency (dashed black line). (a) and (b) show both the Cl^{+} and Cl^{-} instabilities simulated together, (b) and (d) shows the Cl^{+} instability and (c) and (f) show the Cl^{-} instability. Each spectrum was calculated with a Fourier window is 93.6 $\Omega_i t$.

centrations of thermalised S^{+} ions originating from Io have a similar mass per charge ratio and resonantly interact to damp the growth of waves near the O_2^{+} gyrofrequency. Consequently O_2^{+} ICWs are not observed in significant quantities and during the E11 encounter these waves appear to be generated in a higher frequency band to those concentrated near the $Cl^{+/-}$ gyrofrequency [*Volwerk et al.*, 2001]. During E15 however it is however difficult to rule out contribution to the LH wave power from ICWs generated by the pickup of O_2^{+}.

The E11 and E15 observations of wave power at the Chlorine gyrofrequency occurred between 3-4 Europa Radii (R_{Eur} ~1561 km) downstream of the moon [*Volwerk et al.*, 2001]. The simulation results presented in Runs I-IV, show that for the various densities examined, the instability saturates within 200 - 320 Ω^{-1}, which, in the plasma frame, corresponds to a convection distance of < 1 R_{Eur}. The simulations therefore suggest that the Cl^{+} and Cl^{-} ring instabilities would likely have reached saturation when observed by Galileo, if the ions were picked up close to the moon.

To relate possible source densities to the Galileo observations, a parametric study of the

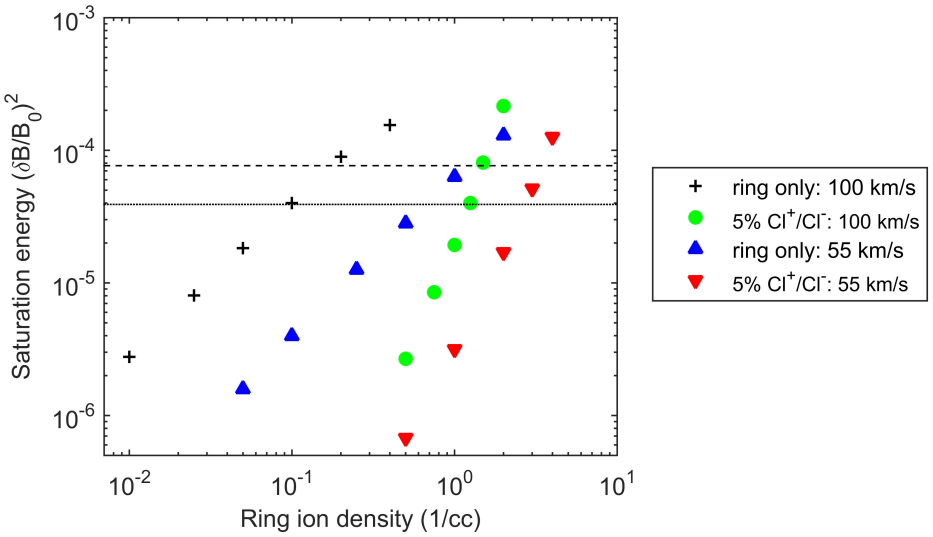

Figure 5.15: Parameter space for the limiting cases of 100km/s (magenta) and 55km/s (cyan) pickup velocities. These two cases are simulated with a 5% total ring+core $Cl^{+/-}$ ion density (circles) and with zero core damping (squares). The Cl^{+} and Cl^{-} instabilities have equivalent properties as shown in Section 5.4 The Galileo maximum wave amplitudes during E11 (dashed line) and E15 (finely dotted line) are overlaid. The input parameters are provided in Tables 5.1 and 5.3.

Alfvén-cyclotron instability is carried out for magnetic field fluctuations in the range observed by Galileo, see Table 5.3. During the E11 and E15 encounters the wave amplitudes at the $Cl^{+/-}$ gyrofrequency reached absolute values of 2.5 nT, $(\delta B/B_0)^2 = 3.9 \times 10^{-5}$, and 3.5 nT, $(\delta B/B_0)^2 = 7.7 \times 10^{-5}$, respectively, The wave saturation amplitude is necessarily dependent on the background density of $Cl^{+/-}$ ions, which will act to damp the growth of the instability. In Figure 5.15 the ring ion densities are plotted against saturated amplitude for the two limiting cases of a varying core population where the Chlorine ring and core ion densities sum to 5%, and for zero core damping. The amplitude modulations brought upon by gyrophase bunching are not included in the saturation amplitudes as a running average was used. This could complicate the direct interpretation of the wave amplitudes and introduce a factor of 2 additional uncertainty. The pickup or ring velocity is also varied across the anticipated range observed near the moon [*Kivelson et al.*, 2009], although during E11 and E15 this was in the upper end of this range [*Volwerk et al.*, 2001].

From this parameter space the Cl^{+} and Cl^{-} total maximum densities are constrained to a range of $0.1 - 1.5/cc$ required to produce the 2.5 and 3.5 nT peak values observed during the E11 and E15 Galileo flybys through Europa's wake. This spread is dependent on the unknown background Chlorine ion density and exact pickup velocity. Cl^{+} densities have been placed at between $1 - 2.5\%$ of the Io plasma torus [*Küppers and Schneider*, 2000; *Feldman et al.*, 2001]

and highlighted as plausibly present in neutral, negatively and multiply charged states, as well as produced from Io within compounds such as $FeCl_2$, CuCl, $ZnCl_2$, NaCl, KCl and $MgCl_2$ [*Fegley and Zolotov*, 2000; *Brown and Hand*, 2013]. These compounds will diffuse outwards towards Europa and likely become implanted within the surface ice before being sputtered into the near-Europa plasma environment and torus, in addition to any local source. Cl^+ and Cl^- ions produced locally at Europa would also contribute to the Europan torus, and may also contribute to wave damping. The chemical pathways describing the Cl^+ and Cl^- production and loss processes are however beyond the scope of this analysis and the results are parametrized with respect to the unknown background Chlorine ion densities. It should therefore be noted however how important it is to constrain the Iogenic material diffusing outwards in Jupiter's magnetosphere to understand processes occurring locally at Europa.

The upper limits on the inferred peak Cl^+ and Cl^- pickup densities appear high for a sputtered minority species ultimately derived from Io. NaCl has however been suggested to be abundant within Europa's sub-surface ocean [*Kivelson et al.*, 2000; *Zimmer et al.*, 2000] and could therefore feasibly be present in significant quantities within the Europan ice and plumes. A recent study by *Hand and Carlson* [2015] also suggest that the characteristic brownish streaks on the moon's surface are composed of high quantities of heavily irradiated NaCl, discoloured as a result of the intense $>$500 kRad Europan radiation environment. A Na cloud has also been observed to envelope the moon and, although Na can be produced through other processes as observed at Mercury [*McGrath et al.*, 1986], significant quantities of Cl ions in localised regions is not inconsistent with physical processes inferred to be occurring at the moon. The results indeed provide evidence that Europa is a local source of Chlorine ions.

The LH and RH Galileo wave observations are too brief to directly establish the respective amplitudes for the positive and negative ion instabilities. To interpret these further, *Kivelson et al.* [2009] show the magnetic field rotations using 15 second hodograms, indicating the RH wave power is detected over the order of this time period. For the parameter space explored, the dynamic spectra showed evidence of both LH and RH polarisations for density ratios as low as 1:19 Cl^-:Cl^+. Below this lower limit of $\sim$5% the Cl^- instability was not sufficiently strong to produce a polarisation reversal.

5.8 Summary & Conclusions

This study used a hybrid simulation technique to characterise the physics of ICWs generated by anisotropic distributions of positive and negative pickup ions. These simulations have verified the predictions of linear dispersion theory and were used in this study to relate the wave amplitudes and wave polarisations to local ion populations. Through the characterisation of the negative ion ring driven instability and the simultaneous generation of the positive and negative ring instabilities within the same system, the following were concluded:

- A negatively charged pickup ion ring will generate near circularly polarised RH waves consistent with theoretical predictions.
- The RH ring-instability behaves analogously to the LH ring-instability with respect to the resonant frequencies, wave numbers excited and interactions with a gyroresonant core population.
- The presence of both RH and LH instabilities act to bunch both the ring and core ion populations, which results in an additional and potentially significant factor of ≤ 2 modulation to the wave amplitudes.
- The presence of both positive and negative ring ions results in variability in ICW polarisation with the dynamic spectra displaying LH, RH and linear polarisation, the latter as anticipated for oppositely handed circularly polarised waves with otherwise equivalent spectral properties.
- Despite the modulations associated with gyrophase bunching, the positive and negative ring instabilities behaved independently as indicated by the time histories of their average wave amplitudes, component temperatures, and wave spectral properties.

After characterising the behaviour of the instability in the Europan plasma environment, the simulations and Galileo wave observations were compared to determine if Cl^- pickup ions are able to explain the wave signatures observed by Galileo and if it is possible to estimate the absolute densities of the Chlorine ions from the observed waves. The following were concluded:

- The simulations and linear theory demonstrate that for the Europan pickup geometry, the RH wave power observed by Galileo is consistent with the pickup of Cl^-.

- The simulations suggest that variability in the wave polarisations is observed in systems, which contain instabilities driven by positive and negative ion rings, as was observed by Galileo.

- From the overall E11 and E15 wave amplitudes the Cl^+ or Cl^- densities are estimated to peak in the range of 0.1-1.5 cm^{-3}, this spread dependent on the unknown background Cl^+ and Cl^- densities and exact pickup velocity.

- The ICWs at the Chlorine ion gyrofrequency observed by Galileo were too brief to establish amplitudes for the LH and RH waves individually, and a threshold of $\sim$5% of the total Chlorine pickup ions was established below which an observable signal of the Cl^- instability would not be present.

- The occurrence of bunched ion populations, caused by the presence of both LH and RH ICWs can however complicate interpretation of ICWs driven by positive and negative pickup ions.

This study has investigated the behaviour of the RH ion cyclotron temperature anisotropy instability and also a method of using the wave polarisation to identify the presence of negatively charged pickup ions. This method is envisaged to be relevant to other environments in the outer solar system where negative ions are likely present in abundance and also provides context for planned in-situ observations to be gained from the upcoming ESA JUpiter ICy moons Explorer (JUICE) mission and the NASA Europa Clipper mission.

Chapter 6

Cassini CAPS observations of pickup ions at Rhea

6.1 Summary

Saturn's largest icy moon, Rhea, hosts a tenuous surface-sputtered exosphere composed primarily of molecular oxygen and carbon dioxide. In this chapter, I examine Cassini Plasma Spectrometer velocity space distributions near Rhea and confirm that Cassini detected nongyrotropic fluxes of outflowing CO_2^+ during both the R1 and R1.5 encounters. Accounting for this nongyrotropy, we show that these possess comparable alongtrack densities of $\sim 2\times10^{-3}$ cm^{-3}. Negatively charged pickup ions, also detected during R1, are surprisingly shown as consistent with mass 26$\pm$3 u, which we suggest are carbon-based compounds, such as CN^-, C_2H^-, C_2^-, or HCO^-, sputtered from carbonaceous material on the moons surface. The negative ions are calculated to possess alongtrack densities of $\sim 5\times10^{-4}$ cm^{-3} and are suggested to derive from exogenic compounds, a finding consistent with the existence of Rhea's dynamic CO_2 exosphere and surprisingly low O_2 sputtering yields. These pickup ions provide important context for understanding the exospheric and surface-ice composition of Rhea and of other icy moons which exhibit similar characteristics

A version of this chapter has been published as a *Geophysical Research Letter* with the citation: R. T. Desai, S. A. Taylor, L. H. Regoli, Coates, A. J., Thomsen, T. A. Nordheim, M. A. Cordiner, B. D. Teolis, M. F., Johnson, R. E., Jones, G. H., Cowee, M. M., Nordheim, T. A., Waite, J. H., Cassini identification of pickup ion compositions at Rhea, *Geophysical Research Letter*, 45, 10.1002/2017GL076588.

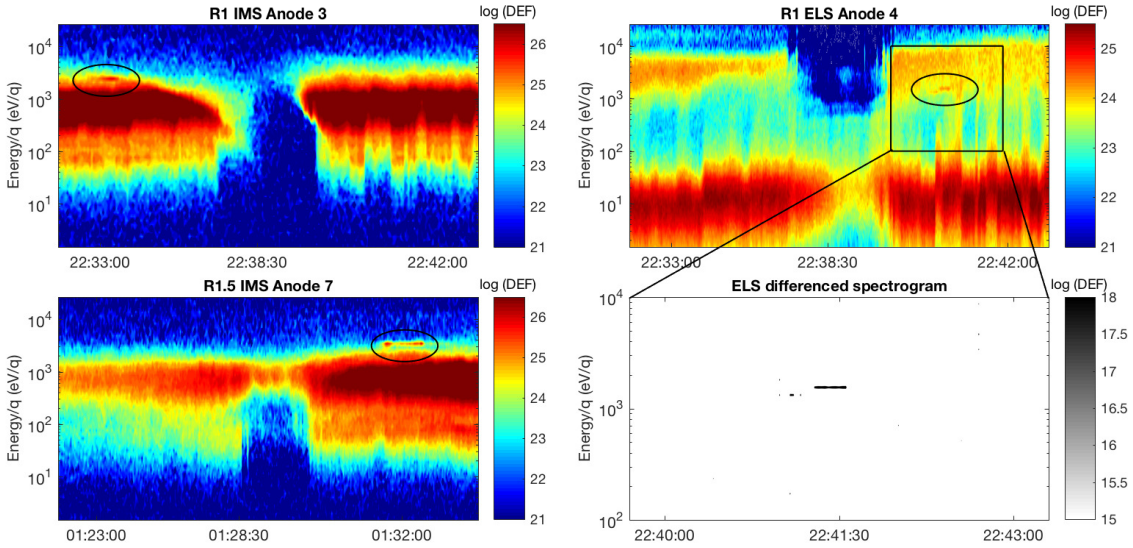

Figure 6.1: The left-hand panels show CAPS IMS differential energy flux (DEF) spectrograms acquired during the R1 and R1.5 encounters with Rhea and the right-hand panels CAPS ELS DEF spectrogram acquired during the R1 encounter. The IMS pickup ion detections are encircled at 22:33:00 during R1 at ∼2.5 keV and 01:33:00 during R1.5 at ∼3.5 keV. The negative pickup ion detections are evident at 22:41:30 at ∼1.5 keV. The lower right-hand panel shows a differenced plot of the ELS data, which shows a negatively charged pickup ion signature similar in appearance to the positive pickup ion signatures.

6.2 Introduction

Rhea is Saturn's largest icy moon with a radius of ∼764 km, and orbits within the sub-Alfvénic environment of Saturn's middle magnetosphere. As such, Rhea presents an archetype of the dominant satellite class at the outer planets, whose physical properties can be used to understand the formation and evolution of the giant planetary systems and, especially, their many moons.

A sputter-induced exosphere was first discovered to exist at Rhea by the Cassini spacecraft [*Teolis et al.*, 2010], a phenomenon also present at Dione, Europa, Callisto, and Ganymede [*Tokar et al.*, 2012; *Hall et al.*, 1998; *Carlson*, 1999]. Rhea's and Dione's exospheres were also surprisingly found to host large quantities of CO_2 [*Teolis and Waite*, 2016], a characteristic shared with Callisto. Rhea's surface is predominantly water ice whilst also containing lesser quantities of darker non-ice constituents and trace compounds such as CO_2 [*Clark et al.*, 2008]. Beneath this, Rhea's gravitational field indicates a body existing away from hydrostatic equilibrium, which might be differentiated [*Tortora et al.*, 2016], and possibly hosts a subsurface water ocean [*Hussmann et al.*, 2006].

Rhea is an unmagnetised body and acts to absorb incident magnetodisk plasma [*Khurana et al.*, 2008; *Roussos et al.*, 2008]. Ionised material can be directly picked up by the motional electric field and form "pickup ion" current systems, which, with the resulting j×B force and density gradients associated with the plasma wake [*Simon et al.*, 2012; *Khurana et al.*, 2017], slows down the incident magnetoplasma causing field-line draping and Alfvén wings. Pickup ions, as well as providing information on bulk and trace atmospheric constituents, impact the moon's plasma interaction and mass load Saturn's middle magnetosphere.

In a plasma flow, pickup ions will be accelerated to a maximum velocity of twice that of the bulk plasma and, in the plasma frame, will possess energies of

$$E_i = \frac{1}{2} m_i v_b^2 sin^2 \theta_{vb}, \tag{6.1}$$

where m_i is the pickup ion mass, v_b is the bulk plasma velocity in the initial rest frame, and θ_{vb} is the angle between the bulk plasma velocity and the magnetic field [*Coates et al.*, 1989].

At Rhea's orbit of ∼8.9 R_S, the Saturnian magnetic field is nominally dipolar and newly born ions will be accelerated perpendicularly to the magnetic field to execute rings in velocity space. If the size of the ion gyroradii significantly exceeds that of the pickup ion source region, the resultant distributions won't fill the entire ring and can be considered nongyrotropic.

Pickup ion distributions are inherently unstable and provide a source of free energy for plasma wave generation [*Wu and Davidson*, 1972]. These waves act scatter the distributions in pitch angle and energy, and heat ambient gyroresonant populations. Alfvén-cyclotron waves, generated by pickup ions, have been observed throughout Saturn's extended neutral cloud out to ∼8 Rs where the increased plasma beta (ratio of magnetic to thermal pressure) results in the Mirror Mode dominating [*Russell et al.*, 2006; *Meeks et al.*, 2016]. The magnetic signatures of mass loading have, however, not been reported in the vicinity of Rhea, despite increased O_2^+ abundances being observed at these radial distances [*Martens et al.*, 2008].

In this chapter, I examine Cassini Plasma Spectrometer (CAPS) observations of pickup ions outflowing from Rhea with emphasis on further constraining the composition and origin of the negatively charged pickup ions detected by the CAPS Electron Spectrometer (ELS).

6.3 Velocity Space Analysis

The CAPS Ion Mass Spectrometer (IMS) and CAPS Electron Spectrometer (ELS) [*Young et al.*, 2004] were designed to measure low energy ions and electrons in the ranges of 1 eV to 50.3 keV and 0.6 eV to 28.8 keV, respectively. CAPS is located on an actuator, which was held fixed during the Rhea flybys. Figure 6.1 shows the CAPS observations during the targeted R1 encounter on 26 November 2005 and the non-targeted R1.5 encounter on 30 August. Closest approach occurred at 765 km and 5736 km, respectively, and both flybys occurred behind the moon, thus providing the opportunity to observe outflowing material.

During both encounters, a marked drop-out in ion and electron fluxes occurs as Cassini traversed the moon's plasma wake. During R1, distinct plasma populations are visible in the IMS spectrogram around 22:33 UT at $\sim$2.5 keV, and during R1.5 a similar population is observed at 01:32 UT at $\sim$3.5 keV. In the ELS spectrogram, a distinct plasma population is visible at 22:41 UT at $\sim$1.6 keV, and a differenced plot, (obtained by averaging the counts on anodes oriented away from 90° pitch angle, anodes 2, 3, 6, 7, and subtracting these from anode 3) reveals this signature as analogous to the IMS signatures. These respective plasma populations have been identified as positively and negatively charged pickup ions deriving from Rhea and provided evidence for the moon's tenuous exosphere [*Teolis et al.*, 2010].

The IMS and ELS utilise electrostatic analysers to energy select charged particles, and the characteristic velocity imparted to newly created ions by the pickup process allows CAPS to discriminate between pickup ions of different masses. Figure 6.2 shows an IMS and ELS energy sweep corresponding to when these pickup ions were detected. The data are transformed into velocity space using the mass of anticipated pickup ions and projected onto planes parallel and perpendicular to the magnetic field and $-v \times B$ electric field, as measured by Cassini [e.g. *Wilson et al.*, 2010]. The spacecraft and plasma velocity are subtracted, leaving the measurements in the pickup ion rest frame and a contour representing the anticipated pickup ion ring distribution is overlaid, as predicted by Equation 6.1.

During R1 and R1.5, the pickup ions observed by the IMS appear consistent with masses 40$\pm$4 u and 46$\pm$4 u, respectively. This uncertainty derives from the width of the IMS energy bins and the plasma velocity, which varies between $\sim$55 and $\sim$60 km/s during R1, and $\sim$55 and $\sim$65 km/s during R1.5, see *Wilson et al.* [2010]. The pickup ions arrive with near-zero velocity parallel to the B-field as anticipated for pickup within a dipolar pickup geometry and are therefore

attributed to CO_2^+, a conclusion previously reached by *Teolis and Waite* [2016].

The pickup ions possess varying velocities parallel to the electric field indicating they are highly nongyrotropic and exist within slightly different locations in phase space. During both encounters the pickup ions appear shifted compared to the predicted velocity contours, the most likely explanation being that the plasma conditions were different closer to the moon, where and when the ions were produced, compared to at the time and location of their detection. In Figure 6.3, the nominal trajectories of outflowing positive and negative pickup ions are shown, calculated using Cassini field and plasma measurements. The CO_2^+ trajectories can be seen to correspond to where the respective detections were made during both R1 and R1.5.

The nongyrotropic nature of these distributions also becomes evident when examining these trajectories as they demonstrate how the pickup ions are only able to occupy a finite amount of the 2π velocity-ring space at any given instance. This also explains why the pickup ions are only observed over a finite time period as the pickup ion phase angle changes closer to the moon to where the CAPS finite FOV did not cover. Spatial variations in the ion production rate, due to the spatial distribution of the exospheric neutral density, could also contribute to this effect.

The identification of CO_2^+ on both the Rhea encounters raises interesting questions regarding the lack of O_2^+ pickup ions, as observed at Dione by Cassini [*Tokar et al.*, 2012]. The IMS spectra shown in Figure 6.4 do, however, feature a shoulder on the main corotational plasma distribution near $\sim$2 keV, which, when closer to Rhea (not shown), appears similar to the O_2^+ pickup ion detections reported by *Tokar et al.* [2012]. It is, however, difficult to differentiate this from the corotational plasma at Rhea's orbit, which exhibits a greater spread in energy compared to at Dione. Rhea's CO_2 and O_2 exosphere has been measured insitu by Cassini's Ion and Neutral Mass Spectrometer [*Teolis and Waite*, 2016], and the O_2 production rates have notably been determined to be significantly ($\sim$300 times) lower than that predicted from the sputtering of pure water-ice, and are consistent with the presence of significant surface impurities.

The consistency of these identifications with the analysis and exospheric modelling results reported by *Teolis and Waite* [2016], validates the use of the pickup ions velocity as a means of identifying composition, a method which will now be applied to analyse the negatively charged pickup ions.

The CAPS-ELS is capable of detecting negatively charged ions [*Coates et al.*, 2007a], and *Teolis et al.* [2010] reported that the negatively charged pickup ions detected during R1 were likely

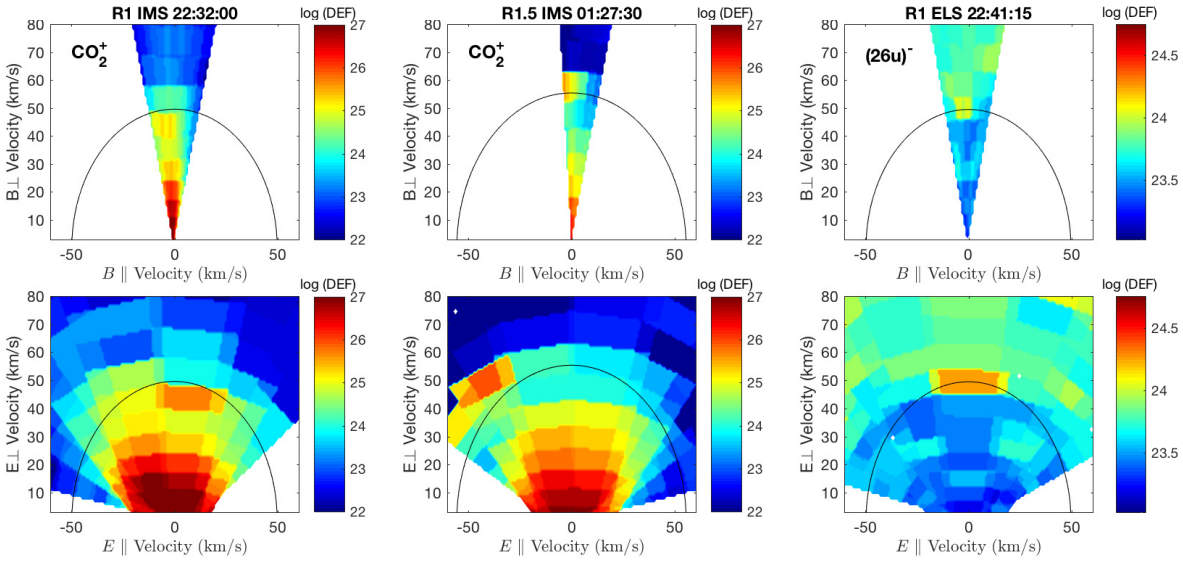

Figure 6.2: The CAPS data are converted into velocity space assuming CO_2^+ (left and centre panels) and mass 26 u (right-hand panels). These are projected into planes parallel and perpendicular to the magnetic field and $-v \times B$ electric field for a single energy sweep. A linear interpolation is used for overlapping FOVs, which dilutes the detections when projected relative to the magnetic field. The geometrical look directions are used, which, combined with each anodes 20° width, smears the detections in the parallel and anti-parallel directions. The pickup velocity ring-contour are overlaid.

comprised of O^-. While initially reported as produced from electron attachment to atmospheric species, the inefficiency of this process was highlighted in a subsequent study [*Teolis and Waite*, 2016; *Itikawa*, 2009], and it was consequently suggested that these were likely produced by surface mediated process such as sputtering. In Figure 6.1 and 6.2, these detections appear above the anticipated O^- energy by ∼15 km/s, which corresponds to an energy discrepancy of ∼500 eV. These detections therefore appear consistent with a heavier species of mass 26±3 u. It is, however, possible for pickup ions to be accelerated to increased energies by a number of processes, which are now examined:

- Intense plasma waves have been observed at Rhea [*Santolík et al.*, 2011], and right-hand polarised Alfvén-cyclotron waves, which would gyroresonantly interact with O^-, could be produced by negatively charged pickup ions [*Desai et al.*, 2017b]. These however feed of the free energy from the pickup ions and this effect could not be significant over such a short time period.

- Specular reflection from the lunar surface has been observed to accelerate solar wind ions to three times that of the bulk plasma velocity [*Saito et al.*, 2008]. This is however judged

unlikely at Rhea due to high water-group photo-detachment rates in Saturn's magnetosphere [*Coates et al.*, 2009] precluding negatively charged O^- existing in abundance as an ambient magnetospheric population.

- Sputtering can result in energy being transferred to the sputter products. O^- sputtering experiments have, however, shown this to be too inefficient to account for the velocity discrepancy discovered herein [*Tang et al.*, 1996].

- Previous theoretical studies have predicted large negative surface potentials at Rhea up to several hundred volts [Roussos et al., 2010; Nordheim et al., 2014] and observations during the Rhea R2 flyby appear to support this [*Santolík et al.*, 2011]. However, for surface potentials to explain the observed energy discrepancy, a negative surface potential of 500V would have to occur uniformly over a large region of Rhea's surface. Given that the theoretical studies have predicted surface potentials, which vary strongly depending on surface location, this is not considered likely.

- The bulk plasma velocity is predicted to vary in the vicinity of Rhea and in particular on the Saturn-facing hemisphere [*Roussos et al.*, 2008]. The CAPS plasma velocity measurements during R1 were, however, obtained in this region and do not show this effect to be significant [*Wilson et al.*, 2010].

The apparent inconsistency with O^- pickup ions raises two possibilities. Firstly, the signature could be produced by an electron beam oriented perpendicularly to the magnetic field. The longevity of this signatures above the background populations, its spatial occurrence, and the similarity to the unambiguous positive pickup ion signatures, are however highly indicative of negatively charged pickup ions of mass 26 ± 3 u, of a type not previously considered.

6.4 Origin of the Negative Ions

Heavier negative pickup ions could result from carbon-based compounds with positive electron affinities (EA), such as CN^-, C_2H^-, C_2^-, or HCO^-, being produced via sputtering of the moon's surface. Spectroscopic observations of Rhea at $\leq$5.2 μm wavelengths have revealed unusually dark material, which is consistent with the presence of either tholin (C-, H-, N-, O-bearing) and/or iron (Fe- bearing) compounds [*Ciarniello et al.*, 2011; *Stephan et al.*, 2012; *Scipioni et al.*, 2014]. This material is also present at Dione, Phoebe, Iapetus, Hyperion, Epimetheus

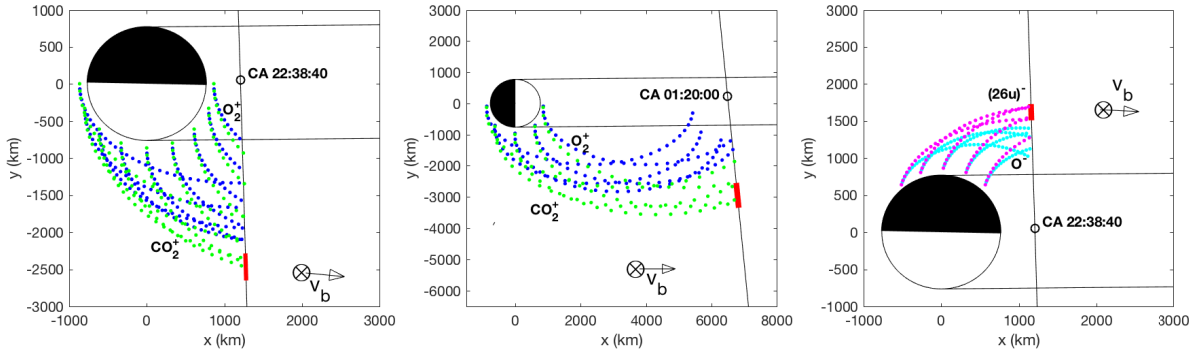

Figure 6.3: Nominal trajectories of outflowing O_2^+ (blue) and CO_2^+ (green) during R1 in the left-hand panel and during R1.5 in the centre panels. Outflowing O^- (cyan) and negative ions of 24u (magenta) are shown during R1 in the right-hand panel. The trajectories are traced according to the gyroradii of the pickup ions, with the inputs deriving from Cassini plasma and field measurements at the time of detection and displayed in a Rhea centred coordinate system. The nominal corotational wake and approximate sunlit regions of Rhea are marked and times along Cassini's trajectory where the pickup ions were detected are marked red. The pickup ion trajectories originate within 100 km of Rhea's surface where increased neutral abundances are anticipated.

and throughout Saturn's F-ring, thus implying a common process occurring throughout these icy satellites [*Clark et al.*, 2008]. Dark tholin-like material is also apparent in spectroscopic observations of the Galilean icy moons, which is thought to be comprised of hydrocarbon or cyanide compounds [*McCord et al.*, 1998]. An abundance of electrons are also anticipated near Rhea's negatively charged surface, which could readily attach onto electrophillic molecules.

Visual Infrared Mapping Spectrometer (VIMS) observations of Rhea have shown that an $\sim$1% tholin-type admixture could explain unidentified features in the near-infrared [*Ciarniello et al.*, 2011]. It therefore initially appears surprising that such a trace constituent would be observed outflowing in significant quantities. The pickup ion trajectories, however, shown in Figure 6.3, demonstrate how pickup ions originating from different regions in Rhea's exosphere become concentrated in phase space when observed, a phenomenon, which appears enhanced for heavier species due to their larger gyroradii. This could explain why a trace heavier species might preferentially be detected.

VIMS observations of Rhea's surface are also derived from the top few microns and exogenous material might not have penetrated this far. A thin carbonaceous surface coating on the moon, possibly only a few monolayers thick, could therefore consist of significantly larger fraction of this unidentified dark material than is apparent from remote observations. This could have been deposited from magnetospheric plasma and dust populations, or been delivered by microm-

eteorite, cometary and interplanetary particles raining into the Saturn system [*Clark et al.*, 2008; *Stephan et al.*, 2012]. At Rhea, the spatial distributions of the unidentified material indeed suggest an external origin, with higher concentrations on the leading and trailing hemispheres pointing to magnetospheric dust and plasma deposition, respectively [*Clark et al.*, 2008; *Scipioni et al.*, 2014].

Dark spots are also observed near Rhea's equator, which are associated with surface disruptions [*Schenk et al.*, 2011]. The negative pickup ions map back to near Rhea's equatorial regions and the possibility that endogenic carbon-rich material could have been released onto the surface via impact events such as the cause of the Inktomi impact crater, or the discolored spots, or from further large-scale geologocial resurfacing [e.g. *Stephan et al.*, 2010], cannot be discounted.

It is possible for tholin-type compounds to be incorporated into the ice from when the moon formed. Compounds such as C_2H_2, CH_3OH and HCN appear ubiquitously within cometary ices at $\sim$1% of H_2O abundances, thus signifying their presence in the protosolar accretion disk from which the giant planetary systems formed [*Mumma and Charnley*, 2011]. *Teolis and Waite* [2016] go on to predict the quantity of carbon atoms in Rhea's surface ice to be as high as 13% that of H_2O and processes such as photolysis, radiolysis, and heating could act to process the chemical state of such compounds, whether endogenic or exogenic to Rhea.

The CN^- (EA = 3.8 eV), C_2H^- (EA = 3.0 eV) and C_2^- (EA = 3.3 eV) anions can be produced from electrons impacting compounds such as hydrogen cyanide, acetylene and diacetylene [*Inoue, Masao*, 1966; *May et al.*, 2008]. Graphite-compounds could be created through radiation bombardment and surface chemistry [*Lifshitz et al.*, 1990; *McCord et al.*, 1998], which could produce C_2^-. Sputtering experiments indeed predict the efficient production of the $C_2H_x^-$ anions from hydrocarbon compounds [*Johnson*, 1993], and these are suggested as candidate sputter products at Europa [*Johnson et al.*, 1998]. Carbon chain anions have also possibly been observed at Comet Halley [*Cordiner and Charnley*, 2014] and exist elsewhere in Saturn's magnetosphere, amongst carbon-rich compounds in Titan's ionosphere [*Desai et al.*, 2017a]. The HCO^- (EA = 0.31 eV) anion could possibly be formed by deprotonation or dissociative electron attachment of H_2CO or CH_3OH. Further study of the sputtering of carbon-rich ejecta from ices representative of the icy moons of Saturn and Jupiter, could surely provide further insight into which sputtering rates are significant with regards to these anions.

Although the aforementioned negative pickup ions appear inconsistent with O^-, it should

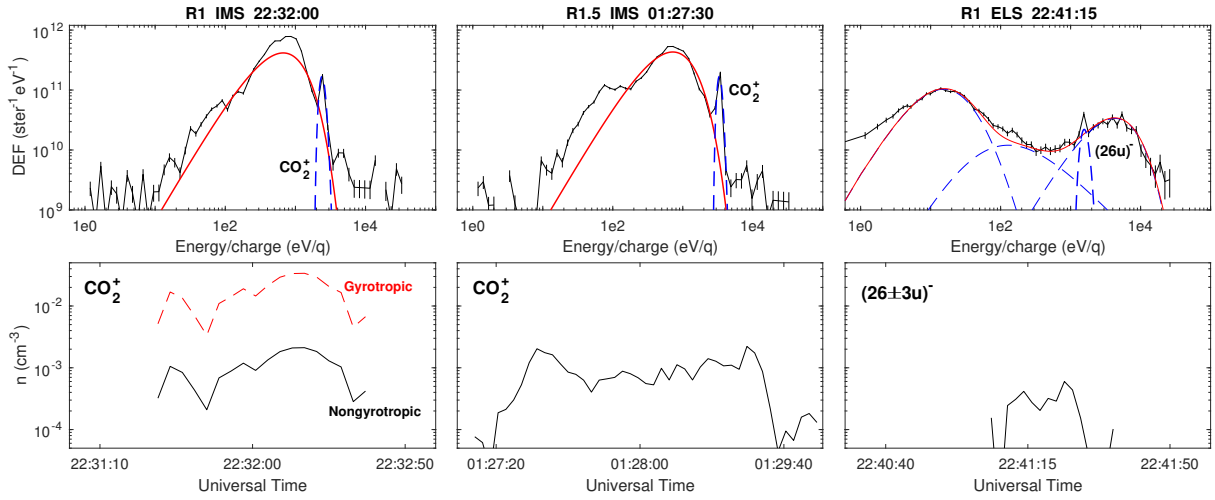

Figure 6.4: The top panels show an IMS and ELS spectrum from each of the pickup ion detections identified in Figure 6.1. The IMS background plasma is fitted to using Maxwellian velocity distributions for water-group ions and the ELS spectra is fitted using a low, medium and high energy kappa distributions. The lower panels show the calculated alongtrack densities.

be noted that in the differenced ELS spectrogram displayed in Figure 6.1, further signatures also consistent with negative pickup ions are present earlier in time at a lower energy. Although too brief to conclusively identify these as negative ions, this might represent the same pickup ion population dispersed in energy via interactions with a surface-generated electric field as observed at the Earth's moon [*Poppe et al.*, 2012], or indeed could correspond to O^- pickup ions given their location in phase space, see Figure 6.3.

6.5 Densities & Escape Rates

Figure 6.4 shows IMS energy spectra during R1 and R1.5 and the ELS spectrum during R1, corresponding to the pickup ion detections. The ion background is fitted using a Maxwellian water-group velocity distribution, which appears to better match the data during R1.5 when Cassini was farther from Rhea's plasma interaction. In either instance the pickup ion detections are clearly identifiable and these fits are sufficient to isolate the pickup ion populations. A lower energy hydrogen population is also present, as well as further high energy populations evident at >4 keV. These are not considered for this analysis.

The ELS spectrum shows two distinct electron populations at low and high energies, which are represented using a double Kappa distribution [*Schippers et al.*, 2009]. A significant amount of intermediary electrons are also present, which are also approximated by a broad Kappa distri-

bution. The proximity to Rhea's plasma interaction, as well as multiple possible photoelectron populations [*Taylor et al.*, 2018], result in significant variabilities in the electron spectrum during R1. The negatively charged pickup ion population consistently remains above the background throughout this variability, see Figure 6.1.

The nongyrotropic pickup ion densities are calculated using an expression derived for partially-filled ring-velocity distributions. In the plasma frame, the pickup ions can be expressed relative to the magnetic field as

$$f(v) = \frac{n}{\Delta\phi v_{b\perp}} \delta(v_\perp - v_{b\perp}) \delta(v_\parallel - v_{b\parallel}), \tag{6.2}$$

where $\Delta\phi = 2\pi$ in the case of a gyrotropic ring [*Wu and Davidson*, 1972].

Pickup ion trajectories derived from the extrema of Rhea's exosphere, see Figure 6.3, are used to estimate that the pickup ions are able to fill $\sim \pi/4$ of velocity space, see Figure 6.3. This can be expressed in the spacecraft frame as

$$f(v) = \frac{n}{\Delta\phi v_{b\perp}} \delta(v_b - v_c) \delta v_{b\parallel}, \tag{6.3}$$

where v_c is the velocity corresponding to the CAPS energy bin in which the pickup ions were detected. The spacecraft velocity is removed for an inertial reference frame. The pickup ion density, n, can then be calculated from the count rate, R_c by the expression,

$$n = \frac{R_c \Delta\phi}{v_b \varepsilon A \Delta\phi_c}, \tag{6.4}$$

where the area of acceptance $A = 0.33 cm^{-2}$, the CAPS phase angle coverage $\Delta\phi_c = \pi/2$, and ε is the Microchannel Plate (MCP) efficiency. An MCP efficiency of 0.46 is used for the CO_2^+ pickup ions and 0.50 for the negatively charged pickup ions [*Tokar et al.*, 2012; *Stephen and Peko*, 2000].

Figure 6.4 shows the resulting IMS and ELS along-track densities. The CO_2^+ densities peak at $\sim 2.5 \times 10^{-3}$ cm^{-3} whereas the negatively charged pickup ions peak at values nearly an order of magnitude lower at $\sim$5x10^{-4}. The CO_2^+ densities during R1 are also calculated assuming a gyrotropic distribution to demonstrate how such an assumption significantly overestimates abundances.

Whilst Rhea's exosphere has shown to be dynamic and variable, the CO_2^+ densities can be

integrated over the hemisphere of the moon where the motional electric field will result in ion escape, to calculate approximate global escape rates. Assuming uniform ionisation, this results in an estimated $\sim 4.6\times10^{20}$ CO_2^+ s^{-1} escaping the moon during R1 and $\sim 5.7\times10^{20}$ CO_2^+ s^{-1} during R1.5. This rate is compatible with the varying CO_2 production rates resulting from the model of *Teolis and Waite* [2016]. This is also $\sim$0.25 times that predicted at Dione, which experiences more intense plasma bombardment due to being located deeper inside Saturn's magnetosphere [*Wilson et al.*, 2017]. A similar calculation can be performed for the negative ions, which results in an outflow rate of $\sim 5.4\times10^{19}$ s^{-1}.

It should be noted that these rates are only an estimate as studies have shown highly varying dynamical processes at Rhea's magnetospheric interaction at small or intermediate scales, and such dynamics may "destroy" or disperse the smooth paths of pick-up ions with small or moderate-sized gyroradii [*Roussos et al.*, 2012]. It is therefore not clear precisely, which density should be used to represent globally averaged ion production rates.

The outflowing pickup ions will contribute to magnetospheric ion populations. Rhea's CO_2 exosphere may therefore provide a source of the 44 u ions, or the carbon and oxygen ions via dissociative reactions, identified at radial distances of $<$20 R_S [*Christon et al.*, 2015]. If the breakup is sufficiently fast, this may provide some explanation for the elevated O_2^+ levels reported by *Martens et al.* [2008] at Rhea's orbit.

Further analysis of the generation of instabilities associated with nongyrotropic pickup ions, in a plasma beta regime representative of Rhea's plasma environment, is required to understand whether the magnetic signature of this mass loading might be visible.

6.6 Summary & Conclusions

This study has analysed the composition, density and outflow rates of positively and negatively charged pickup ion distributions at Saturn's icy moon Rhea and determined the following:

- CAPS-IMS observed nongyrotropic fluxes of CO_2^+ pickup ions during the R1 and R1.5 encounters with comparable alongtrack densities of $\lesssim 2\times10^{-3}$cm^{-3}.

- The R1 CAPS-ELS detections, previously identified as deriving from the pickup of O^- [*Teolis et al.*, 2010], are shown as consistent with a heavier species of mass 26$\pm$3u. These

are consequently identified as negatively charged carbon-based compounds produced from tholin-type material on Rhea's surface.

- The negatively charged pickup ions are suggested to consist of CN^-, C_2H^-, C_2^- or HCO^-, resulting from the dark material observed at Rhea and throughout the icy moons of Saturn. This may therefore well be the first identification of organic material at an icy moon.

- The negatively charged ions were observed with alongtrack densities of $\lesssim 5\times10^{-4}$ cm^{-3}, which resulted in estimated outflow rates of $\sim 5.4\times10^{19}$ s^{-1}. This calculation is rudimentary and yet the first for Rhea. Previous outflow rates were calculated from the model of *Teolis and Waite* [2016], which are in agreement with these observations.

- Possible further negative ion signatures are also identified, which could represent dispersion in energy as a result of surface charging or a further population of O^- pickup ions. The background plasma at Rhea's orbit mean pickup ions with masses (energies) closer to that of the ambient plasma, such as O^- and O_2^+, are difficult to identify.

This study provides context for understanding the exospheric and surface compositions and plasma interaction of Rhea as well as other icy satellites in the outer solar system. The trace constituents in Rhea's surface ice, and also at other Saturnian and Jovian icy moons, are largely unconstrained and it remains to be determined just how similar or different these ices are to each other or indeed to ices formed elsewhere in the solar system such as those within comets and further icy bodies.

Chapter 7

Conclusions & Further Work

7.1 Summary & Conclusions

The research described in this thesis has focussed on advancing the understanding of negatively charged ions in outer solar system plasmas.

The physics of plasmas and negative ions were first described, which was followed by a comprehensive review of the current state of knowledge on negative ions in astrophysical and atmospheric environments. From this review distinct themes emerged:

The first theme that emerged was that of the hydrogen negative ion, H^-. H^- exists in abundance in within the outer layers of stars with photospheric temperatures of $<$7000 K, thereby impacting their macroscopic properties. H^- was present in the early Universe and played a role in formation of the first molecular compounds within the Universe. Most recently H^- has been discovered within the Solar Wind at increased heliocentric distances, thereby signifying that hydrogen plasmas are environments where negative ions can exist.

The second theme involves that of electrophillic carbon-based molecules. Negatively charged carbon chains are known to be ubiquitous within interstellar molecular clouds, and have recently also surprisingly been discovered in abundance in Titan's upper atmosphere. These environments are rich in organic compounds and these detections indeed hinted towards a pivotal role played by negative ions with regards to producing complex molecules.

The third theme was that of oxygen or water based negative ion plasmas. The first environments where negative ions were first known to naturally exist was the Earth's atmosphere and here, oxygen-based negative ions formed the basis for the formation of a number of negative ions, which dominate ionospheric dynamics during certain conditions. The detections of negatively charged

water cluster ions at Saturn's moon, Enceladus, further showed how electrophillic oxygen based molecules could facilitate the presence of negative ions within plasmas.

Beyond these, the halogen Chlorine and Bromine anion species have also been observed to naturally occur due their high electron affinities. In addition to the water based negative ions, Chlorine and Bromine prevail in the Earth's ionosphere and it was highlighted that these species could also have been observed in the Jovian system at Europa.

Following this, three research chapters then focussed on negative ion populations observed at Titan and Rhea, and inferred to exist at Europa, and the following conclusions were drawn.

7.1.1 Titan

Titan's atmospheric chemistry remains, at the time of writing, the most complex known within any in the solar system. The Cassini Electron Spectrometer (ELS) notable detected large quantities of negative ions in the range of 12-13,800 u/q [*Coates et al.*, 2007a]. The response function of this instrument to negative ions presented a significant barrier to understanding the composition and role played by this unexpected upper atmospheric constituent. The research effort began by developing an advanced understanding of the manner in which the negative ions were detected by the ELS. This is in part summarised within the Chapter 3 entitled 'Method & Techniques'. The material contains a review of the various methods, which can be used to derive plasma parameters and also drew together knowledge from different fields, including that of atomic physics and ion-surface interactions. The research into the negative ions in Titan's ionosphere then unfolded as described in Chapter 4. From this the following conclusions were drawn:

- As CAPS scanned across the spacecraft ram direction, the nominal energy of particles registered in each ELS energy bin was determined to be dependent on the angle of incidence, in accordance with the calibrated energy-angle response function. This effect was found to smear the negative ion detections over an artificially large energy, and thus mass, range. Applying a correction based upon laboratory calibration data was able to explain and remove this phenomenon.

- The negative potential gained by Cassini's surfaces in Titan's relatively dense ionospheric plasma was found to alter the measured negative ions energy and also angle of incidence [*Jones et al.*, 2011]. As differential charging occurred across Cassini's surface [*Crary et al.*,

2009], further analysis determined that an increased spacecraft potential measured by the RPWS-LP corresponded to the negative ions arriving from a greater angle to the ram direction. The various orientations of Cassini during the Titan flybys, the differing plasma conditions across various local times, however, precluded this deflection being further analysed and used as a gauge of spacecraft potential.

- In Cassini's reference frame, a negative ion species is observed as a beam arriving from the the spacecraft ram direction. The observations therefore consist of the negative ion distribution function processed by the instruments response function. To deconvolve this effect the negative ions were approximated by a Maxwell-Boltzmann distribution and the ELS instrument response function was represented by a Gaussian distribution, which is well captured the measured ΔE/E response. It was found that this method could accurately reproduce the ELS negative ion detections.

- This method was then applied to the ELS dataset during several flybys and the mass groups outlined by *Coates et al.* [2007a] and [*Wellbrock et al.*, 2013] were further constrained. The method was able to statistically attribute the first two mass groups as comprising of the carbon chains anions, CN^-/C_2H^- and C_3N^-/C_4H^-, respectively. These detections add Titan to an increasing list of astrophysical environments where these species have been observed.

- This method was also applied to constrain the higher mass species. The third mass group could at higher altitudes be consistent with the carbon chain anions C_5N^-/C_6H^- but at lower altitudes covers a higher and increased mass range. These detections are not consistent with any negative ion species previously observed, and are suggested to present the first evidence for anion chemistry in space involving structures other than linear chains.

- The MCP efficiency has, in previous studies, been estimated to be similar to positive ions [*Coates et al.*, 2007a; *Wellbrock*, 2012]. It was highlighted in Chapter 3 how the detection efficiency for detection ions appeared to be significantly larger than for positively charged ions [*Peko and Stephen*, 2000; *Stephen and Peko*, 2000]. A new MCP efficiency was applied to the negative ions dataset and the densities were shown to be lower than previously observed although remain significantly higher than chemical models are able to explain [e.g.

Vuitton et al., 2009a; *Dobrijevic et al.*, 2016].

Results from this chapter have been published as *Astrophysical Journal Letter* with the citation: Desai, R. T., Coates, A. J., Wellbrock, A., Vuitton, V., Crary, F. J., Gonzalez, D. G., Shebanits, O., Jones, G. H., Waite, J. H., Cordiner, M. A., Taylor S. A., Kataria, D. O., Wahlund, J.-E., Edberg, N. J. T., and Sittler, E. C. Carbon chains anions and the growth of complex organic molecules in Titan's ionosphere, *Astrophysical Journal Letters*, 844, 2, L18.

7.1.2 Europa

Negatively charged chlorine ions were hypothesised to be generating a plasma instability at Europa [*Volwerk et al.*, 2001]. This was inferred through Galileo magnetometer observation of right-handed wave power at the Chlorine ion gyrofrequency. To understand this phenomenon and whether this could indeed be occurring, the first hybrid simulation study of negatively charged pickup ions was carried out. The hybrid simulation technique was outlined in Chapter 3, which provided the tool with which the instability could be numerically reproduced. After running an ensemble of simulations for numerous inputs conditions and employing advanced diagnostics to understand the outputs, the following were concluded:

- A negatively charged pickup ion ring distribution will generate near circularly polarised RH waves consistent with theoretical predictions. The right-hand wave power observed by Galileo at Europa is therefore shown to be consistent with the pickup of Cl^{-}.

- The RH ring-instability behaviour was analogous to that of the LH ring-instability with respect to the resonant frequencies, wave numbers excited and interactions with a gyroresonant core population.

- The cogeneration of both RH and LH instabilities were found to induce gyrophase bunching within the ring and core ion populations. This resulted in a non-trivial modulations to the wave amplitudes, which reached values ≤ 2 than anticipated. This phenomenon was highlighted as potentially introducing complications when interpretation wave amplitudes..

- The cogeneration of both RH and LH instabilities caused variability in the resultant wave polarisation, as was observed by Galileo.

- From the overall wave amplitudes observed by Galileo, the Cl^+ or Cl^- densities are estimated to peak in the range of $0.1 - 1.5/cc$, this spread dependent on the unknown background Chlorine densities and exact pickup velocity.

- The waves at the Chlorine ion gyrofrequency observed by Galileo were too brief to establish amplitudes for the LH and RH waves individually, and a threshold of $\sim$5% of the total Chlorine pickup ions was established below which an observable signal of the Cl^- instability would not be present.

- The analysis of the wave polarisation confirms the hypothesis of *Volwerk et al.* [2001] and constrains this method of using magnetometer observations of wave polarisations to detect negatively charged pickup ions. This can be utilised in further plasma environments where negative ions might exist.

The presence of negatively charged pickup populations have also been predicted by global hybrid simulations of Titan's plasma interaction [*Ledvina and Brecht*, 2012] and have also been observed at Rhea [*Teolis et al.*, 2010]. This study forms the basis for understanding the instability characteristics of these species. The results also further the understanding of what observations ESA's JUICE and NASA's Europa Clipper missions can achieve and indeed what they might look for.

A reduced version of this chapter has been published as an *Journal of Geophysical Research Article* with the citation: Desai. R. T. Cowee, M. M. Wei, H. Fu, X. Gary, S. P. Volwerk, M. Coates, A. J., Hybrid simulations of positively and negatively charged pickup ions and cyclotron wave generation at Europa, *Journal of Geophysical Research: Space Physics*, Vol. 122, Issue 10, p. 408-420.

7.1.3 Rhea

At Saturn's largest icy moon, Rhea, negatively charged pickup ions, detected once again by the CAPS-ELS, provided evidence for the moon's sputter-induced atmosphere. Beyond their initial identification however, further analysis had not been reported other than to suggest that these were O^-. To further investigate this plasma population, the final research chapter of this thesis utilised the the advanced understanding of the instrument response to negative ions gained through the first research chapter and also the theoretical understanding of pickup ions gained through the hybrid simulation chapter.

The velocity space analysis utilised in this chapter was applied to the positively charged pickup ions detected at Rhea by the CAPS-IMS and which were identified by *Teolis and Waite* [2016] as consisting of CO_2^+. After reproducing the same results, this method was applied to the negatively charged pickup ions and the following were concluded:

- The negatively charged detections, previously identified as deriving from the pickup of O^- [*Teolis et al.*, 2010], are shown as consistent with a heavier species in the range of 26±3u.

- These are consequently identified as negatively charged carbon-based compounds produced from dark tholin-type material observed on Rhea's surface. Unidentified dark material is found throughout the icy satellites of Saturn in Cassini near-infrared observations, which is suggested to derive from either tholin or iron compounds [*Clark et al.*, 2008]. The CAPS negatively charged pickup ions appear to be the first insitu measurement of particles deriving from this.

- The negatively charged pickup ions are suggested to consist of CN^-, C_2H^- or C_2^-. The lack of further laboratory experiments on the sputtering rates of these species from icy surfaces precludes their definitive identification.

- The negatively charged ions were observed with alongtrack densities of $\sim 5\times10^{-4}$ cm^{-3}, which resulted in estimated outflow rates of 5.4×10^{19} s^{-1}.

- The nongyrotropic pickup ions distributions at Rhea resulted from the size of the ion gyroradii, r_g, exceeding the size of their source region, l_{source}, a phenomenon also present at Titan. The instability characteristics and observable signatures of such populations in Saturn's magnetosphere have yet to be constrained.

These results are highly relevant to icy moons with similar exospheric and surface characteristics. These include the icy satellites orbiting Saturn and possible also Jupiter although the similarities and differences between Saturn's and Jupiter's icy moons have yet to receive quantitative consideration.

A version of this chapter has been published as a *Geophysical Research Letter* with the citation: R. T. Desai, S. A. Taylor, L. H. Regoli, Coates, A. J., Thomsen, T. A. Nordheim, M. A. Cordiner, B. D. Teolis, M. F., Johnson, R. E., Jones, G. H., Cowee, M. M., Nordheim, T.

A., Waite, J. H., Cassini CAPS identification of pickup ion compositions at Rhea, *Geophysical Research Letter*, 45, 10.1002/2017GL076588.

7.2 Further work

The conclusions reached within this thesis has resulted in several further spin-of research projects and directions, which were too extensive to describe or pursue within the timeframe that this thesis was carried out. In this section several further directions are outlined as suggestions for future work.

7.2.1 MCP efficiency characterisation for heavy positive and heavy negative ions

Detections at Titan still require further understanding and in particular the MCP electron emission characteristics at energies $<$1 keV. Above 1 keV the electron emission processes are dominated by kinetic emission [*Baragiola et al.*, 1979] and are therefore similar for positive and negative ions species [e.g. *Peko and Stephen*, 2000]. Below this region potential emission processes start to dominate and only a limited number of studies have examined the efficiencies in this regime. At present the Titan negative ion densities are constrained to a mass range of an order of magnitude, using values 0.05 and 0.50 for species $<$100 u. The densities of the larger negative ion densities are even more unconstrained as these detections are farther away from existing MCP efficiency measurements. To address this the following steps could be taken:

- Laboratory tests for positive and negative ion MCP efficiency across energies from 100 eV to 10 keV, thus spanning the regimes dominated by kinetic and potential emission.
- Repeat these tests for various mass ion species where positive and negative charged ions can be produced such as O^+ and O^-.
- Apply these updated efficiency values to the Titan dataset to accurately determine the negative ion abundances observed by Cassini.

7.2.2 From Cassini to ALMA

The success of the Cassini-Huygens mission is unparalleled and has opened our eyes to the many wonders of Saturn and its many moons, itself almost a mini-solar system in its own right.

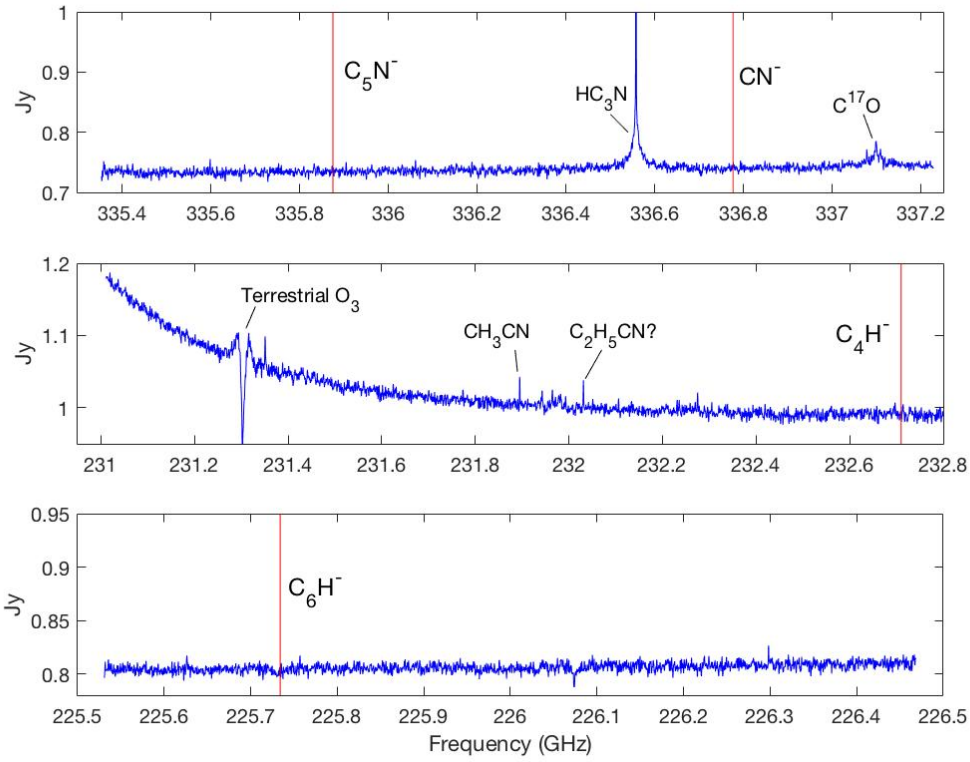

[h]

Figure 7.1: ALMA Archive data showing the lack of detections (red) of several of the chain anions as well as notable features present in the spectra. Panels (a) & (b) were obtained from flux calibration data and panel (c) from science observation 2012.1.00064.S (PI: Vinatier)..

In the absence of a return mission to Saturn, as is the case at the time of writing, it is important that the notable discoveries made and scientific understanding gained is built upon by future research efforts.

The Atacama Large Millimeter-Submillimeter Array (ALMA) is currently the largest astronomical project in existence and has in recent years gained near full capacity, thus providing unprecedented capabilities to probe astrophysical and solar system objects. This facility provides the necessary spectral and spatial resolution to carry on from Cassini's pioneering findings by further probing the composition of Titan's atmosphere. As well as providing dedicated science observing time, ALMA also routinely uses Titan for flux calibration and therefore provides relevant datasets for scientific analysis. This has already been carried out and, for example, *Cordiner and Charnley* [2014] demonstrate how ALMA is capable of observing HNC and HC_3N distributions in Titan's atmosphere.

Figure 7.1 shows ALMA data over three different frequencies bands. The top two panels

show publicly available flux calibration data and the bottom panel shows a publicly available science observation. Several feature can be observed in the spectrum, such as; HC_3N, a CO isotopologue, terrestrial O_3, CF_3CN, C_2H_5CN, as well as several further unidentified lines. These data are the result of searching through ALMA Archive to identify whether ALMA had already observed negative ions. The frequencies marked in red denote where the emission lines of several of the carbon chain anions identified in Chapter 4 are anticipated, these observations showing a clear lack of detections. The lack of non-detection is however not a null result as these data can be used to set upper limits on the negative ion abundances.

To further build upon the CAPS-ELS negative ion detections, the following directions could be taken:

- Use a radiative transfer code, such as Nemesis [*Irwin et al.*, 2008], to exploit the ALMA datasets shown in Figure 7.1, as well as further Archive data, to calculate upper limits on the carbon chain anion abundances at Titan.

- Combine existing ALMA datasets of overlapping frequencies to obtain enhanced spectral resolution to try make a detection or even lower upper limits.

- Propose for further observing time for detections and mapping purposes. Whilst the presence of carbon chain anions has been demonstrated, it is unknown whether these are hydrocarbon or cyanide species and the reported densities remain at odds with chemical models.

7.2.3 Nongyrotropic simulations

The pickup ion distributions at Rhea were found to be highly nongyrotropic a phenomenon due to the gyroradii of ions outflowing from the moon, exceeding the size of the region in which they were generated. Nongyrotropic pickup ions have also been observed at Titan [*Regoli et al.*, 2016]. The instability characteristics of nongyrotroic pickup ions in the Saturnian system therefore require further analyses, a research direction well suited to the hybrid simulation technique described in Chapter 3 and successfully employed in Chapter 5.

Whilst this topic requires detailed consideration, some preliminary test simulations were carried to explore this concept. Figure 7.2 shows the velocity space distributions at at four different times during four different runs where the code was modified to include pickup ion distributions with varying degrees of nongyrotropy. These simulations can either be run with ions continuously

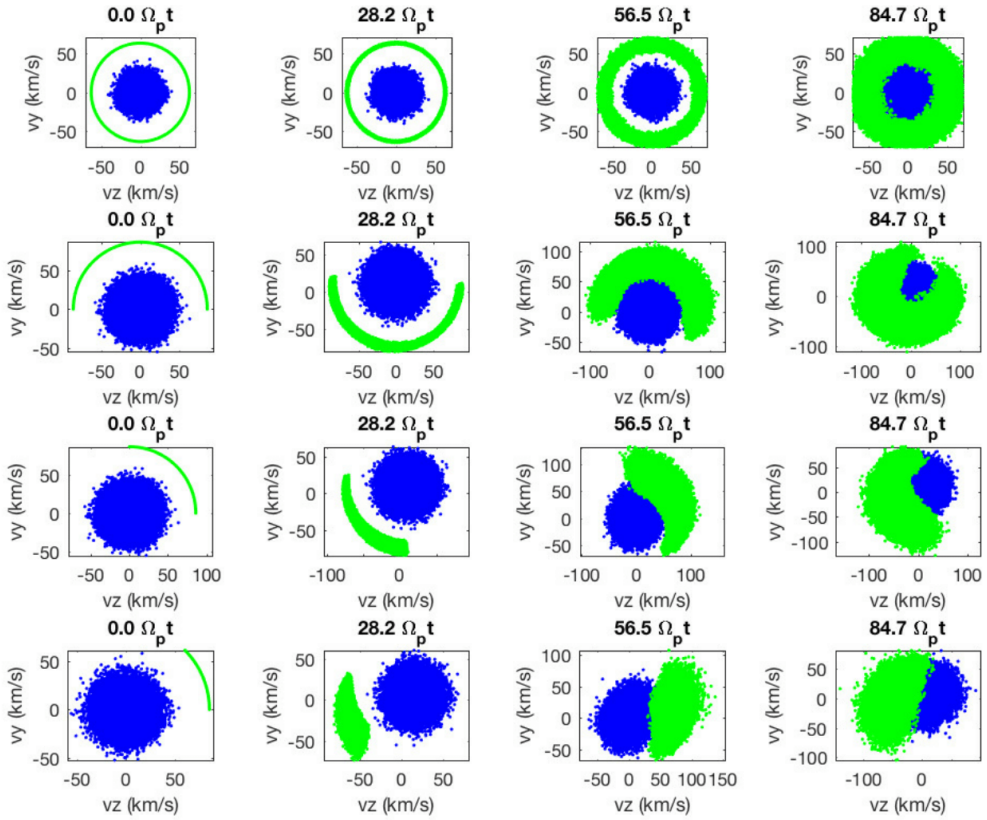

Figure 7.2: These simulations consist of 512x256 grid points over 256x128 inertial lengths with the simulation x-axis once again aligned with the ambient magnetic field. In this preliminary investigations the plasma is considered as CO_2^+ with 80% core and 20% pickup ion rings with zero drift velocity.

injected into the simulation domain or as initial value simulations. Figure 7.2 show the pickup ions scattering as anticipated.

- Due to the high plasma beta of Rhea's plasma environment, the first step is to adapt the hybrid simulations for nongyrotropic pickup ions within a Titan-like plasma environment where nongyrotropic pickup ions are also observed. These can then be used to examine the instability characteristics and the effects of a dϕ gradient.

- Examine the various magnetic field topologies and ambient conditions associated with the various plasma environments in which Titan can be situated [*Rymer et al.*, 2009]. Determine the pickup ion distributions during these various conditions and use these as inputs to the hybrid simulation code.

- Run an ensemble of simulations to determine when and where ICWs would be observed in the vicinity of Titan.

- Further examine the generation of this instability in the high plasma beta environment in Saturn's middle magnetosphere at Rhea's orbit. The competition between the the mirror and Alfvén-cyclotron modes are relevant to accurately characterising mass loading signatures.

Mirror mode structures have also been observed at various heliocentric distances, advecting with the accelerating solar wind war from their generation region in the solar corona. It has therefore been postulated that Alfvén-cyclotron instability might also be generated and contribute to coronal heating [*Russell et al.*, 2008]. Significant uncertainness also exist regarding the generation of this instability in the solar wind. The accurate characterisation of energy partitioning between the two instabilities could therefore yield insights far beyond the Saturnian system.

7.2.4 Non-uniform simulations

A surprisingly phenomenon regarding ICW characteristics in Saturn's magnetosphere is the unexplained latitudinal structure reported by *Leisner et al.* [2011]. Figure 7.3 shows this surprising trend, which shows the amplitudes surprisingly peaking away from the equator where the waves are generated. It therefore remains to be determined whether these waves undergo convective growth of whether this is simply a function of the latitudinal plasma and field variations.

To understand this phenomenon hybrid or particle-in-cell simulation codes are required to accurately reproduce such non-uniform conditions. To this end the following steps could be taken:

- Implement a Harris current sheet into hybrid simulation code and demonstrate that this plasma structure can be modelled in steady state.

- Inject pickup ions into the centre of this simulation domain and constrain the wave propagation characteristics structure within this non-uniform domain.

- Implement field and plasma gradients representative of the Saturnian magnetodisk, for example, as predicted by the magnetodisk model of *Achilleos et al.* [2010] and examine wave propagation through these gradients.

- Relate the simulation amplitudes to those in Saturn's magnetosphere to calculate global ionisation rates of Saturn's extended neutral cloud.

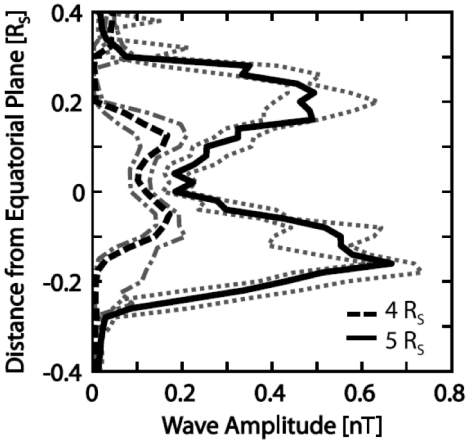

Figure 7.3: Vertical ICW amplitude structure in Saturn's inner magnetosphere.

- Apply this technique to the Jovian magnetodisk and to thus account for a dipole tilt. A similar study can be carried out as at Saturn, but with the wave polarisation as an added focus as oblique propagation angle polarisations might also occur due to the dipole tilt.

Bibliography

Ågren, K., N. J. T. Edberg, and J.-E. Wahlund (2012), Detection of negative ions in the deep ionosphere of Titan during the Cassini T70 flyby, *Geophysical Research Letters*, *39*, L10201, doi: 10.1029/2012GL051714.

Achilleos, N., P. Guio, and C. S. Arridge (2010), A model of force balance in Saturn's magnetodisc, *Monthly Notices of the Royal Astronomical Society*, *401*, 2349–2371, doi: 10.1111/j.1365-2966.2009.15865.x.

Agúndez, M., et al. (2010), Astronomical identification of CN^-, the smallest observed molecular anion, *Astronomy and Astrophysics*, *517*, L2, doi: 10.1051/0004-6361/201015186.

Alfvén, H. (1957), On the theory of comet tails., *Tellus*, *9*.

Ali, A., E. C. Sittler, D. Chornay, B. R. Rowe, and C. Puzzarini (2013), Cyclopropenyl cation - the simplest Huckel's aromatic molecule - and its cyclic methyl derivatives in Titan's upper atmosphere, *Planetary and Space Science*, *87*, 96–105, doi: 10.1016/j.pss.2013.07.007.

Ali, A., E. C. Sittler, D. Chornay, B. R. Rowe, and C. Puzzarini (2015), Organic chemistry in Titan's upper atmosphere and its astrobiological consequences: I. Views towards Cassini plasma spectrometer (CAPS) and ion neutral mass spectrometer (INMS) experiments in space, *Planetary and Space Science*, *109*, 46–63, doi: 10.1016/j.pss.2015.01.015.

Appleton, E. V., R. Naismith, and G. Builder (1933), Ionospheric Investigations in High Latitudes, *Nature*, *132*, 340–341, doi: 10.1038/132340a0.

Arn, G. A. (2009), Experimental studies of exotic negative ions, Ph.D. thesis, University of Tennessee, Knoxville.

Arnold, F., A. A. Viggiano, and E. E. Ferguson (1982), Combined mass spectrometric composition measurements of positive and negative ions in the lower ionosphere. II - Negative ions, *Planetary and Space Science*, *30*, 1307–1314, doi: 10.1016/0032-0633(82)90104-0.

Bagenal, F., et al. (2015), Plasma conditions at Europa's orbit, *Icarus*, *261*, 1–13, doi: 10.1016/j.icarus.2015.07.036.

Barabash, S., E. Dubinin, N. Pisarenko, R. Lundin, and C. T. Russell (1991), Picked-up protons near Mars - PHOBOS observations, *Geophysical Research Letters*, *18*, 1805–1808, doi: 10.1029/91GL02082.

Baragiola, R. A., E. V. Alonso, and A. O. Florio (1979), Electron emission from clean metal surfaces induced by low-energy light ions, *Phys. Rev. B*, *19*, 121–129, doi: 10.1103/PhysRevB.19.121.

Baumjohann, W., and R. A. Treumann (1996), *Basic space plasma physics*, doi: 10.1142/p015.

Berné, O., G. Mulas, and C. Joblin (2013), Interstellar C_{60}^+, *Astronomy and Astrophysics*, *550*, L4, doi: 10.1051/0004-6361/201220730.

Bertucci, C., et al. (2008), The Magnetic Memory of Titan's Ionized Atmosphere, *Science*, *321*, 1475, doi: 10.1126/science.1159780.

Bettens, R. P. A., and E. Herbst (1996), The Abundance of Very Large Hydrocarbons and Carbon Clusters in the Diffuse Interstellar Medium, *Astrophysical Journal Letters*, *468*, 686, doi: 10.1086/177726.

Bittencourt, J. A. (2004), *Fundamentals of Plasma Physics*, 3 ed., 711 pp., Pergamon, Amsterdam, doi: https://doi.org/10.1016/B978-0-08-033923-8.50005-7.

Borucki, W. J., R. C. Whitten, E. L. O. Bakes, E. Barth, and S. Tripathi (2006), Predictions of the electrical conductivity and charging of the aerosols in Titan's atmosphere, *Icarus*, *181*, 527–544, doi: 10.1016/j.icarus.2005.10.030.

Bradbury, N. E. (1938), Ionization, negative-ion formation, and recombination in the ionosphere, *Terrestrial Magnetism and Atmospheric Electricity*, *43*(1), 55–66, doi: 10.1029/TE043i001p00055.

Brinca, A. L., L. Borda de Agua, and D. Winske (1993), On the stability of nongyrotropic ion populations - A first (analytic and simulation) assessment, *Journal of Geophysical Research*, *98*, 7549–7560, doi: 10.1029/92JA01874.

Broadfoot, A. L., et al. (1979), Extreme ultraviolet observations from Voyager 1 encounter with Jupiter, *Science*, *204*, 979–982, doi: 10.1126/science.204.4396.979.

Broadfoot, A. L., et al. (1989), Ultraviolet spectrometer observations of Neptune and Triton, *Science*, *246*, 1459–1466, doi: 10.1126/science.246.4936.1459.

Brown, M. E., and K. P. Hand (2013), Salts and Radiation Products on the Surface of Europa, *Astrophysical Journal Letters*, *145*, 110, doi: 10.1088/0004-6256/145/4/110.

Brünken, S., H. Gupta, C. A. Gottlieb, M. C. McCarthy, and P. Thaddeus (2007), Detection of the Carbon Chain Negative Ion C_8H^- in TMC-1, *Astrophysical Journal Letters*, *664*, L43–L46, doi: 10.1086/520703.

Burch, J. L., T. E. Cravens, K. Llera, R. Goldstein, P. Mokashi, C.-Y. Tzou, and T. Broiles (2015), Charge exchange in cometary coma: Discovery of H^- ions in the solar wind close to comet 67P/Churyumov-Gerasimenko, *Geophysical Research Letters*, *42*, 5125–5131, doi: 10.1002/2015GL064504.

Burton, M. E., B. Buratti, D. L. Matson, and J.-P. Lebreton (2001), The Cassini/Huygens Venus and earth flybys: An overview of operations and results, *Journal of Geophysical Research*, *106*, 30,099–30,108, doi: 10.1029/2001JA900088.

Carlson, C. W., D. W. Curtis, G. Paschmann, and W. Michael (1982), An instrument for rapidly measuring plasma distribution functions with high resolution, *Advances in Space Research*, *2*, 67–70, doi: 10.1016/0273-1177(82)90151-X.

Carlson, R. W. (1999), A Tenuous Carbon Dioxide Atmosphere on Jupiter's Moon Callisto, *Science*, *283*, 820, doi: 10.1126/science.283.5403.820.

Cernicharo, J., M. Guélin, M. Agündez, K. Kawaguchi, M. McCarthy, and P. Thaddeus (2007), Astronomical detection of C_{4H^-}, the second interstellar anion, *Astronomy and Astrophysics*, *467*, L37–L40, doi: 10.1051/0004-6361:20077415.

Cernicharo, J., M. Guélin, M. Agúndez, M. C. McCarthy, and P. Thaddeus (2008), Detection of C_5N^- and Vibrationally Excited C_6H in IRC +10216, *Astrophysical Journal Letters*, *688*, L83, doi: 10.1086/595583.

Chaizy, P., et al. (1991), Negative ions in the coma of Comet Halley, *Nature*, *349*, 393–396, doi: 10.1038/349393a0.

Chandrasekhar, S., and M. K. Krogdahl (1943), On the Negative Hydrogen Ion and its Absorption Coefficient., *Astrophysical Journal Letters*, *98*, 205, doi: 10.1086/144561.

Chen, F. F. (1974), *Introduction to plasma physics*.

Chen, X., M. S. Westphall, and L. M. Smith (2003), Mass spectrometric analysis of dna mixtures: instrumental effects responsible for decreased sensitivity with increasing mass, *Analytical Chemistry*, *75*(21), 5944–5952, doi: 10.1021/ac030127h, pMID: 14588036.

Christon, S. P., D. C. Hamilton, J. M. C. Plane, D. G. Mitchell, R. D. DiFabio, and S. M. Krimigis (2015), Discovery of suprathermal Fe^+ in Saturn's magnetosphere, *Journal of Geophysical Research (Space Physics)*, *120*, 2720–2738, doi: 10.1002/2014JA020906.

Ciarniello, M., et al. (2011), Hapke modeling of rhea surface properties through cassini-vims spectra, *Icarus*, *214*(2), 541 – 555, doi: https://doi.org/10.1016/j.icarus.2011.05.010.

Clark, R. N., et al. (2008), Compositional mapping of Saturn's satellite Dione with Cassini VIMS and implications of dark material in the Saturn system, *Icarus*, *193*, 372–386, doi: 10.1016/j.icarus.2007.08.035.

Coates, A. J., A. D. Johnstone, B. Wilken, K. Jockers, and K.-H. Glassmeier (1989), Velocity space diffusion of pickup ions from the water group at Comet Halley, *Journal of Geophysical Research*, *94*, 9983–9993, doi: 10.1029/JA094iA08p09983.

Coates, A. J., A. D. Johnstone, B. Wilken, K. Jockers, and K.-H. Glassmeier (1990), Bulk properties and velocity distributions of water group ions at Comet Halley - Giotto measurements, *Journal of Geophysical Research*, *95*, 10,249–10,260, doi: 10.1029/JA095iA07p10249.

Coates, A. J., A. D. Johnstone, B. Wilken, and F. M. Neubauer (1993), Velocity space diffusion and nongyrotropy of pickup water group ions at comet Grigg-Skjellerup, *Journal of Geophysical Research*, *98*, 20, doi: 10.1029/93JA02535.

Coates, A. J., F. J. Crary, G. R. Lewis, D. T. Young, J. H. Waite, and E. C. Sittler (2007a), Discovery of heavy negative ions in Titan's ionosphere, *Geophysical Research Letters*, *34*, L22103, doi: 10.1029/2007GL030978.

Coates, A. J., F. J. Crary, D. T. Young, K. Szego, C. S. Arridge, Z. Bebesi, E. C. Sittler, R. E. Hartle, and T. W. Hill (2007b), Ionospheric electrons in Titan's tail: Plasma structure during the Cassini T9 encounter, *Geophysical Research Letters*, *34*, L24S05, doi: 10.1029/2007GL030919.

Coates, A. J., et al. (2008), Ionospheric photoelectrons at Venus: Initial observations by ASPERA-4 ELS, *Planetary and Space Science*, *56*, 802–806, doi: 10.1016/j.pss.2007.12.008.

Coates, A. J., A. Wellbrock, G. R. Lewis, G. H. Jones, D. T. Young, F. J. Crary, and J. H. Waite (2009), Heavy negative ions in Titan's ionosphere: Altitude and latitude dependence, *Planetary and Space Science*, *57*, 1866–1871, doi: 10.1016/j.pss.2009.05.009.

Coates, A. J., et al. (2010), Negative ions at Titan and Enceladus: recent results, *Faraday Discussions*, *147*, 293, doi: 10.1039/c004700g.

Coates, A. J., S. M. E. Tsang, A. Wellbrock, R. A. Frahm, J. D. Winningham, S. Barabash, R. Lundin, D. T. Young, and F. J. Crary (2011), Ionospheric photoelectrons: Comparing Venus, Earth, Mars and Titan, *Planetary and Space Science*, *59*, 1019–1027, doi: 10.1016/j.pss.2010.07.016.

Coates, A. J., et al. (2012), Cassini in Titan's tail: CAPS observations of plasma escape, *Journal of Geophysical Research (Space Physics)*, *117*, A05324, doi: 10.1029/2012JA017595.

Coates, A. J., A. Wellbrock, J. H. Waite, and G. H. Jones (2015), A new upper limit to the field-aligned potential near Titan, *Geophysical Research Letters*, *42*, 4676–4684, doi: 10.1002/2015GL064474.

Cobas, A., and W. E. Lamb (1944), On the extraction of electrons from a metal surface by ions and metastable atoms, *Phys. Rev.*, *65*, 327–337, doi: 10.1103/PhysRev.65.327.

Coletti, C., and N. Re (2012), High level theoretical study of binding and of the potential energy surface in benzene-hydride system, *Chemical Physics*, *398*, 168–175, doi: 10.1016/j.chemphys.2011.03.017.

Convery, P. D., D. Schriver, M. Ashour-Abdalla, and R. L. Richard (2002), Wave-particle interactions associated with nongyrotropic distribution functions: A hybrid simulation study, *Journal of Geophysical Research (Space Physics)*, *107*, 1013, doi: 10.1029/2001JA000160.

Cordiner, M. A., and S. B. Charnley (2014), Negative ion chemistry in the coma of comet 1P/Halley, *Meteoritics and Planetary Science*, *49*, 21–27, doi: 10.1111/maps.12082.

Cordiner, M. A., J. V. Buckle, E. S. Wirström, A. O. H. Olofsson, and S. B. Charnley (2013a), On the Ubiquity of Molecular Anions in the Dense Interstellar Medium, *Astrophysical Journal Letters*, *770*, 48, doi: 10.1088/0004-637X/770/1/48.

Cordiner, M. A., J. V. Buckle, E. S. Wirström, A. O. H. Olofsson, and S. B. Charnley (2013b), On the Ubiquity of Molecular Anions in the Dense Interstellar Medium, *Astrophysical Journal Letters*, *770*, 48, doi: 10.1088/0004-637X/770/1/48.

Cowee, M. M., R. J. Strangeway, C. T. Russell, and D. Winske (2006), One-dimensional hybrid simulations of planetary ion pickup: Techniques and verification, *Journal of Geophysical Research (Space Physics)*, *111*(A10), A12213, doi: 10.1029/2006JA011996.

Cowee, M. M., D. Winske, C. T. Russell, and R. J. Strangeway (2007), 1D hybrid simulations of planetary ion-pickup: Energy partition, *Geophysical Research Letters*, *34*, L02113, doi: 10.1029/2006GL028285.

Cowee, M. M., C. T. Russell, and R. J. Strangeway (2008), One-dimensional hybrid simulations of planetary ion pickup: Effects of variable plasma and pickup conditions, *Journal of Geophysical Research (Space Physics)*, *113*, A08220, doi: 10.1029/2008JA013066.

Cowee, M. M., N. Omidi, C. T. Russell, X. Blanco-Cano, and R. L. Tokar (2009), Determining ion production rates near Saturn's extended neutral cloud from ion cyclotron wave amplitudes, *Journal of Geophysical Research (Space Physics)*, *114*, A04219, doi: 10.1029/2008JA013664.

Crary, F. J., B. A. Magee, K. Mandt, J. H. Waite, J. Westlake, and D. T. Young (2009), Heavy ions, temperatures and winds in Titan's ionosphere: Combined Cassini CAPS and INMS observations, *Planetary and Space Science*, *57*, 1847–1856, doi: 10.1016/j.pss.2009.09.006.

Cravens, T. E., et al. (2006), Composition of Titan's ionosphere, *Geophysical Research Letters*, *33*, L07105, doi: 10.1029/2005GL025575.

Cravens, T. E., I. P. Robertson, S. A. Ledvina, D. Mitchell, S. M. Krimigis, and J. H. Waite (2008), Energetic ion precipitation at Titan, *Geophysical Research Letters*, *35*, L03103, doi: 10.1029/2007GL032451.

Cui, J., M. Galand, R. V. Yelle, J.-E. Wahlund, K. Ågren, J. H. Waite, and M. K. Dougherty (2010), Ion transport in Titan's upper atmosphere, *Journal of Geophysical Research (Space Physics)*, *115*, A06314, doi: 10.1029/2009JA014563.

Dalgarno, A., and R. A. McCray (1973), The Formation of Interstellar Molecules from Negative Ions, *Astrophysical Journal Letters*, *181*, 95–100, doi: 10.1086/152032.

Danielson, R. E., J. J. Caldwell, and D. R. Larach (1973), An Inversion in the Atmosphere of Titan, *Icarus*, *20*, 437–443, doi: 10.1016/0019-1035(73)90016-X.

Darwin, C. (1920), Li. the dynamical motions of charged particles, *Philosophical Magazine*, *39*(233), 537–551, doi: 10.1080/14786440508636066.

Delva, M., T. L. Zhang, M. Volwerk, Z. Vörös, and S. A. Pope (2008), Proton cyclotron waves in the solar wind at Venus, *Journal of Geophysical Research (Planets)*, *113*, E00B06, doi: 10.1029/2008JE003148.

Desai, R. T., et al. (2017a), Carbon chain anions and the growth of complex organic molecules in titans ionosphere, *The Astrophysical Journal Letters*, *844*(2), L18.

Desai, R. T., M. M. Cowee, H. Wei, X. Fu, S. P. Gary, M. Volwerk, and A. J. Coates (2017b), Hybrid simulations of positively and negatively charged pickup ions and cyclotron wave generation at europa, *Journal of Geophysical Research: Space Physics*, *122*(10), 10,408–10,420, doi: 10.1002/2017JA024479, 2017JA024479.

Dobrijevic, M., J. C. Loison, K. M. Hickson, and G. Gronoff (2016), 1D-coupled photochemical model of neutrals, cations and anions in the atmosphere of Titan, *Icarus*, *268*, 313–339, doi: 10.1016/j.icarus.2015.12.045.

Dong, Y., T. W. Hill, and S.-Y. Ye (2015), Characteristics of ice grains in the enceladus plume from cassini observations, *Journal of Geophysical Research: Space Physics*, *120*(2), 915–937, doi: 10.1002/2014JA020288, 2014JA020288.

Dougherty, M. K., K. K. Khurana, F. M. Neubauer, C. T. Russell, J. Saur, J. S. Leisner, and M. E. Burton (2006), Identification of a Dynamic Atmosphere at Enceladus with the Cassini Magnetometer, *Science*, *311*, 1406–1409, doi: 10.1126/science.1120985.

Dungey, J. W. (1961), Interplanetary Magnetic Field and the Auroral Zones, *Physical Review Letters*, *6*, 47–48, doi: 10.1103/PhysRevLett.6.47.

Eastwood, J. P., D. A. Brain, J. S. Halekas, J. F. Drake, T. D. Phan, M. Øieroset, D. L. Mitchell, R. P. Lin, and M. Acuña (2008), Evidence for collisionless magnetic reconnection at Mars, *Geophysical Research Letters*, *35*, L02106, doi: 10.1029/2007GL032289.

Fegley, B., and M. Y. Zolotov (2000), Chemistry of Sodium, Potassium, and Chlorine in Volcanic Gases on Io, *Icarus*, *148*, 193–210, doi: 10.1006/icar.2000.6490.

Feldman, P. D., T. B. Ake, A. F. Berman, H. W. Moos, D. J. Sahnow, D. F. Strobel, H. A. Weaver, and P. R. Young (2001), Detection of Chlorine Ions in the Far Ultraviolet Spectroscopic Explorer Spectrum of the Io Plasma Torus, *Astrophysical Journal Letters*, *554*, L123–L126, doi: 10.1086/320920.

Fenzlaff, H.-P., and E. Illenberger (1984), Low energy electron impact on benzene and the fluorobenzenes. Formation and dissociation of negative ions, *International Journal of Mass Spectrometry and Ion Processes*, *59*, 185–202, doi: 10.1016/0168-1176(84)85094-6.

Frahm, R. A., et al. (2006), Carbon dioxide photoelectron energy peaks at Mars, *Icarus*, *182*, 371–382, doi: 10.1016/j.icarus.2006.01.014.

Fraser, G. W. (2002), The ion detection efficiency of microchannel plates (MCPs), *International Journal of Mass Spectrometry*, *215*, 13–30, doi: 10.1016/S1387-3806(01)00553-X.

Fried, B. D., and S. D. Conte (1961), *The Plasma Dispersion Function*.

Friedrich, M., and M. Rapp (2009), News from the Lower Ionosphere: A Review of Recent Developments, *Surveys in Geophysics*, *30*, 525–559, doi: 10.1007/s10712-009-9074-2.

Fritzenwallner, J., and E. Kopp (1998), Model calculations of the negative ion chemistry in the mesosphere with special emphasis on the chlorine species and the formation of cluster ions, *Advances in Space Research*, *21*, 891–894, doi: 10.1016/S0273-1177(97)00649-2.

Fu, X., M. M. Cowee, V. K. Jordanova, S. P. Gary, G. D. Reeves, and D. Winske (2016), Predicting electromagnetic ion cyclotron wave amplitude from unstable ring current plasma conditions, *Journal of Geophysical Research (Space Physics)*, *121*(A10), 10, doi: 10.1002/2016JA023303.

Galand, M., R. V. Yelle, A. J. Coates, H. Backes, and J.-E. Wahlund (2006), Electron temperature of Titan's sunlit ionosphere, *Geophysical Research Letters*, *33*, L21101, doi: 10.1029/2006GL027488.

Galli, D., and F. Palla (2013), The Dawn of Chemistry, *Annual Review of Astronomy and Astrophysics*, *51*, 163–206, doi: 10.1146/annurev-astro-082812-141029.

Ganguly, S. (1984), Observations of large negative ion zones around 88 km, *Journal of Atmospheric and Terrestrial Physics*, *46*(8), 663 – 666, doi: https://doi.org/10.1016/0021-9169(84)90126-0.

Ganguly, S., J. D. Mathews, and C. A. Tepley (1979), Thomson scatter radar detection of d-region negative ions at arecibo, *Geophysical Research Letters*, *6*(2), 89–92, doi: 10.1029/GL006i002p00089.

Gary, S. P. (1993), *Theory of Space Plasma Microinstabilities*, 193 pp.

Gary, S. P., and C. D. Madland (1988), Electromagnetic ion instabilities in a cometary environment, *Journal of Geophysical Research*, *93*, 235–241, doi: 10.1029/JA093iA01p00235.

Gary, S. P., and D. Schriver (1987), The electromagnetic ion cyclotron beam anisotropy instability, *Planetary and Space Science*, *35*, 51–59, doi: 10.1016/0032-0633(87)90144-9.

Gary, S. P., K. Akimoto, and D. Winske (1989), Computer simulations of cometary-ion/ion instabilities and wave growth, *Journal of Geophysical Research*, *94*, 3513–3525, doi: 10.1029/JA094iA04p03513.

Gladstone, G. R., et al. (2016), The atmosphere of Pluto as observed by New Horizons, *Science*, *351*, aad8866, doi: 10.1126/science.aad8866.

Gong, Y., Z. Ma, Y. Li, Q. Zhou, S. Zhang, and C. Huang (2017), The effect of doppler broadening on d region negative ion ratio measurements at arecibo, *Journal of Geophysical Research: Space Physics*, *122*(5), 5816–5824, doi: 10.1002/2016JA023805, 2016JA023805.

Gurnett, D. A., et al. (2004), The Cassini Radio and Plasma Wave Investigation, *Space Science Reviews*, *114*, 395–463, doi: 10.1007/s11214-004-1434-0.

Hagstrum, H. D. (1977), low energy de-excitation and neutralization processes near surfaces, in *Inelastic IonSurface Collisions*, edited by N. TOLK, J. TULLY, W. HEILAND, and C. WHITE, pp. 1 – 25, Academic Press, doi: https://doi.org/10.1016/B978-0-12-703550-5.50006-6.

Haider, S. A. (1986), Some molecular nitrogen emission from Titan-solar EUV interaction, *Journal of Geophysical Research*, *91*, 8998–9000, doi: 10.1029/JA091iA08p08998.

Halekas, J. S., D. L. Mitchell, R. P. Lin, L. L. Hood, M. H. Acuña, and A. B. Binder (2002), Evidence for negative charging of the lunar surface in shadow, *Geophysical Research Letters*, *29*, 1435, doi: 10.1029/2001GL014428.

Hall, D. T., D. F. Strobel, P. D. Feldman, M. A. McGrath, and H. A. Weaver (1995), Detection of an oxygen atmosphere on Jupiter's moon Europa, *Nature*, *373*, 677–679, doi: 10.1038/373677a0.

Hall, D. T., P. D. Feldman, M. A. McGrath, and D. F. Strobel (1998), The Far-Ultraviolet Oxygen Airglow of Europa and Ganymede, *Astrophysical Journal Letters*, *499*, 475–481, doi: 10.1086/305604.

Hand, K. P., and R. W. Carlson (2015), Europa's surface color suggests an ocean rich with sodium chloride, *Geophysical Research Letters*, *42*, 3174–3178, doi: 10.1002/2015GL063559.

Harada, N., and E. Herbst (2008), Modeling Carbon Chain Anions in L1527, *Astrophysical Journal Letters*, *685*, 272-280, doi: 10.1086/590468.

Hartle, R. E., et al. (2006), Initial interpretation of Titan plasma interaction as observed by the Cassini plasma spectrometer: Comparisons with Voyager 1, *Planetary and Space Science*, *54*, 1211–1224, doi: 10.1016/j.pss.2006.05.029.

Hasegawa, A. (1969), Heating of the magnetospheric plasma by electromagnetic waves generated in the magnetosheath, *Journal of Geophysical Research*, *74*, 1763, doi: 10.1029/JA074i007p01763.

Herbst, E. (1981), Can negative molecular ions be detected in dense interstellar clouds, *Nature*, *289*, 656, doi: 10.1038/289656a0.

Hill, T. W., et al. (2012), Charged nanograins in the Enceladus plume, *Journal of Geophysical Research (Space Physics)*, *117*, A05209, doi: 10.1029/2011JA017218.

Huddleston, D. E., and A. D. Johnstone (1992), Relationship between wave energy and free energy from pickup ions in the Comet Halley environment, *Journal of Geophysical Research*, *97*, 12, doi: 10.1029/92JA00726.

Huddleston, D. E., R. J. Strangeway, J. Warnecke, C. T. Russell, M. G. Kivelson, and F. Bagenal (1997), Ion cyclotron waves in the Io torus during the Galileo encounter: Warm plasma dispersion analysis, *Geophysical Research Letters*, *24*, 2143, doi: 10.1029/97GL01203.

Huddleston, D. E., R. J. Strangeway, J. Warnecke, C. T. Russell, and M. G. Kivelson (1998), Ion cyclotron waves in the Io torus: Wave dispersion, free energy analysis, and $SO_2{}^+$ source rate estimates, *Journal of Geophysical Research*, *103*, 19,887–19,900, doi: 10.1029/97JE03557.

Hunten, D. M., M. G. Tomasko, F. M. Flasar, R. E. Samuelson, D. F. Strobel, and D. J. Stevenson (1984), *Titan*, pp. 671–759.

Hussmann, H., F. Sohl, and T. Spohn (2006), Subsurface oceans and deep interiors of medium-sized outer planet satellites and large trans-neptunian objects, *Icarus*, *185*(1), 258 – 273, doi: https://doi.org/10.1016/j.icarus.2006.06.005.

Inoue, Masao (1966), Ions ngatifs forms dans le cyanogne et lacide cyanhydrique*, *J. Chim. Phys.*, *63*, 1061–1071, doi: 10.1051/jcp/1966631061.

Irwin, P. G. J., et al. (2008), The NEMESIS planetary atmosphere radiative transfer and retrieval tool, *Journal of Quantitative Spectroscopy and Radiative Transfer*, *109*, 1136–1150, doi: 10.1016/j.jqsrt.2007.11.006.

Itikawa, Y. (2009), Cross Sections for Electron Collisions with Oxygen Molecules, *Journal of Physical and Chemical Reference Data*, *38*, 1–20, doi: 10.1063/1.3025886.

Jian, L. K., C. T. Russell, J. G. Luhmann, R. J. Strangeway, J. S. Leisner, and A. B. Galvin (2009), Ion Cyclotron Waves in the Solar Wind Observed by STEREO Near 1 AU, *Astrophysical Journal Letters*, *701*, L105–L109, doi: 10.1088/0004-637X/701/2/L105.

Johnson, C. Y., E. B. Meadows, and J. C. Holmes (1958), Ion composition of the arctic ionosphere, *Journal of Geophysical Research*, *63*(2), 443–444, doi: 10.1029/JZ063i002p00443.

Johnson, R. E. (1993), Sputtering of an atmosphere, *Trends in Geophys. Res.*, *2*, 501–513, doi: 10.1029/98GL02565.

Johnson, R. E., R. M. Killen, J. H. Waite, Jr., and W. S. Lewis (1998), Europa's surface composition and sputter-produced ionosphere, *Geophysical Research Letters*, *25*, 3257–3260, doi: 10.1029/98GL02565.

Johnson, R. E., M. H. Burger, T. A. Cassidy, F. Leblanc, M. Marconi, and W. H. Smyth (2009), *Composition and Detection of Europa's Sputter-induced Atmosphere*, p. 507.

Johnstone, A. D. (1988), *Observations of the Interaction between Comet Halley and the Solar Wind by the Giotto Spacecraft*, p. 110.

Johnstone, A. D., et al. (1997), Peace: a Plasma Electron and Current Experiment, *Space Science Reviews*, *79*, 351–398, doi: 10.1023/A:1004938001388.

Jones, G. H., and A. J. Coates (2014), Observations of negatively-charged particles near Saturn's Main Rings during Saturn Orbit Insertion, *European Planetary Science Congress 2014, EPSC Abstracts, Vol. 9, id. EPSC2014-623*, *9*, EPSC2014-623.

Jones, G. H., et al. (2009), Fine jet structure of electrically charged grains in Enceladus' plume, *Geophysical Research Letters*, *36*, L16204, doi: 10.1029/2009GL038284.

Jones, G. H., A. J. Coates, and A. Wellbrock (2011), Negative ion flow at Titan, *AGU Fall Meeting Abstracts*.

Jurac, S., and J. D. Richardson (2005), A self-consistent model of plasma and neutrals at Saturn: Neutral cloud morphology, *Journal of Geophysical Research (Space Physics)*, *110*, A09220, doi: 10.1029/2004JA010635.

Khurana, K. K., M. G. Kivelson, D. J. Stevenson, G. Schubert, C. T. Russell, R. J. Walker, and C. Polanskey (1998), Induced magnetic fields as evidence for subsurface oceans in Europa and Callisto, *Nature*, *395*, 777–780, doi: 10.1038/27394.

Khurana, K. K., C. T. Russell, and M. K. Dougherty (2008), Magnetic portraits of Tethys and Rhea, *Icarus*, *193*, 465–474, doi: 10.1016/j.icarus.2007.08.005.

Khurana, K. K., S. Fatemi, J. Lindkvist, E. Roussos, N. Krupp, M. Holmström, C. T. Russell, and M. K. Dougherty (2017), The role of plasma slowdown in the generation of Rhea's Alfvén wings, *Journal of Geophysical Research (Space Physics)*, *122*, 1778–1788, doi: 10.1002/2016JA023595.

Kishinevsky, L. M. (1973), Estimation of electron potential emission yield dependence on metal and ion parameters, *Radiation Effects*, *19*(1), 23–27, doi: 10.1080/00337577308232211.

Kivelson, M. G., and C. T. Russell (1995), *Introduction to Space Physics*, 586 pp.

Kivelson, M. G., K. K. Khurana, R. J. Walker, C. T. Russell, J. A. Linker, D. J. Southwood, and C. Polanskey (1996), A Magnetic Signature at Io: Initial Report from the Galileo Magnetometer, *Science*, *273*, 337–340, doi: 10.1126/science.273.5273.337.

Kivelson, M. G., K. K. Khurana, C. T. Russell, M. Volwerk, R. J. Walker, and C. Zimmer (2000), Galileo Magnetometer Measurements: A Stronger Case for a Subsurface Ocean at Europa, *Science*, *289*, 1340–1343, doi: 10.1126/science.289.5483.1340.

Kivelson, M. G., K. K. Khurana, and M. Volwerk (2009), *Europa's Interaction with the Jovian Magnetosphere*, p. 545.

Küppers, M., and N. M. Schneider (2000), Discovery of chlorine in the Io torus, *Geophysical Research Letters*, *27*, 513–516, doi: 10.1029/1999GL010718.

Kurth, W. S., D. A. Gurnett, A. M. Persoon, A. Roux, S. J. Bolton, and C. J. Alexander (2001), The plasma wave environment of Europa, *Planetary and Space Science*, *49*, 345–363, doi: 10.1016/S0032-0633(00)00156-2.

Larmor, J. (1919), How could a rotating body such as the Sun become a magnet?, *Report of the British Association for the Advancement of Science*, *87th Meeting*, 159–160.

Lavvas, P., et al. (2013), Aerosol growth in titans ionosphere, *Proceedings of the National Academy of Sciences*, *110*(8), 2729–2734, doi: 10.1073/pnas.1217059110.

Le, G., X. Blanco-Cano, C. T. Russell, X.-W. Zhou, F. Mozer, K. J. Trattner, S. A. Fuselier, and B. J. Anderson (2001), Electromagnetic ion cyclotron waves in the high altitude cusp: Polar observations, *Journal of Geophysical Research*, *106*, 19,067–19,080, doi: 10.1029/2000JA900163.

Ledvina, S. A., and S. H. Brecht (2012), Consequences of negative ions for Titan's plasma interaction, *Geophysical Research Letters*, *39*, L20103, doi: 10.1029/2012GL053835.

Leisner, J. S., C. T. Russell, M. K. Dougherty, X. Blanco-Cano, R. J. Strangeway, and C. Bertucci (2006), Ion cyclotron waves in Saturn's E ring: Initial Cassini observations, *Geophysical Research Letters*, *33*, L11101, doi: 10.1029/2005GL024875.

Leisner, J. S., C. T. Russell, H. Y. Wei, and M. K. Dougherty (2011), Probing Saturn's ion cyclotron waves on high-inclination orbits: Lessons for wave generation, *Journal of Geophysical Research (Space Physics)*, *116*, A09235, doi: 10.1029/2011JA016555.

Lepp, S., and A. Dalgarno (1988), Polycyclic aromatic hydrocarbons in interstellar chemistry, *Astrophysical Journal Letters*, *324*, 553–556, doi: 10.1086/165915.

Lewis, G. R., N. André, C. S. Arridge, A. J. Coates, L. K. Gilbert, D. R. Linder, and A. M. Rymer (2008), Derivation of density and temperature from the Cassini Huygens CAPS electron spectrometer, *Planetary and Space Science*, *56*, 901–912, doi: 10.1016/j.pss.2007.12.017.

Lifshitz, Y., S. R. Kasi, J. W. Rabalais, and W. Eckstein (1990), Subplantation model for film growth from hyperthermal species, *Phys. Rev. B*, *41*, 10,468–10,480, doi: 10.1103/PhysRevB.41.10468.

Linder, D. R., A. J. Coates, R. D. Woodliffe, C. Alsop, A. D. Johnstone, M. Grande, A. Preece, B. Narheim, and D. T. Young (1998), The Cassini CAPS Electron Spectrometer, *Washington DC American Geophysical Union Geophysical Monograph Series*, *102*, 257.

Lindgren, E. B., B. Stamm, H.-K. Chan, Y. Maday, A. J. Stace, and E. Besley (2017), The effect of like-charge attraction on aerosol growth in the atmosphere of Titan, *Icarus*, *291*, 245–253, doi: 10.1016/j.icarus.2016.12.013.

Macquorn Rankine, W. J. (1870), On the Thermodynamic Theory of Waves of Finite Longitudinal Disturbance, *Philosophical Transactions of the Royal Society of London Series I*, *160*, 277–288.

Martens, H. R., D. B. Reisenfeld, J. D. Williams, R. E. Johnson, and H. T. Smith (2008), Observations of molecular oxygen ions in Saturn's inner magnetosphere, *Geophysical Research Letters*, *35*, L20103, doi: 10.1029/2008GL035433.

Martyn, D. F., and O. O. Pulley (1936), The Temperatures and Constituents of the Upper Atmosphere, *Proceedings of the Royal Society of London Series A*, *154*, 455–486, doi: 10.1098/rspa.1936.0062.

Massey, H. (1976), *Negative ions.*

Massey, H. S. W. (1930), The theory of the extraction of electrons from metals by positive ions and metastable atoms, *Mathematical Proceedings of the Cambridge Philosophical Society*, *26*(3), 386401, doi: 10.1017/S030500410001611X.

Massey, H. S. W. (1937), Dissociation, Recombination and Attachment Processes in the Upper Atmosphere. I, *Proceedings of the Royal Society of London Series A*, *163*, 542–553, doi: 10.1098/rspa.1937.0243.

May, O., J. Fedor, B. C. Ibănescu, and M. Allan (2008), Absolute cross sections for dissociative electron attachment to acetylene and diacetylene, *Phys. Rev. A*, *77*, 040,701, doi: 10.1103/PhysRevA.77.040701.

McCarthy, M. C., C. A. Gottlieb, H. Gupta, and P. Thaddeus (2006), Laboratory and astronomical identification of the negative molecular ion c6h, *The Astrophysical Journal Letters*, *652*(2), L141.

McCord, T. B., et al. (1998), Non-water-ice constituents in the surface material of the icy Galilean satellites from the Galileo near-infrared mapping spectrometer investigation, *Journal of Geophysical Research*, *103*, 8603–8626, doi: 10.1029/98JE00788.

McDowell, M. R. C. (1961), On the formation of H2 in H I regions, *The Observatory*, *81*, 240–243.

McGrath, M. A., R. E. Johnson, and L. J. Lanzerotti (1986), Sputtering of sodium on the planet Mercury, *Nature*, *323*, 694–696, doi: 10.1038/323694a0.

Means, J. D. (1972), Use of the three-dimensional covariance matrix in analyzing the polarization properties of plane waves, *Journal of Geophysical Research*, *77*(28), 5551–5559, doi: 10.1029/JA077i028p05551.

Meeks, Z., S. Simon, and S. Kabanovic (2016), A comprehensive analysis of ion cyclotron waves in the equatorial magnetosphere of Saturn, *Planetary and Space Science*, *129*, 47–60, doi: 10.1016/j.pss.2016.06.003.

Michael, M., S. N. Tripathi, P. Arya, A. Coates, A. Wellbrock, and D. T. Young (2011), High-altitude charged aerosols in the atmosphere of Titan, *Planetary and Space Science*, *59*, 880–885, doi: 10.1016/j.pss.2011.03.010.

Millar, T. J., E. Herbst, and R. P. A. Bettens (2000), Large molecules in the envelope surrounding IRC+10216, *Monthly Notices of the Royal Astronomical Society*, *316*, 195–203, doi: 10.1046/j.1365-8711.2000.03560.x.

Millar, T. J., C. Walsh, and T. A. Field (2017), Negative ions in space, *Chemical Reviews*, *117*(3), 1765–1795, doi: 10.1021/acs.chemrev.6b00480, pMID: 28112897.

Miller, S. L., and H. C. Urey (1959), Organic Compound Synthesis on the Primitive Earth, *Science*, *130*, 245–251, doi: 10.1126/science.130.3370.245.

Mumma, M. J., and S. B. Charnley (2011), The Chemical Composition of Comets: Emerging Taxonomies and Natal Heritage, *Annual Review of Astronomy and Astrophysics*, *49*, 471–524, doi: 10.1146/annurev-astro-081309-130811.

Narcisi, R. S., A. D. Bailey, L. Della Lucca, C. Sherman, and D. M. Thomas (1971), Mass spectrometric measurements of negative ions in the D- and lower E-regions, *Journal of Atmospheric and Terrestrial Physics*, *33*, 1147, doi: 10.1016/0021-9169(71)90102-4.

Ness, N. F., M. H. Acuna, and K. W. Behannon (1982), The induced magnetosphere of Titan, *Journal of Geophysical Research*, *87*, 1369–1381, doi: 10.1029/JA087iA03p01369.

Neubauer, F. M. (1998), The sub-Alfvénic interaction of the Galilean satellites with the Jovian magnetosphere, *Journal of Geophysical Research*, *103*, 19,843–19,866, doi: 10.1029/97JE03370.

Neubauer, F. M. (1999), Alfvén wings and electromagnetic induction in the interiors: Europa and Callisto, *Journal of Geophysical Research*, *104*, 28,671–28,684, doi: 10.1029/1999JA900217.

Niemann, H. B., et al. (2005), The abundances of constituents of Titan's atmosphere from the GCMS instrument on the Huygens probe, *Nature*, *438*, 779–784, doi: 10.1038/nature04122.

Nordheim, T. A., et al. (2014), Detection of a strongly negative surface potential at Saturn's moon Hyperion, *Geophysical Research Letters*, *41*, 7011–7018, doi: 10.1002/2014GL061127.

Olah, G. A. (1972), Stable carbocations. cxviii. general concept and structure of carbocations based on differentiation of trivalent (classical) carbenium ions from three-center bound penta- of tetracoordinated (nonclassical) carbonium ions. role of carbocations in electrophilic reactions, *Journal of the American Chemical Society*, *94*(3), 808–820, doi: 10.1021/ja00758a020.

Olah, G. A., T. Mathew, G. K. S. Prakash, and G. Rasul (2016), Chemical aspects of astrophysically observed extraterrestrial methanol, hydrocarbon derivatives, and ions, *Journal of the American Chemical Society*, *138*(5), 1717–1722, doi: 10.1021/jacs.6b00343, pMID: 26760052.

Oliphant, M. L. E., and P. B. Moon (1930), The liberation of electrons from metal surfaces by positive ions. part ii. theoretical, *Proceedings of the Royal Society of London. Series A, Containing Papers of a Mathematical and Physical Character*, *127*(805), 388–406.

Omidi, N., R. M. Thorne, and J. Bortnik (2010), Nonlinear evolution of EMIC waves in a uniform magnetic field: 1. Hybrid simulations, *Journal of Geophysical Research (Space Physics)*, *115*(A14), A12241, doi: 10.1029/2010JA015607.

Osepian, A., S. Kirkwood, and P. Dalin (2009), The influence of ozone concentration on the lower ionosphere; modelling and measurements during the 29-30 october 2003 solar proton event, *Annales Geophysicae*, *27*(2), 577–589, doi: 10.5194/angeo-27-577-2009.

Page, T. L. (1938), Kramers' Absorption Law in Astrophysical Problems, *Nature*, *141*, 1137, doi: 10.1038/1411137a0.

Parker, E. N. (1955), Hydromagnetic Dynamo Models., *Astrophysical Journal Letters*, *122*, 293, doi: 10.1086/146087.

Parker, E. N. (1958), Dynamics of the Interplanetary Gas and Magnetic Fields., *Astrophysical Journal Letters*, *128*, 664, doi: 10.1086/146579.

Pavlov, A. V. (2014), Photochemistry of ions at d-region altitudes of the ionosphere: A review, *Surveys in Geophysics*, *35*(2), 259–334, doi: 10.1007/s10712-013-9253-z.

Peko, B. L., and T. M. Stephen (2000), Absolute detection efficiencies of low energy H, H^-, H^+, H_2^+ and H_3^+ incident on a multichannel plate detector, *Nuclear Instruments and Methods in Physics Research B*, *171*, 597–604, doi: 10.1016/S0168-583X(00)00306-2.

Petkaki, P., and M. K. Dougherty (2001), ULF wave observations in Jupiter's magnetosphere, *Advances in Space Research*, *28*, 909–914, doi: 10.1016/S0273-1177(01)00517-8.

Petrie, S., and E. Herbst (1997), Some Interstellar Reactions Involving Electrons and Neutral Species: Attachment and Isomerization, *Astrophysical Journal Letters*, *491*, 210–215, doi: 10.1086/304941.

Poppe, A. R., R. Samad, J. S. Halekas, M. Sarantos, G. T. Delory, W. M. Farrell, V. Angelopoulos, and J. P. McFadden (2012), ARTEMIS observations of lunar pick-up ions in the terrestrial magnetotail lobes, *Geophysical Research Letters*, *39*, L17104, doi: 10.1029/2012GL052909.

Prasad, R., F. Abicht, M. Borghesi, J. Braenzel, P. V. Nickles, G. Priebe, M. Schnürer, and S. Ter-Avetisyan (2013), Thomson spectrometer-microchannel plate assembly calibration for MeV-range positive and negative ions, and neutral atoms, *Review of Scientific Instruments*, *84*(5), 053302-053302-6, doi: 10.1063/1.4803670.

Rauch, J. L., and A. Roux (1982), Ray tracing of ulf waves in a multicomponent magnetospheric plasma: Consequences for the generation mechanism of ion cyclotron waves, *Journal of Geophysical Research: Space Physics*, *87*(A10), 8191–8198, doi: 10.1029/JA087iA10p08191.

Reasoner, D. L., and W. J. Burke (1972), Characteristics of the lunar photoelectron layer in the geomagnetic tail, *Journal of Geophysical Research*, *77*, 6671, doi: 10.1029/JA077i034p06671.

Regoli, L. H., A. J. Coates, M. F. Thomsen, G. H. Jones, E. Roussos, J. H. Waite, N. Krupp, and G. Cox (2016), Survey of pickup ion signatures in the vicinity of Titan using CAPS/IMS, *Journal of Geophysical Research (Space Physics)*, *121*, 8317–8328, doi: 10.1002/2016JA022617.

Remya, B., R. V. Reddy, B. T. Tsurutani, G. S. Lakhina, and E. Echer (2013), Ion temperature anisotropy instabilities in planetary magnetosheaths, *Journal of Geophysical Research (Space Physics)*, *118*, 785–793, doi: 10.1002/jgra.50091.

Roberts, P. H. (1987), *Dynamo Theory*, pp. 73–133, Springer Netherlands, Dordrecht, doi: 10.1007/978-94-009-4778-8_5.

Rodríguez-Martínez, M., X. Blanco-Cano, C. T. Russell, J. S. Leisner, R. J. Wilson, and M. K. Dougherty (2010), Harmonic growth of ion-cyclotron waves in Saturn's magnetosphere, *Journal of Geophysical Research (Space Physics)*, *115*, A09207, doi: 10.1029/2009JA015000.

Roussos, E., et al. (2008), Plasma and fields in the wake of Rhea: 3-D hybrid simulation and comparison with Cassini data, *Annales Geophysicae*, *26*, 619–637, doi: 10.5194/angeo-26-619-2008.

Roussos, E., et al. (2012), Energetic electron observations of Rhea's magnetospheric interaction, *Icarus*, *221*, 116–134, doi: 10.1016/j.icarus.2012.07.006.

Russell, C. T., and O. Vaisberg (1983), *The interaction of the solar wind with Venus*, pp. 873–940.

Russell, C. T., J. S. Leisner, C. S. Arridge, M. K. Dougherty, and X. Blanco-Cano (2006), Nature of magnetic fluctuations in Saturn's middle magnetosphere, *Journal of Geophysical Research (Space Physics)*, *111*(A10), A12205, doi: 10.1029/2006JA011921.

Russell, C. T., L. K. Jian, J. G. Luhmann, T. L. Zhang, F. M. Neubauer, R. M. Skoug, X. Blanco-Cano, N. Omidi, and M. M. Cowee (2008), Mirror mode waves: Messengers from the coronal heating region, *Geophysical Research Letters*, *35*, L15101, doi: 10.1029/2008GL034096.

Rymer, A. M. (2004), Analysis of Cassini plasma and magnetic field measurements from 1-7 AU, Ph.D. thesis, University of London, University College London (United Kingdom.

Rymer, A. M., A. J. Coates, K. Svenes, G. A. Abel, D. R. Linder, B. Narheim, M. Thomsen, and D. T. Young (2001), Cassini plasma spectrometer electron spectrometer measurements during the Earth swing-by on August 18, 1999, *Journal of Geophysical Research*, *106*, 30,177–30,198, doi: 10.1029/2001JA900087.

Rymer, A. M., H. T. Smith, A. Wellbrock, A. J. Coates, and D. T. Young (2009), Discrete classification and electron energy spectra of Titan's varied magnetospheric environment, *Geophysical Research Letters*, *36*, L15109, doi: 10.1029/2009GL039427.

Sagan, C., and B. N. Khare (1979), Tholins - Organic chemistry of interstellar grains and gas, *Nature*, *277*, 102–107, doi: 10.1038/277102a0.

Saito, Y., T. Mukai, M. Hirahara, S. Machida, A. Nishida, T. Terasawa, S. Kokubun, and T. Yamamoto (1994), GEOTAIL observation of ring-shaped ion distribution functions in the plasma sheet-lobe boundary, *Geophysical Research Letters*, *21*, 2999–3002, doi: 10.1029/94GL02099.

Saito, Y., et al. (2008), Solar wind proton reflection at the lunar surface: Low energy ion measurement by MAP-PACE onboard SELENE (KAGUYA), *Geophysical Research Letters*, *35*, L24205, doi: 10.1029/2008GL036077.

Santolík, O., et al. (2011), Intense plasma wave emissions associated with Saturn's moon Rhea, *Geophysical Research Letters*, *38*, L19204, doi: 10.1029/2011GL049219.

Sarre, P. J. (1980), On the possible detection of negative ions in the interstellar medium., *Journal de Chimie Physique*, *77*, 769–771, doi: 10.1051/jcp/1980770769.

Schenk, P., D. P. Hamilton, R. E. Johnson, W. B. McKinnon, C. Paranicas, J. Schmidt, and M. R. Showalter (2011), Plasma, plumes and rings: Saturn system dynamics as recorded in global color patterns on its midsize icy satellites, *Icarus*, *211*, 740–757, doi: 10.1016/j.icarus.2010.08.016.

Schippers, P., N. André, R. E. Johnson, M. Blanc, I. Dandouras, A. J. Coates, S. M. Krimigis, and D. T. Young (2009), Identification of photoelectron energy peaks in Saturn's inner neutral torus, *Journal of Geophysical Research (Space Physics)*, *114*, A12212, doi: 10.1029/2009JA014368.

Schrijver, C. J., and G. L. Siscoe (2012), *Heliophysics: Evolving Solar Activity and the Climates of Space and Earth*.

Schulte, P., and F. Arnold (1992), Detection of upper atmospheric negatively charged microclusters by a rocket-borne mass spectrometer, *Geophysical Research Letters*, *19*, 2297–2300, doi: 10.1029/92GL02631.

Schwenn, R., and E. Marsch (1991), *Physics of the Inner Heliosphere II. Particles, Waves and Turbulence.*, 152 pp.

Schwingenschuh, K., et al. (1992), The Martian magnetic field environment - Induced or dominated by an intrinsic magnetic field?, *Advances in Space Research*, *12*, 213–219, doi: 10.1016/0273-1177(92)90333-S.

Scipioni, F., F. Tosi, K. Stephan, G. Filacchione, M. Ciarniello, F. Capaccioni, and P. Cerroni (2014), Spectroscopic classification of icy satellites of Saturn II: Identification of terrain units on Rhea, *Icarus*, *234*, 1–16, doi: 10.1016/j.icarus.2014.02.010.

Shebanits, O., J.-E. Wahlund, K. Mandt, K. Ågren, N. J. T. Edberg, and J. H. Waite (2013), Negative ion densities in the ionosphere of Titan-Cassini RPWS/LP results, *Planetary and Space Science*, *84*, 153–162, doi: 10.1016/j.pss.2013.05.021.

Shebanits, O., et al. (2016), Ion and aerosol precursor densities in Titan's ionosphere: A multi-instrument case study, *Journal of Geophysical Research (Space Physics)*, *121*(A10), 10, doi: 10.1002/2016JA022980.

Shekhter, S. S. (1937), Neutralization of positive ions and the emission of secondary electrons, *J. Exp. Theor. Phys.*, *7*, 1, doi: ..

Shemansky, D. E., Y. L. Yung, X. Liu, J. Yoshii, C. J. Hansen, A. R. Hendrix, and L. W. Esposito (2014), A New Understanding of the Europa Atmosphere and Limits on Geophysical Activity, *Astrophysical Journal Letters*, *797*, 84, doi: 10.1088/0004-637X/797/2/84.

Shukla, P. K., and A. A. Mamun (2002), *Introduction to dusty plasma physics*.

Simon, S., H. Kriegel, J. Saur, A. Wennmacher, F. M. Neubauer, E. Roussos, U. Motschmann, and M. K. Dougherty (2012), Analysis of Cassini magnetic field observations over the poles of Rhea, *Journal of Geophysical Research (Space Physics)*, *117*, A07211, doi: 10.1029/2012JA017747.

Sittler, E. C., A. Ali, J. F. Cooper, R. E. Hartle, R. E. Johnson, A. J. Coates, and D. T. Young (2009), Heavy ion formation in Titan's ionosphere: Magnetospheric introduction of free oxygen and a source of Titan's aerosols?, *Planetary and Space Science*, *57*, 1547–1557, doi: 10.1016/j.pss.2009.07.017.

Spahn, F., et al. (2006), Cassini Dust Measurements at Enceladus and Implications for the Origin of the E Ring, *Science*, *311*, 1416–1418, doi: 10.1126/science.1121375.

Stephan, K., et al. (2010), Dione's spectral and geological properties, *Icarus*, *206*, 631–652, doi: 10.1016/j.icarus.2009.07.036.

Stephan, K., et al. (2012), The saturnian satellite rhea as seen by cassini vims, *Planetary and Space Science*, *61*(1), 142 – 160, doi: https://doi.org/10.1016/j.pss.2011.07.019, surfaces, atmospheres and magnetospheres of the outer planets and their satellites and ring systems: Part VII.

Stephen, T. M., and B. L. Peko (2000), Absolute calibration of a multichannel plate detector for low energy o, o, and o+, *Review of Scientific Instruments*, *71*(3), 1355–1359, doi: 10.1063/1.1150462.

Sternglass, E. J. (1957), Theory of secondary electron emission by high-speed ions, *Phys. Rev.*, *108*, 1–12, doi: 10.1103/PhysRev.108.1.

Stix, T. H. (1992), *Waves in plasmas*.

SWRI (2018), `https://eoportal.org/web/eoportal/satellite-missions/content/-/article/mms-observatory`, accessed April 2018.

Tang, K. B. K., R. Azria, Y. Le Coat, M. Tronc, and R. E. Palmer (1996), O- esd from o2 monolayers physisorbed on graphite: a surface mediated mechanism, *Zeitschrift für Physik D Atoms, Molecules and Clusters*, *38*(1), 41–44, doi: 10.1007/s004600050061.

Taylor, S. A., et al. (2018), Modeling, analysis, and interpretation of photoelectron energy spectra at enceladus observed by cassini, *Journal of Geophysical Research: Space Physics*, *123*(1), 287–296, doi: 10.1002/2017JA024536, 2017JA024536.

Teolis, B. D., and J. H. Waite (2016), Dione and Rhea seasonal exospheres revealed by Cassini CAPS and INMS, *Icarus*, *272*, 277–289, doi: 10.1016/j.icarus.2016.02.031.

Teolis, B. D., et al. (2010), Cassini Finds an Oxygen-Carbon Dioxide Atmosphere at Saturns Icy Moon Rhea, *Science*, *330*, 1813, doi: 10.1126/science.1198366.

Tepley, C. A., J. D. Mathews, and S. Ganguly (1981), Incoherent scatter radar studies of mesospheric temperatures and collision frequencies at arecibo, *Journal of Geophysical Research: Space Physics*, *86*(A13), 11,330–11,334, doi: 10.1029/JA086iA13p11330.

Terzieva, R., and E. Herbst (2000), Radiative electron attachment to small linear carbon clusters and its significance for the chemistry of diffuse interstellar clouds., *International Journal of Mass Spectrometry*, *201*, 135–142, doi: 10.1016/S1387-3806(00)00212-8.

Thaddeus, P., C. A. Gottlieb, H. Gupta, S. Brünken, M. C. McCarthy, M. Agúndez, M. Guélin, and J. Cernicharo (2008), Laboratory and Astronomical Detection of the Negative Molecular Ion C_3N^-, *Astrophysical Journal Letters*, *677*, 1132-1139, doi: 10.1086/528947.

Thorne, R. M., and B. T. Tsurutani (1987), Resonant interactions between cometary ions and low frequency electromagnetic waves, *Planetary and Space Science*, *35*, 1501–1511, doi: 10.1016/0032-0633(87)90076-6.

Tokar, R. L., et al. (2008), Cassini detection of water-group pick-up ions in the Enceladus torus, *Geophysical Research Letters*, *35*, L14202, doi: 10.1029/2008GL034749.

Tokar, R. L., R. E. Johnson, M. F. Thomsen, E. C. Sittler, A. J. Coates, R. J. Wilson, F. J. Crary, D. T. Young, and G. H. Jones (2012), Detection of exospheric $O_2{}^+$ at Saturn's moon Dione, *Geophysical Research Letters*, *39*, L03105, doi: 10.1029/2011GL050452.

Tortora, P., M. Zannoni, D. Hemingway, F. Nimmo, R. A. Jacobson, L. Iess, and M. Parisi (2016), Rhea gravity field and interior modeling from Cassini data analysis, *Icarus*, *264*, 264–273, doi: 10.1016/j.icarus.2015.09.022.

Trainer, M. G., J. A. Sebree, Y. H. Yoon, and M. A. Tolbert (2013), The Influence of Benzene as a Trace Reactant in Titan Aerosol Analogs, *Astrophysical Journal Letters*, *766*, L4, doi: 10.1088/2041-8205/766/1/L4.

Unsöld, A. (1939), Über die Stärke einiger Seriengrenzkontinua im Spektrum der Sonne. Mit 1 Abbildung., *Zeitschrift fuer Astrophysik*, *17*, 1.

Vasyliunas, V. M. (1983), *Plasma distribution and flow*, pp. 395–453.

Verronen, P. T., A. SeppäLä, M. A. Clilverd, C. J. Rodger, E. KyröLä, C.-F. Enell, T. Ulich, and E. Turunen (2005), Diurnal variation of ozone depletion during the October-November 2003 solar proton events, *Journal of Geophysical Research (Space Physics)*, *110*, A09S32, doi: 10.1029/2004JA010932.

Vervack, R. J., B. R. Sandel, and D. F. Strobel (2004), New perspectives on Titan's upper atmosphere from a reanalysis of the Voyager 1 UVS solar occultations, *Icarus*, *170*, 91–112, doi: 10.1016/j.icarus.2004.03.005.

Volwerk, M., M. G. Kivelson, and K. K. Khurana (2001), Wave activity in Europa's wake: Implications for ion pickup, *Journal of Geophysical Research*, *106*, 26,033–26,048, doi: 10.1029/2000JA000347.

Vuitton, V., R. V. Yelle, and M. J. McEwan (2007), Ion chemistry and N-containing molecules in Titan's upper atmosphere, *Icarus*, *191*, 722–742, doi: 10.1016/j.icarus.2007.06.023.

Vuitton, V., R. V. Yelle, and J. Cui (2008), Formation and distribution of benzene on Titan, *Journal of Geophysical Research (Planets)*, *113*, E05007, doi: 10.1029/2007JE002997.

Vuitton, V., P. Lavvas, R. V. Yelle, M. Galand, A. Wellbrock, G. R. Lewis, A. J. Coates, and J.-E. Wahlund (2009a), Negative ion chemistry in Titan's upper atmosphere, *Planetary and Space Science*, *57*, 1558–1572, doi: 10.1016/j.pss.2009.04.004.

Vuitton, V., R. V. Yelle, and P. Lavvas (2009b), Composition and chemistry of Titan's thermosphere and ionosphere, *Philosophical Transactions of the Royal Society of London Series A*, *367*, 729–741, doi: 10.1098/rsta.2008.0233.

Wahlund, J.-E., et al. (2005), Cassini Measurements of Cold Plasma in the Ionosphere of Titan, *Science*, *308*, 986–989, doi: 10.1126/science.1109807.

Wahlund, J.-E., et al. (2009), On the amount of heavy molecular ions in Titan's ionosphere, *Planetary and Space Science*, *57*, 1857–1865, doi: 10.1016/j.pss.2009.07.014.

Waite, J. H., et al. (2005), Ion Neutral Mass Spectrometer Results from the First Flyby of Titan, *Science*, *308*, 982–986, doi: 10.1126/science.1110652.

Waite, J. H., D. T. Young, T. E. Cravens, A. J. Coates, F. J. Crary, B. Magee, and J. Westlake (2007), The Process of Tholin Formation in Titan's Upper Atmosphere, *Science*, *316*, 870, doi: 10.1126/science.1139727.

Walsh, C., N. Harada, E. Herbst, and T. J. Millar (2009), The Effects of Molecular Anions on the Chemistry of Dark Clouds, *Astrophysical Journal Letters*, *700*, 752–761, doi: 10.1088/0004-637X/700/1/752.

Wang, X.-B., and L.-S. Wang (2009), Photoelectron Spectroscopy of Multiply Charged Anions, *Annual Review of Physical Chemistry*, *60*, 105–126, doi: 10.1146/annurev.physchem.59.032607.093724.

Wang, Z.-C., and V. M. Bierbaum (2016), Reactions of substituted benzene anions with N and O atoms: Chemistry in Titan's upper atmosphere and the interstellar medium, *The Journal of Chemical Physics*, *144*(21), 214304, doi: 10.1063/1.4952454.

Wang, Z.-C., C. A. Cole, N. J. Demarais, T. P. Snow, and V. M. Bierbaum (2015), Reactions of azine anions with nitrogen and oxygen atoms: Implications for titans upper atmosphere and interstellar chemistry, *Journal of the American Chemical Society*, *137*(33), 10,700–10,709, doi: 10.1021/jacs.5b06089, pMID: 26281019.

Wei, H. Y., C. T. Russell, M. K. Dougherty, F. M. Neubauer, and Y. J. Ma (2010), Upper limits on Titan's magnetic moment and implications for its interior, *Journal of Geophysical Research (Planets)*, *115*(E14), E10007, doi: 10.1029/2009JE003538.

Wekhof, A. (1981), Negative ions in comets, *Moon and Planets*, *24*, 157–173, doi: 10.1007/BF00910606.

Wellbrock, A. (2012), Cassini plasma spectrometer observations of titans ionospheric electrons and negative ions, Ph.D. thesis, University College London.

Wellbrock, A., A. J. Coates, G. H. Jones, G. R. Lewis, and J. H. Waite (2013), Cassini CAPS-ELS observations of negative ions in Titan's ionosphere: Trends of density with altitude, *Geophysical Research Letters*, *40*, 4481–4485, doi: 10.1002/grl.50751.

Westlake, J. H., et al. (2012), The observed composition of ions outflowing from Titan, *Geophysical Research Letters*, *39*, L19104, doi: 10.1029/2012GL053079.

Westlake, J. H., J. H. Waite, N. Carrasco, M. Richard, and T. Cravens (2014), The role of ion-molecule reactions in the growth of heavy ions in Titan's ionosphere, *Journal of Geophysical Research (Space Physics)*, *119*, 5951–5963, doi: 10.1002/2014JA020208.

Whipple, E. C. (1981), Potentials of surfaces in space, *Reports on Progress in Physics*, *44*, 1197–1250, doi: 10.1088/0034-4885/44/11/002.

Wicks, R. T., et al. (2016), A Proton-cyclotron Wave Storm Generated by Unstable Proton Distribution Functions in the Solar Wind, *Astrophysical Journal Letters*, *819*, 6, doi: 10.3847/0004-637X/819/1/6.

Wildt, R. (1939), Negative Ions of Hydrogen and the Opacity of Stellar Atmospheres., *Astrophysical Journal Letters*, *90*, 611, doi: 10.1086/144125.

Wilson, E. H., and S. K. Atreya (2003), Chemical sources of haze formation in Titan's atmosphere, *Planetary and Space Science*, *51*, 1017–1033, doi: 10.1016/j.pss.2003.06.003.

Wilson, R. J., R. L. Tokar, W. S. Kurth, and A. M. Persoon (2010), Properties of the thermal ion plasma near Rhea as measured by the Cassini plasma spectrometer, *Journal of Geophysical Research (Space Physics)*, *115*, A05201, doi: 10.1029/2009JA014679.

Wilson, R. J., F. Bagenal, and A. M. Persoon (2017), Survey of thermal plasma ions in Saturn's magnetosphere utilizing a forward model, *Journal of Geophysical Research (Space Physics)*, *122*, 7256–7278, doi: 10.1002/2017JA024117.

Winske, D., and O. Omidi (1992), *Hybrid Cods*, pp. 103–160.

Winske, D., L. Yin, N. Omidi, and et al. (2003), Hybrid Simulation Codes: Past, Present and Future - A Tutorial, in *Space Plasma Simulation*, *Lecture Notes in Physics, Berlin Springer Verlag*, vol. 615, edited by J. Büchner, C. Dum, and M. Scholer, pp. 136–165.

Wiza, L. J. (1979), Microchannel plate detectors, *Nuclear Instruments and Methods*, *162*, 587–601, doi: 10.1016/0029-554X(79)90734-1.

Wu, C. S., and R. C. Davidson (1972), Electromagnetic instabilities produced by neutral-particle ionization in interplanetary space, *Journal of Geophysical Research*, *77*, 5399, doi: 10.1029/JA077i028p05399.

Xaktly (2014), `http://xaktly.com/PeriodicTrends.html`, accessed April 2018.

Young, D. T., et al. (2004), Cassini Plasma Spectrometer Investigation, *Space Science Reviews*, *114*, 1–112, doi: 10.1007/s11214-004-1406-4.

Zhang, T. L., et al. (2012), Magnetic Reconnection in the Near Venusian Magnetotail, *Science*, *336*, 567, doi: 10.1126/science.1217013.

Zimmer, C., K. K. Khurana, and M. G. Kivelson (2000), Subsurface Oceans on Europa and Callisto: Constraints from Galileo Magnetometer Observations, *Icarus*, *147*, 329–347, doi: 10.1006/icar.2000.6456.